Characterization of the new BATCH Teflon chamber and on-line analysis of isomeric multifunctional photooxidation products

Finja Löher[1,2], Esther Borrás[3], Amalia Muñoz[3], Anke Christine Nölscher[1,2]

[1]Department of Atmospheric Chemistry, University of Bayreuth, 95447 Bayreuth, Germany
[2]Bayreuth Center of Ecology and Environmental Research (BayCEER), University of Bayreuth, 95447 Bayreuth, Germany
[3]Fundación Centro de Estudios Ambientales del Mediterráneo (CEAM), 46980 Paterna, Valencia, Spain

Correspondence to: Finja Löher (finja.loeher@uni-bayreuth.de) and Anke C. Nölscher (anke.noelscher@uni-bayreuth.de)

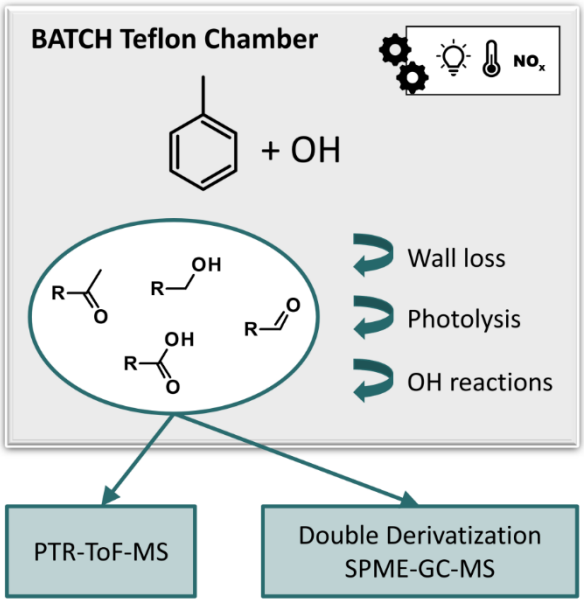

Abstract.

The photooxidation of volatile organic compounds (VOCs) in the troposphere has important implications for air quality, weather, and climate. A deeper understanding of the underlying mechanisms can be achieved by studying these reactions under controlled conditions and analyzing the emerging photooxidation products. This requires dedicated laboratory infrastructure as well as sensitive and selective analytical techniques. Here, we constructed a new 300 L indoor Teflon atmospheric simulation chamber as part of the Bayreuth ATmospheric simulation CHambers (BATCH) infrastructure. The chamber was irradiated by a bandpass-filtered solar simulator that enabled experiments with realistic photon fluxes and OH radical concentrations. It was coupled to a proton-transfer-reaction – time-of-flight – mass spectrometer (PTR-ToF-MS) and a solid phase microextraction – gas chromatography – mass spectrometry (SPME-GC-MS) system for the on-line analysis of the precursor VOC and its oxidation products in the gas phase. As part of the SPME-GC-MS method, multifunctional oxygenated compounds (carbonyls, alcohols, carboxylic acids) were derivatized with O-(2,3,4,5,6-Pentafluorobenzyl)-hydroxylamine (PFBHA) and N-trimethylsilyl-N-methyl trifluoroacetamide (MSTFA). We designed a permeation source for the on-line addition of internal standards to improve method reproducibility. The joint setup was tested and validated by studying the OH radical-induced photooxidation of toluene, one of the most abundant aromatic hydrocarbons in the atmosphere. For chamber characterization, we first derived the photolysis rates for several typical toluene products in the irradiated BATCH Teflon chamber (1.77×10^{-8} – 3.02×10^{-4} s^{-1}). Additionally, wall loss rates were determined empirically (4.54×10^{-6} – 8.53×10^{-5} s^{-1}), and then parameterized according to fundamental molecular properties. For the cresols ~~and benzyl alcohol~~, we compiled a weighted calibration factor for the PTR-ToF-MS, taking into account isomer-specific sensitivities as well as the relative distribution as determined by the SPME-GC-MS. The weighted calibration improved the instrumental agreement to 1~~4~~5 %, whereas the PTR-ToF-MS overestimated the sum of the isomers by ~~25~~ 31 % compared to the SPME-GC-MS concentrations when using the averaged calibration factor. Thus, the combined data set offered insight into both temporal trends and the isomeric composition. Finally, we conducted six toluene photooxidation experiments to evaluate the ring-retaining first generation products. Based on the loss-corrected concentrations, we derived formation yields for *o*-cresol (8.0±1.8 %), *m*-cresol (0.4±0.1 %), *p*-cresol (2.4±0.6 %), benzyl alcohol (0.5±0.1 %), and benzaldehyde (4.6±1.7 %) under NO_x-free conditions at T = 298±1 K. These yields are consistent with previous studies and therefore serve as proof-of-concept for our applied methods.

1 Introduction

Volatile organic compounds (VOCs) readily undergo photooxidation in the troposphere. These reactions are tightly linked to the formation of secondary pollutants such as ground-level ozone (O_3) or secondary organic aerosol (SOA) (Henze et al., 2008; Kanakidou et al., 2005; Zhao et al., 2022). Furthermore, they directly impact the ambient budget of hydroxyl (OH) radicals and thus the oxidative capacity of the atmosphere (Lelieveld et al., 2008; Williams et al., 2016). Indirectly, VOC photooxidation affects radiative forcing as it competes with the removal of greenhouse gases such as methane (CH_4) (von Schneidemesser et al., 2015). To improve and complement model predictions of air quality and climate, the underlying reaction mechanisms of VOC photooxidation therefore need to be better constrained.

Atmospheric simulation chambers (ASCs) are an established and powerful tool to mimic tropospheric oxidation processes and to derive both mechanistic understanding and kinetic data (Chu et al., 2022; Finlayson-Pitts and Jr, 1999; Kiendler-Scharr et al., 2023). Typical applications include photooxidant studies (e.g. Carter et al., 1979), gas-phase reaction and product studies (e.g. Zaytsev et al., 2019), and aerosol studies (e.g. Charan et al., 2020). In ASCs, added reagents and ambient conditions can be controlled with great precision. Thus, they enable gradual increases in complexity, the imitation of diverse environments and chemical regimes, and finally transferability to the real world. These data in turn provide the foundation of atmospheric chemistry models such as the near-explicit Master Chemical Mechanism (MCM) for gas-phase reactions (Jenkin et al., 2003; Saunders et al., 2003).

ASCs worldwide differ in their size and shape, material, and light source. For instance, the EUPHORE (EUropean PHOtoREactor) chamber is spherical, irradiated by natural sunlight, and one of the largest photoreactors in Europe with a volume of about 200 m³ (Muñoz et al., 2018; Zádor et al., 2006). In contrast, other chambers fit into laboratory facilities (e.g. Carter et al., 2005; Huang et al., 2017). Such indoor chambers have the advantage of being independent of weather and season but require carefully tuned artificial light sources. Knowledge of the spectral distribution and intensity of these lights sources is needed for assessing the analogy to the natural solar spectrum, radical production rates, and photolytic losses of the involved species. Regarding the wall material of ASCs and flow reactors, common choices include borosilicate glass (e.g. Behnke et al., 1988), quartz (e.g. Huang et al., 2017), stainless steel (e.g. Shaw et al., 2018), and Teflon films (e.g. Leskinen et al., 2015). Teflon films provide flexible arrangements of the chamber design and volume, are UV-transparent, and are a preferred option for many gas-phase studies due to their high chemical inertia (Schwantes et al., 2017; Zádor et al., 2006; Zaytsev et al., 2019). Nevertheless, wall losses matter in Teflon chambers as well, especially for species with low volatility, for small chambers, and for experiments conducted over long time frames (Grosjean, 1985; Krechmer et al., 2020; Ye et al., 2016; Zhang et al., 2015). Regardless of their specific design, all chambers therefore need to be characterized thoroughly (Alfarra et al., 2023; Carter et al., 2005; Leskinen et al., 2015; Ma et al., 2022) to account not only for contamination and artefacts but also for chamber- and compound-specific losses.

In recent years, the identification and quantification of the multifunctional products formed during VOC photooxidation has become increasingly important and has contributed to great advances in the understanding of autoxidation (e.g. Rissanen, 2021), gas-particle-partitioning (e.g. Gkatzelis et al., 2018), and peroxy radical chemistry (e.g. Berndt et al., 2018). Their analysis is often approached by spectroscopic methods (e.g. Klotz et al., 1998; Olariu et al., 2002) or stand-alone mass spectrometry (MS) (e.g. Baltaretu et al., 2009; Schwantes et al., 2017; Zaytsev et al., 2019). A powerful soft ionization technique for the real-time MS analysis of gas-phase species is by proton transfer reaction (PTR) (Lindinger et al., 1998). PTR-MS is selective to compounds with higher proton affinity than water and commonly applied to quantify airborne VOC and their photooxidation products (e.g. Müller et al., 2012; Zaytsev et al., 2019). When using high resolution mass spectrometers such as Time of Flight (ToF) models, PTR-ToF-MS spectra give insights into sum formulas and enable suspect screening (Romano and Hanna, 2018).

Meanwhile, isomeric information remains scarce for many reaction systems, even though isomers can differ in their properties, rate constants, and yields, and can help elucidating precise reaction mechanisms and intermediate species (Atkinson et al., 1980; Olariu et al., 2002). To distinguish between mass-equal isomers, MS detectors can be coupled to gas chromatography (GC) so that compounds are identified along two dimensions. However, oxygenated products such as ketones, aldehydes, alcohols, and carboxylic acids are often not suitable for GC analysis due to their high fragility and polarity. If analysable at all, there is a substantial risk of losses, poor separation, surface reactions, or conversions to other species during the chromatographic process, resulting in a lowered sensitivity and potentially creating artefacts (Rivera-Rios et al., 2014; Vasquez et al., 2018). To mitigate these problems, Borrás et al. (2021) have recently proposed an on-line GC-MS method with solid phase microextraction (SPME) sampling and on-fibre double derivatization of fragile analytes.

SPME is a sampling and enrichment technique which was first developed by Arthur and Pawliszyn (1990). The associated fibres are coated with a thin layer of a stationary sorbent phase which is exposed to extract and retain analytes during sampling. SPME can be used as a preparatory step to GC-MS analysis, in which case the high temperature in the GC inlet desorbs the analytes from the coated fibre. Advantages include high selectivity and sensitivity, minimization of human error due to the high degree of automation associated with autosampler systems, the reduction in solvent consumption, and the increased analytical throughput by fewer preparation steps and shorter extraction times (Arthur and Pawliszyn, 1990; Borrás et al., 2021; Koziel and Pawliszyn, 2001). However, the performance and reproducibility of SPME can be compromised by saturation effects and competition between analytes due to the limited fibre sorption capacity (Bartelt, 1997) as well as varying extraction efficiencies due to fibre effects (Tumbiolo et al., 2004).

By controlled chemical modification, derivatization procedures can help preserving molecular structures and stabilizing analytes throughout the chromatographic process. Additionally, the compounds of interest can be made more amenable to the

specific analytical technique, such as by increasing their volatility for subsequent GC separation. For the analysis of photooxidation products, this concerns in particular the derivatization of hydroxy groups (e.g. alcohols, carboxylic acids) and carbonyl groups (e.g. aldehydes, ketones). The most common approaches for subsequent GC-MS analysis include silylation for the hydroxy group using reagents like *N*-trimethylsilyl-*N*-methyl trifluoroacetamide (MSTFA) or *N*,*O*-bis(trimethylsilyl)trifluoroacetamide (BSTFA), and oxime formation for the carbonyl group using for instance *O*-(2,3,4,5,6-Pentafluorobenzyl)-hydroxylamine (PFBHA). These derivatization techniques have been used, for example, to analyze gaseous and particulate oxygenated products formed in the photooxidation of aromatic compounds (e.g. Gómez Alvarez et al., 2007; White et al., 2014), monoterpenes (e.g. Jang and Kamens, 1999; Yu et al., 1998), or VOC mixtures (e.g. Pindado Jiménez et al., 2013) in laboratory studies. By combining silylation and oxime formation, ~~can also be used in combination to cover~~ a broad range of compounds with diverse functionalities can be covered (Pindado Jiménez et al., 2013; White et al., 2014; Yu et al., 1998). As a means of automating the analytical process, derivatization can be performed directly on SPME fibres, which has been reported for PFBHA previously (Gómez Alvarez et al., 2007; Martos and Pawliszyn, 1998; Schmarr et al., 2008).

Here, we constructed and characterized a new indoor Teflon ASC as part of the **B**ayreuth **AT**mospheric simulation **CH**ambers (BATCH). For the purpose of studying multifunctional VOC photooxidation products, we coupled the BATCH Teflon chamber to a PTR-ToF-MS and an on-line SPME-GC-MS system with double derivatization using PFBHA and MSTFA. The developed methods were tested and validated by studying the reaction of toluene with OH radicals.

2 Study System: Reaction of Toluene with OH Radicals

Toluene is one of the most abundant aromatic hydrocarbons in the atmosphere (Cabrera-Perez et al., 2016). Most of its first generation products are well-studied (Atkinson et al., 1980; Bloss et al., 2005; Klotz et al., 1998; Zaytsev et al., 2019), making it a suitable and relevant reference system (e.g. Leskinen et al., 2015; Ma et al., 2022). Toluene reacts with OH radicals at a rate of about $k = 5.6\times10^{-12}$ molecules^{-1} cm^3 s^{-1} at T = 298 K (IUPAC, 2024), either via addition of the OH radical to the aromatic ring structure or via H abstraction from the substituted methyl group. ~~The addition pathway is dominant with a branching ratio in the range of 0.85 – 0.93 (Atkinson et al., 1980; Hu et al., 2007; Wu et al., 2014).~~ The MCMv3.1 (Bloss et al., 2005) distinguishes between four channels in the primary chemistry of toluene (Fig. 1). Following the formation of an intermediate OH-toluene-adduct (Klotz et al., 1998; Zhang et al., 2019), the addition pathway can lead to ring-retaining cresol isomers (*cresol channel*, 18 % yield) or to ring-opened products such as an epoxydicarbonylene compound (*epoxy-oxy channel*, 10 % yield). Alternatively, peroxy radical isomerization can produce bicyclic peroxy radicals, which ultimately fragment to form the α-dicarbonyl compounds glyoxal and methylglyoxal along with their respective furanone or γ-dicarbonyl co-products (*dicarbonyl channel*, 65 % yield). In the H abstraction pathway (*benzaldehyde channel*, 7 % yield), benzyl radicals readily form peroxy radicals, which undergo a range of bimolecular reactions, producing ring-retaining products such as benzaldehyde and benzyl alcohol (Bloss et al., 2005). The follow-up chemistry of major toluene products such as the cresols, benzaldehyde,

or the different dicarbonyls has been the subject of previous laboratory studies (e.g. Atkinson et al., 1980; Liu et al., 1999; Majer et al., 1969; Olariu et al., 2002; Schwantes et al., 2017).

Here, we aimed at evaluating the formation yields of the first generation products that can be calibrated and quantified and that are specific to their reaction channel. The dicarbonyl products glyoxal and methylglyoxal occur not only in the primary chemistry of toluene but are also formed as secondary products in most channels (Atkinson et al., 1980; Bloss et al., 2005; Wagner et al., 2003), especially in the breakdown of other dicarbonyls (Liu et al., 1999). Although ~~their~~ primary production is typically dominant (Gómez Alvarez et al., 2007; Volkamer et al., 2001), ~~a contribution from~~ secondary sources contribute to a fraction of~~to~~ the~~ir~~ observed concentrations of glyoxal and methylglyoxal ~~cannot be fully dismissed~~. Meanwhile, their co-products remain poorly constrained (Bloss et al., 2005; Jenkin et al., 2003; and references therein) and are not available as authentic standards. The epoxy-oxy channel is highly controversial (e.g. Hu et al., 2007; Wu et al., 2014; Zaytsev et al., 2019) and included in the MCM only based on qualitative indications in order to balance the reaction flux (Bloss et al., 2005; Jenkin et al., 2003). No authentic standard of the epoxydicarbonylene product is available. Therefore, we focus especially on the main NO_x-free ring-retaining first generation products of toluene, namely the cresol isomers, benzyl alcohol, and benzaldehyde. For the purpose of evaluating the novel setup, however, we refer to the entire test system with its wide range of multifunctional products in the first and second generation (beyond the scope of the photooxidation chemistry shown in Fig. 1).

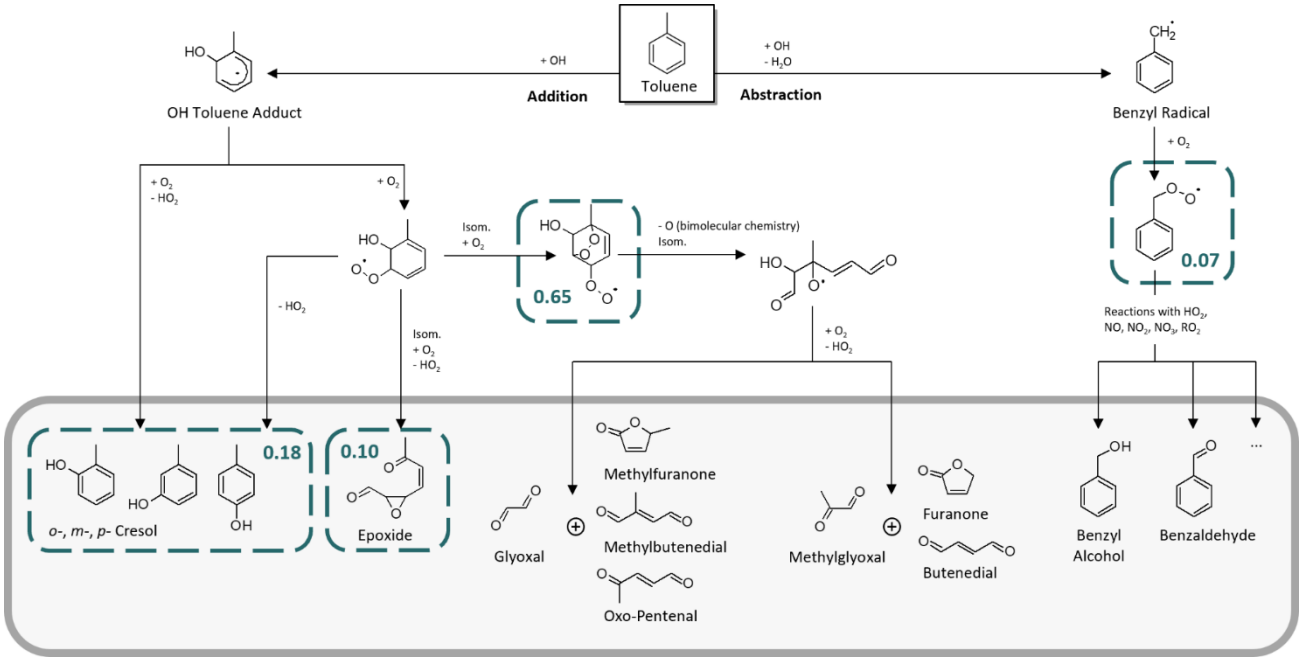

Figure 1: Primary chemistry of toluene following the reaction with OH radicals in the MCM. The blue boxes represent the four major channels and their corresponding yields. The grey area includes the main first generation products.

3 Experimental

An overview of the novel laboratory setup is provided in Fig. 2. The BATCH Teflon chamber was located in a temperature-controlled room (Hans Zettner GmbH, 3×4×5 m), in which the temperature could be adjusted between -25 °C and 35 °C with a stability of ±1 K (DeLonghi, HCS 2550 FTS and Dixell, XR170C).

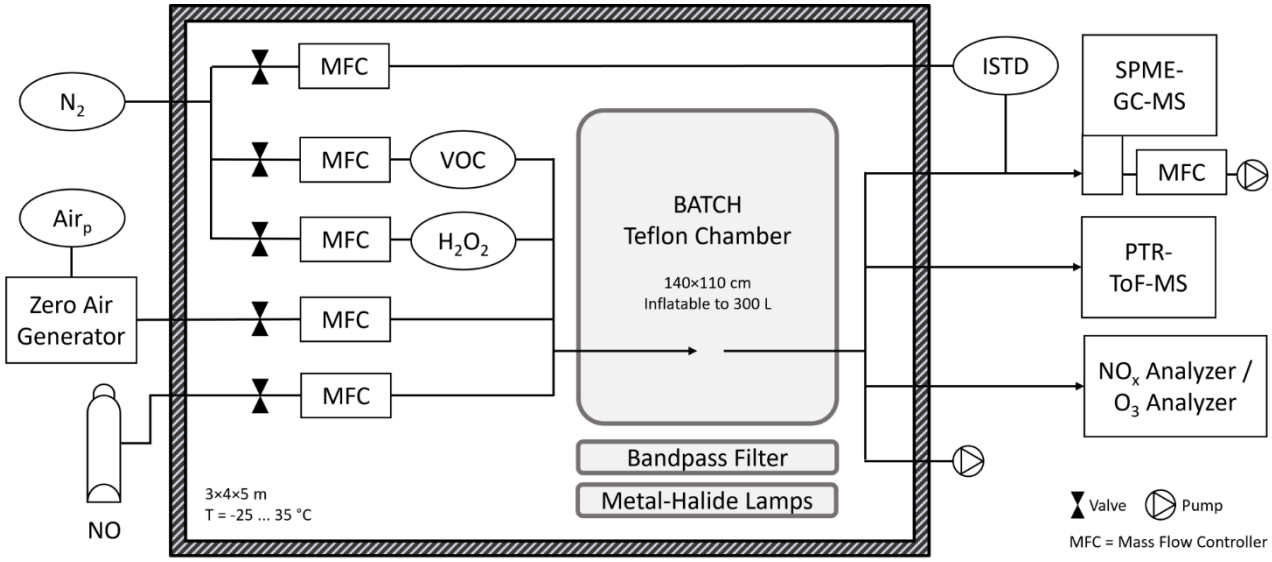

Figure 2: BATCH Teflon chamber with infrastructure and instrumentation. The Teflon chamber was installed in a temperature-controlled room (T = -25 °C – 35 °C) and placed above a bandpass-filtered solar simulator. Pressurized air and N_2 were available from the in-house gas supply. Added reagents included the VOC precursor, hydrogen peroxide (H_2O_2) as OH radical precursor, optionally nitric oxide (NO), and zero air as matrix. The VOC precursor and H_2O_2 were introduced with a flow of N_2. The chamber had one connector which was used as inlet during filling and as outlet during the experiments. All lines were made from polytetrafluoroethylene (PTFE). Coupled analytical instruments included a NO_x analyser, an O_3 analyser, a PTR-ToF-MS, and an on-line SPME-GC-MS with attached sampling cell. Two internal standards (ISTDs) were added into the SPME-GC-MS flow using a permeation source. Dimensions are not to scale.

3.1 Atmospheric Simulation Chamber

The BATCH Teflon chamber was made from UV-transparent fluorinated ethylene propylene (FEP). We constructed the pillow-shaped bag by folding a single sheet of a 50 µm thick FEP film (Chemours, 200A FEP100) and heat-sealing (Dieck, UM 802) the three open sides. Excluding the heat-sealed areas, the empty and flattened chamber was 140×110 cm in size. It ~~The chamber~~ was suspended in a metal scaffold, with the two short sides being used as top and bottom ends. It was not further stabilized into a specific shape, so that it remained flexible and fully collapsible, and could be operated in batch mode. ~~It~~ The chamber could be filled to approximately 300 L, in which case the surface-area-to-volume ratio was about SA:V = 0.1 cm^{-1}. When it was inflated, it expanded to a maximum of about 100 cm in the third dimension. To reduce the risk of leaks, only one connector was installed at the front side of the chamber and used both as inlet (during filling) and outlet (during ongoing

experiments). ~~The chamber was suspended in a metal scaffold, with the two short sides being used as top and bottom ends. It was not further stabilized into a specific shape, so that it remained flexible and fully collapsible, and could be operated in batch mode.~~

3.1.1 Light Source and Photolysis Rates

The chamber was irradiated by a solar simulator, described in detail previously (Bleicher, 2012; Buxmann et al., 2012; Siekmann, 2018; Wittmer et al., 2015). The solar simulator was located underneath the chamber and consisted of seven metal-halide gas discharge medium-arc lamps (Osram, HMI 1200 W, HMI = hydrargyrum medium-arc iodide) with a total power of 8.4 kW. A two-fold bandpass filter was positioned in between the lamps and the chamber to better reproduce the natural solar spectrum. As UV filter, a 3 mm thick borosilicate glass plate (Schott, Tempax) was mounted approximately 1 m above the lamps. A 3 cm column of decalcified water on top of the glass plate was used both as an IR filter and as a cooling system. During the experiments, the water was circulated to prevent overheating.

The emission spectrum of the solar simulator was already available from a previous measurement by Bleicher (2012). However, aging and replacement of the lamps, changes in the optical properties of the glass plate, or trace contaminations in the water layer can affect the photon flux. Therefore, we recorded an updated emission spectrum with a spectroradiometer (StellarNet, SILVER-Nova) in the wavelength range λ = 325 – 1000 nm. The instrument was equipped with a 14 µm slit for a spectral resolution of 0.75 nm, and a CR2 cosine receptor calibrated with NIST traceable calibration lamps. An aperture with 11 % transmission was used to extend the dynamic range. We performed 30 measurements in 15 different positions above the solar simulator to represent the spatial expansion of the inflated chamber. We selected 3 vertical planes (bottom, middle, top) and 5 spots (middle, front, back, left, right) on each plane. The final spectrum was derived as the average of these measurements. In order to characterize lower wavelengths ranges, we compared our recorded spectrum to the old measurement by Bleicher (2012). We scaled the old spectrum to the new spectrum according to the data available in the spectral range of λ = 350 – 500 nm. This scaled spectrum was used for the wavelength range λ = 262 – 325 nm.

We calculated the photolysis rates of the individual compounds according to Eq. (1):

$$J = \int_{\lambda_{min}}^{\lambda_{max}} \phi(\lambda)\sigma(\lambda)F(\lambda)\Delta\lambda \quad (1)$$

where J is the photolysis rate in s^{-1}, λ is the wavelength in nm, ϕ is the quantum yield in molecules photons^{-1}, σ is the absorption cross section in cm^2 molecules^{-1}, and F is the photon flux of the solar simulator in photons cm^{-2} nm^{-1} s^{-1}. Compound-specific absorption cross sections and quantum yields were taken from the literature (Table S1). Whenever available, IUPAC-recommended values were selected. If such recommendations were missing, absorption cross section data sets were selected to be recorded at a temperature close to T = 298 K, have a high spectral resolution, and cover a wide wavelength range. If no absorption cross section was available, we assumed that no substantial photolytic loss occurred and did not compile a photolysis

rate. For the quantum yields, we used wavelength-specific values or distinct values assigned to a defined actinic range. Otherwise, we assumed a quantum yield of 1 which can be regarded as the upper limit. More details and visualization are provided in the Supplement S1.1 and Fig. S1.

To validate the recorded spectrum as well as the scaled spectrum in the UV range, we performed two actinometric experiments. Firstly, we evaluated the NO_2 photolysis rate as described for example by Bohn et al. (2005). We injected 40 ppbv of NO_2 (Rießner-Gase, 106 ppmv in N_2) into the dark chamber in a zero air matrix. After 15 minutes for mixing, the solar simulator was ignited to start the photochemistry. The photolysis rate of NO_2 was calculated with NO_2, NO, and O_3 in photostationary state (for details, see Supplement S1.2 and Fig. S2). Secondly, we measured the photolysis rate of methylglyoxal by injecting 120 ppbv of the pure compound into the chamber and observing the wall-loss-corrected decay while the chamber was irradiated (see Supplement S1.2 and Fig. S3). Both NO_2 and methylglyoxal absorb in a broad UV-vis range (Table S1) and are hence useful to reference spectral data.

3.1.2 Wall Losses

To obtain the individual wall losses, a solution containing all authentic standards was injected into the chamber in a dry N_2 matrix at T = 298±1 K (c = 12.3×10^{10} molecules cm^{-3}, see SPME-GC-MS calibration in Sect. 3.2.1). We then recorded five consecutive SPME-GC-MS measurements in the dark. For each compound, the relative response was plotted against time and the first order loss rate in s^{-1} was derived by exponential regression. In order to characterize compounds without available authentic standards as well, we developed a parameterization of these empirical rates as a function of their vapor pressure, molecular weight, and oxygen-to-carbon ratio, as described in more detail in Sect. 4.1.2.

3.2 Analytical Instrumentation

While the SPME-GC-MS enabled the quantitative and isomer-resolved analysis of photooxidation products, the PTR-ToF-MS was used for analysing the sum of isomers on a high temporal resolution, for suspect screening, and for monitoring toluene as the precursor VOC. All solvents and authentic standards were purchased in the highest available purity (see Supplement S2.1). The instrumental setup was complemented by NO_x and O_3 analysers (see Supplement S2.2).

3.2.1 SPME-GC-MS for Isomer-Resolved VOC Product Analysis

The SPME-GC-MS setup included an SPME autosampler unit (PAL, RSI 85), a gas chromatograph (Agilent, 7890B), and a mass spectrometer (Agilent, 5977A, electron ionization source Xtr 350, Single Quad). The GC-MS was operated with splitless injections, a standard HP-5MS column ramping from a temperature of 45 °C to 280 °C, and in both scan and selected ion monitoring (SIM) mode. Details on the instrumental settings are listed in Table S2. The selected SPME fibre had a mixed polydimethylsiloxane (PDMS) and divinylbenzene (DVB) coating (Agilent, 5191-5873, PDMS/DVB, 65 µm thickness). Joint PDMS/DVB coatings are bipolar and combine absorption and adsorption extraction mechanisms. They are not only well-

suited for the analysis of oxygenated products but also have a high affinity towards nitro-aromatic compounds and towards amines such as PFBHA. We exchanged the SPME fibres every three to four experiments.

We adopted the on-fibre double-derivatization method of Borrás et al. (2021), including (1) the extraction of PFBHA as carbonyl reagent, (2) the on-line sampling of the gas-phase photooxidation products, (3) the extraction of MSTFA as hydroxy/carboxylic reagent, and (4) the thermal desorption of the derivatized compounds from the fibre into the GC-MS inlet. The derivatization reagents were prepared freshly for each experiment in 20 mL glass vials. 2 mL of PFBHA solution (c = 85 mg L^{-1} in H_2O) were made from a concentrated stock solution (c = 850 mg L^{-1} in H_2O) which was prepared weekly and stored in the dark at 4 °C. For the silylation reagents, 40 µL of MSTFA were mixed with 10 µL of trimethylchlorosilane (TMCS) as catalyst for higher silylation efficiency. At the beginning of each SPME-GC-MS sequence, the fibre was conditioned at elevated temperature (T = 240 °C) in an inert N_2 environment. If a new fibre was used, it was placed in the conditioning cell for 60 minutes. If an old fibre was re-used, it was first cleaned with methanol (3 minutes immersion, 10 minutes desorption) and then conditioned for 30 minutes. The steps of each subsequent sampling cycle are summarized in Table S3 and were automated via the SPME autosampler unit. Including fibre conditioning times, an entire run took 41 minutes.

A customized PTFE sampling cell (Fig. S4) was placed in the SPME-GC-MS sample tray, enabling the on-line extraction of the photooxidation products (for details, see Supplement S3.2). In the cell, the fibre was placed perpendicular to the sample air flow for better sampling efficiency (Gómez Alvarez et al., 2012). We used a flow rate to 5 SLPM to accommodate the limited chamber volume and to prevent excessive physical stress on the fibre, while still providing enough mass for analysis and enabling fast equilibration and transportation through the transfer line. The resulting air velocity was 131 cm s^{-1}, which is well above the critical value of 10 cm s^{-1} (Gómez Alvarez et al., 2012). The calculated Reynolds number of Re = 760 indicates laminar flow conditions. To maintain comparable conditions between the experiments and to reduce losses, the transfer line from the chamber to the sampling cell (~ 6 m length, 6 mm inner diameter) was temperature-controlled to 50 °C.

We used two internal standards (ISTDs) to correct for the general variability of SPME fibres (Tumbiolo et al., 2004) as well as for variations in the derivatization efficiency. These ISTDs were added into the transfer line between the chamber and the SPME-GC-MS sampling cell by means of a customized permeation source (for details, see Supplement S3.3 and Fig. S5). To validate the temporal stability of the permeation source, the enriched outflow was monitored over a period of one week by PTR-ToF-MS. Phenol-d_6 was used to correct alcohols and carboxylic acids (derivatized by MSTFA/TMCS), while acetophenone-d_8 was used to correct aldehydes and ketones (derivatized by PFBHA). Multifunctional compounds were assigned to the ISTD which resulted in the higher R^2 value of the calibration curve. Compounds lacking functional groups amenable to the derivatization scheme were not ISTD-corrected (Table 1).

We tested several known toluene oxidation products. The retention times and SIM masses of the compounds which were included in the final method are provided in Table 1. The SIM masses were selected based on the electron ionization (EI) mass spectra measured for the authentic standards. We considered only those SIM masses which result from mass shifts and fragmentations that are typical for the respective derivatization process (for details, see Supplement S3.4 with Fig. S6 and S7). Thus, we ensured an unambiguous assignment of the quantified ion to the derivatized compound structure. This was necessary so that the internal standards, which were also specifically monitored in their derivatized form, could provide a meaningful correction. Additionally, we made sure to select ions which were still specific to the original molecular structure, instead of reagent fragments such as *m/z* 181 for PFBHA. These non-specific reagent fragments can be dominant and therefore increase sensitivity, but are more prone to interferences by compounds with similar functional groups and the same or a similar retention time. For each compound, we selected the most abundant ion in the EI spectrum fulfilling these criteria. Additional information on the peak systems and the measured ions is given in Table S4.

To account for losses in the transfer line, the extraction from the sampling cell, and the on-line ISTD addition, we calibrated the analytes determined by SPME-GC-MS directly from within the chamber. Joint stock solutions of the analytes were prepared in acetonitrile (ACN) at six different concentrations (c = 0 mM, 0.05 mM, 0.1 mM, 0.2 mM, 0.3 mM, 0.5 mM). For each calibration level, 125 µL of the solution were injected into an installed round-bottomed flask and flushed into the chamber with a 5 SLPM N_2 flow. After 15 minutes, the flask was heated to 60 °C for 5 minutes to ensure complete vaporization. Once the chamber was completely filled, three samples were measured by the on-line SPME-GC-MS system consecutively. The active sampling scheme during the calibration was exactly the same as during the experiments (Sect. 3.3.1). For the entire calibration, the ambient temperature was controlled at T = 298±1 K. In between the different calibration levels, we cleaned the chamber, the introduction system, and the sampling system thoroughly. Each calibration level was preceded by a blank measurement of the chamber to account for remaining carry-over. With a total chamber volume of about 300 L, the calibration levels spanned between c = 0 – 12.3×10^{10} molecules cm^{-3}, corresponding to mixing ratios of approximately 0 − 5 ppbv at standard pressure. The acquired responses of the analytes were corrected for the ISTD response, the blank value, and the determined wall loss rate. For each compound, a linear regression of these corrected relative responses against the concentration in molecules cm^{-3} was performed and forced through the origin. We calculated the limits of detection (LODs) as three times the standard deviation of the blank calibration sample. For most tested compounds, the LOD was in the low pptv range (median = 10.75 pptv for T = 298 K and standard pressure, Table 3 in Sect. 4.2.1).

For the chamber experiments, we calculated a total error of the concentration (*quantification error*) from the propagation of the compound-specific instrumental error, the calibration error, and the experimental error. The instrumental error (5 % – 52 %, Table 3 in Sect. 4.2.1) was obtained as the mean of the relative standard deviations (RSDs) for each calibration level. It was primarily affected by the GC-MS response, the derivatization procedure, fibre effects, and peak integration. Furthermore, it reflects the degree to which the ISTD response and the analyte response co-varied. The calibration error (18 %) included the

preparation and stability of the calibration solutions and their vaporization and transportation into the chamber. The experimental error (10 %) resulted from variations in the flows and injections during chamber filling and was calculated from the variability of the monitored toluene start concentrations across all experiments.

Table 1: List of all compounds monitored by SPME-GC-MS. Compound-specific abbreviations (Abb), retention times (RT), and molecular weights (MW) are given. The functional groups amenable to oxime formation (PFBHA derivatization) or silylation (MSTFA/TMCS derivatization) are denoted as aldehydes (CHO), ketones (C=O), alcohols (OH), and carboxylic acids (COOH). The selected ion monitoring (SIM) masses refer to the derivatized compounds. Internal standards (ISTDs) were assigned based on the derivatization mechanism (acetophenone-d_8 for oxime formation, phenol-d_6 for silylation). Compounds are sorted according to their retention time. Dashed horizontal lines mark the time segments starting at 4.0, 9.8, and 15.0 minutes, respectively.

Compound	Abb	RT / min	MW / g mol^{-1}	Oxime formation	Silylation	SIM / m/z	ISTD
Phenol-d_6[(a)]	PHE-d_6	5.78	100.15	-	1 × OH	156.1	-
o-Cresol	OCR	7.01	108.14	-	1 × OH	165.1	PHE-d_6
m-Cresol	MCR	7.15	108.14	-	1 × OH	165.1	PHE-d_6
p-Cresol	PCR	7.28	108.14	-	1 × OH	165.1	PHE-d_6
Benzyl alcohol	BOH	7.33	108.14	-	1 × OH	135.1	PHE-d_6
o-Nitrotoluene[(b)]	ONT	7.50	137.14	-	-	91.1	-
(Nitromethyl)benzene[(b)]	NMB	7.96	137.14	-	-	91.1	-
m-Nitrotoluene[(b)]	MNT	8.05	137.14	-	-	137.1	-
Benzoic acid	BAC	8.20	122.12	-	1 × COOH	179.1	PHE-d_6
p-Methylcatechol	PMC	10.42	124.13	-	2 × OH	268.1	PHE-d_6
Glycolaldehyde	GAL	10.80	60.05	1 × CHO	1 × OH	312.1	PHE-d_6
Nitrocresols[(c)]	NCR	11.61	153.14	-	1 × OH	210.1	PHE-d_6
Pyruvic acid	PAC	11.75	88.06	1 × C=O	1 × COOH	340.1	PHE-d_6
Acetophenone-d_8[(a)]	APH-d_8	12.95	128.20	1 × C=O	-	323.1	-
Benzaldehyde	BAL	13.18	106.12	1 × CHO	-	301.1	APH-d_8
Glyoxal	GLY	15.43	58.04	2 × CHO	-	448.1	APH-d_8
Methylglyoxal	MGL	15.82	72.06	1 × CHO, 1 × C=O	-	265.1	APH-d_8
p-Hydroxybenzaldehyde	PHB	16.46	122.12	1 × CHO	1 × OH	389.1	PHE-d_6

[(a)] *Internal Standard.*
[(b)] *Only NO_2 functional group.*
[(c)] *Co-elution of 2-nitro-p-cresol and 6-nitro-m-cresol.*

3.2.2 PTR-ToF-MS for VOC and Product Screening with High Temporal Resolution

The PTR-ToF-MS used in this work (Ionicon, PTR-TOF 4000) has a mass resolution of >4000 m/Δm (full width at half maximum) for *m/z* > 147. It is equipped with a multichannel plate (MCP) detector and an internal permeation source of 1,3-diiodobenzene ($C_6H_4I_2$) to calibrate the mass axis continuously. We operated the instrument with a drift tube pressure of 2.6 mbar, and a reduced electric field strength of E/N = 95 Td. For all PTR-ToF-MS data shown here, hydronium reagent ions

(H_3O^+) were used as the primary ion (PI) in order to enable ionization with low fragmentation and to accommodate the analysis of diverse classes of products (Lindinger et al., 1998; Romano and Hanna, 2018). During the experiments, the chamber air was sampled continuously through a 1/8" PTFE line of about 5 m length with a flow of 50 sccm. Besides the analysis of toluene, we focused here on the quantitative analysis of the major photooxidation products. All compounds were measured at their protonated mass (Table S5). For toluene, we monitored the ^{13}C-isotope at *m/z* 94.0716 to avoid artefacts related to peak saturation. We averaged all data in the experiments and the calibrations by the minute.

All PTR-ToF-MS calibrations were performed from the chamber to better mimic the conditions and losses during the experimental measurements. For the photooxidation products, the general procedure was analogous to the SPME-GC-MS calibration, except for that the calibration solutions were prepared in water instead of ACN. The aqueous matrix was necessary to avoid solvent mixing ratios in the chamber in the ppmv range, but limited the range of studied compounds to water-solvable ones. We calibrated the cresols, benzyl alcohol, benzaldehyde, glyoxal, and methylglyoxal. The change in relative humidity during the calibrations compared to the experiments was negligible, as only 125 µL water were injected into the 300 L chamber. For each calibration level, the PI-normalized signal was averaged over a stable time frame of 15 minutes after equilibration. The calibration curves were derived from the blank-corrected values and forced through the origin. The LODs were calculated as three times the standard deviation of the response obtained during an instrumental blank measurement that was performed with an activated charcoal filter. Except for glyoxal (LOD = 1827.8 pptv), the LODs varied between 0.5 pptv and 4.8 pptv (Table S6). Same as for the SPME-GC-MS, we derived the instrumental error as the mean RSD of all calibration levels, and calculated the quantification error from the propagation of the instrumental error (1 % – 2 % except for glyoxal with 89 %, Table S6), the calibration error (18 %), and the experimental error (10 %).

For the toluene calibration, we evaluated the measured signal~~s~~ in the filled chamber after equilibration and prior to the ignition of the solar simulator. As we always used the same start concentration of toluene, we averaged the measured response across all experiments (Sect. 3.3). These experiments were carried out over a period of 6 weeks.~~,~~ D~~d~~uring ~~which~~this time, we did not observe a substantial drift in the sensitivity of the instrument. ~~is not susceptible to substantial drift.~~ ~~W~~We ~~calibrated~~ performed a two-point calibration of toluene using the mean signal for its calculated start concentration of c = 3.79×10^{12} molecules cm^{-3} and the blank value of the cleaned chamber. The overall quantification error was 10 %, calculated as propagation of the instrumental error (0.30 %) and the experimental error (10 %, variability of monitored start concentrations).

To highlight the benefit of the combined analytical instrumentation, we aimed to resolve the C_7H_8O isomers also in the PTR-ToF-MS signal. In a first step, we compiled a weighted calibration similar to e.g. the work by Koss et al. (2018). Therefore, we performed separate calibrations for each of the three cresol isomers and benzyl alcohol. These calibrations were conducted on-line from the BATCH Teflon chamber analogously to the joint PTR-ToF-MS calibration. All compounds were analysed at the protonated mass of *m/z* 109.0626, yet the instrumental response of each of the isomers was derived individually. For

analyzing the sum signal during the photooxidation experiments, we calculated the weighted sensitivity for each of the isomers as the product of its instrumental sensitivity and its relative abundance. Since benzyl alcohol did not have any signal at this mass (Table S6), only the cresols isomers were included in the weighted calibration. Their relative abundances were derived as fixed values from the formation yields as determined with the SPME-GC-MS data (Sect. 4.3.2). ~~T~~According to Eq. (2), the sum of these weighted sensitivities was used as the weighted calibration factor for the *m/z* 109.0626 signal (Table S6). From the correctly quantified sum signal, we later extracted the experimental concentrations of the individual ~~C_7H_8O~~ cresol isomers using the same fixed relative abundances.

$$weighted\ calibration\ factor = \sum_i weighted\ sensitivity_i = \sum_i sensitivity_i \times relative\ abundance_i \quad (2)$$

3.3 Photooxidation Experiments and Data Analysis

In total, we performed 18 experiments at different temperatures and with different initial NO_x mixing ratios for method development purposes. To evaluate the product formation yields and gain mechanistic insight into the toluene chemistry, we focused here exclusively on six NO_x-free toluene-OH photooxidation experiments at T = 298±1 K and different degrees of photochemical aging (Table 2). These experiments were performed first to avoid the risk for contamination and wall sources of NO_x (e.g. Rohrer et al., 2005). We decided to work with an excess of toluene to keep secondary chemistry to a minimum and produce sufficient product mass for analysis.

Table 2: List of conducted NO_x-free experiments at T = 298±1 K. The monitored start concentration of toluene spread around the calculated start concentration of c = 3.79×10^{12} molecules cm^{-3}. The timing of the first (and all consecutive) SPME-GC-MS samples was varied to better constrain formation yields. For all experiments, we obtained 4 SPME-GC-MS samples, resulting in total experimental durations of about three hours.

Label	Toluene / molecules cm^{-3}	Lights / min	Sample 1 / min
Tol-OH-1	3.40×10^{12}	90	20
Tol-OH-2	3.23×10^{12}	75	10
Tol-OH-3	4.18×10^{12}	30	20
Tol-OH-4	3.93×10^{12}	45	30
Tol-OH-5	4.12×10^{12}	60	40
Tol-OH-6	3.79×10^{12}	105	10
Control	-	60	40

3.3.1 Experimental Protocol

Prior to each experiment, we cleaned the chamber and recorded blank values. To dilute and remove remaining impurities, the chamber was filled with zero air and then fully evacuated three times in total. Zero air was prepared by purifying pressurized synthetic air with a commercial zero air generator (Messer Griesheim GmbH, SL 50). In the first flushing cycle, the solar simulator was ignited to promote the oxidation of potential residuals and their release from the walls. After the cleaning, we

filled the chamber with zero air again, and measured preliminary chamber blanks ~~were measured by~~ with the SPME-GC-MS and the PTR-ToF-MS to confirm the cleanliness of the chamber and to test the instrumental performances. For the SPME-GC-MS, this concerned in particular the condition of the SPME fibre as indicated by the PFBHA and ISTD responses. For the PTR-ToF-MS, the background concentration of toluene was obtained. After these checks, the chamber was completely evacuated in preparation for the experiment. The temperature was set to the target value.

Upon completion of the preparatory work, we added the reagents sequentially. First, we introduced the VOC precursor into the chamber. The pure compound was injected through a septum into a 100 mL round-bottomed flask, which was then flushed with N_2 as pick-up flow (5 SLPM) for 15 minutes. In this work, we used 0.2 µL toluene (Roth, ≥ 99.9 % purity), equivalent to a target concentration of 3.79×10^{12} molecules cm^{-3} (154 ppbv at T = 298 K and standard pressure). Second, hydrogen peroxide (H_2O_2) was added as OH radical precursor by filling 3 mL of a 50 % aqueous solution (Sigma Aldrich) into a 5 mL impinger to enrich a flow of N_2 (100 sccm) which was entering the chamber for 20 minutes. We selected H_2O_2 because it provides a NO_x-free method of generating OH radicals and photolyzes even under the near-UV conditions in the chamber. If needed, NO was then introduced directly from a gas cylinder (Rießner-Gase GmbH, 2.88 ppmv in N_2). Finally, the chamber was filled to 300 L with zero air (10 SLPM). All flows were regulated by mass flow controllers and determined with flow meters.

After complete filling, the SPME-GC-MS, the PTR-ToF-MS, and if needed the NO_x and O_3 analysers, were connected to the chamber. The true experimental blank of the oxidation products was obtained in the presence of toluene and H_2O_2, and the start concentration of toluene was monitored. Afterwards, the solar simulator was turned on to initiate the photooxidation chemistry. The lights were kept covered for 3 minutes after ignition, as the emission of the lamps during this warm-up period is generally small and not reproducible (Bleicher, 2012; Wittmer et al., 2015). The start of the oxidation process was marked by the uncovering of the lights. For each SPME-GC-MS sample, the vacuum pump for active sampling was started 3 minutes prior to the on-line extraction and stopped again afterwards in order to conserve chamber volume but still allow sufficient time for equilibration. Since all instruments were attached to the same outlet line of the chamber, the PTR-ToF-MS sample flow (50 sccm) was affected by the active sampling of the SPME-GC-MS pump (5 SLPM) every 41 minutes. This effect was minimized by attaching the PTR-ToF-MS transfer line as closely as possible to the chamber (~5 cm distance from the chamber interior). Remaining artefacts in the PTR-ToF-MS signal were corrected by linear interpolation using the data acquired 2 min before and after the SPME-GC-MS pump was turned on, respectively.

During the experiments, ~~T~~the chamber was never emptied ~~depleted~~ to less than 30 % of its initial volume to avoid (i) too high surface-area-to-volume ratios and an increased importance of wall effects as well as (ii) contamination through leaks. After all the data were collected, the chamber was completely evacuated and then cleaned three times (zero air filling and subsequent evacuation). In the final cycle, the chamber was evacuated by the SPME-GC-MS pump to also clean the transfer line and sampling cell.

For each experiment, air pressure data were retrieved from the weather station at the Botanical Garden of the University of Bayreuth (4 km distance from the atmospheric chemistry laboratory) and averaged over the experimental time frame. We measured the relative humidity in the chamber in one of the experiments and derived a value of 0.1 %. This is consistent with the composition of the air mixture, since the only source of water in the chamber was the N_2 flow enriched with the H_2O_2/H_2O solution, accounting for only 2 L of the 300 L total chamber volume in all performed experiments.

3.3.2 Initial Data Treatment

The raw GC-MS data were processed using MassHunter (GC/MS Data Acquisition v10.1.49, Qualitative Analysis v10.0, Quantitative Analysis v10.2) for peak integration. All further data analysis was performed in Python (v3.9.7). After normalizing the responses to the assigned ISTDs (relative responses), they were blank-subtracted and converted to concentrations in molecules cm^{-3}. For the PTR-ToF-MS data, we used the IONICON Data Analyzer (v2.1.1.2) for mass axis calibration, peak definition, and PI-normalization. In Python, we compiled mean values per minute, subtracted blank values, and applied the calibration factors.

3.3.3 Loss Corrections

Corrections for compound-specific physical and chemical losses were needed to obtain the true formation yields of the studied photooxidation products. In the present work, these losses included wall losses, photolysis, and secondary OH radical reactions. As we evaluated the yields for NO_x-free conditions, secondary reactions with O_3 and NO_3 radicals as competing oxidants were irrelevant. We corrected the losses for each discrete data point iteratively in order to account for the simultaneous formation and loss of the photooxidation products. The calculation is shown in Eq. (32):

$$\Delta L(\Delta t) = \bar{c}(\Delta t) \times \Delta t \times k \quad (32a)$$

$$c_t^{corr} = c_{t-1}^{corr} + \Delta c(\Delta t) + \Delta L(\Delta t) \quad (32b)$$

where $\Delta L(\Delta t)$ is the absolute loss in units of molecules cm^{-3} that occurred over the time span between two given data points. This loss is defined by $\bar{c}(\Delta t)$ as the mean value of the measured concentrations c_t and c_{t-1} in molecules cm^{-3}, Δt as the time span between the two data points in s, and k as the first order loss rate constant for the specific loss process in s^{-1}. The total product concentration formed up to a given point in time, *loss-corrected concentration* hereinafter, entails both the measured concentration and the cumulative loss that occurred since the beginning of the experiment (Fig. S8). The loss-corrected concentration of a given data point c_t^{corr} is therefore calculated as the sum of the loss-corrected concentration of the previous data point c_{t-1}^{corr}, the absolute loss that occurred since that point in time $\Delta L(\Delta t)$, and $\Delta c(\Delta t)$ as the measured difference between these two data points (all in molecules cm^{-3}).

This procedure is based on the approach described by Galloway et al. (2011), but was adapted for the low temporal resolution of the SPME-GC-MS method by relating the loss term to $\bar{c}(\Delta t)$ rather than to the measured concentration of the previous data

point. The calculation was performed for each of the three loss processes individually, so as to better account for the conditions in the chamber, e.g. light or dark, and in order to derive the absolute losses associated with each process. All three corrections were implemented with reference to the measured data and then summed up to derive the final loss-corrected concentration (Fig. S8). The calculations were performed for the SPME-GC-MS and the PTR-ToF-MS analogously. In cases where different compounds with an unknown distribution contributed to a sum signal at the PTR-ToF-MS, we selected the rate constants of the compound which we assumed to be most abundant.

Both the wall loss rates and the photolysis rates were available as first order rate constants. While wall losses were corrected for the entire experimental duration, photolytic losses were corrected only for the periods in which the solar simulator was ignited. To treat the reaction with OH radicals using the same correction formula, we converted the second order reaction of any of the analytes with OH radicals to a pseudo first order approach. For this purpose, we referred to the OH exposure as the time-integrated OH radical concentration, as shown in Eq. (43):

$$OHexp_t = \int_{t=0}^{t=t} [OH]\Delta t \quad (4a)$$

$$\Delta OHexp = \int_{t=t-1}^{t=t} [OH]\Delta t \quad (4b)$$

$$\Delta t \times k' = \Delta t \times k \times [OH] = \Delta OHexp \times k \quad (43c)$$

where $OHexp_t$ is the OH exposure between time t and the beginning of the experiment in units of molecules cm^{-3} s, $[OH]$ is the OH radical concentration in molecules cm^{-3}, $\Delta OHexp$ is the difference of the OH exposure between the two data points in molecules cm^{-3} s, k' is the pseudo first order rate constant in s^{-1}, and k is the second order rate constant in molecules^{-1} cm^3 s^{-1}, ~~$[OH]$ is the OH radical concentration in molecules cm^{-3}, and $\Delta OHexp$ is the difference of the OH exposure between the two data points which is given in the units of molecules cm^{-3} s~~. The second order rate constants for the reactions of the photooxidation products with OH radicals were obtained from the IUPAC recommendations and the scientific literature (Table S7). ~~The~~ To circumvent the need for direct OH radical measurements, the OH exposure ~~calculation of the OH exposure~~ at a given point in time was calculated based on the observed decay of toluene ~~to circumvent the need for direct OH radical measurements~~, as shown in Eq. (54):

$$\Delta OHexp = OHexp_t - OHexp_{t-1} \quad (54a)$$

$$OHexp_t = \ln\left(\frac{[toluene]_t}{[toluene]_0}\right) / -k_{toluene+OH} \quad (54b)$$

where $OHexp_t$ and $OHexp_{t-1}$ are the OH exposures determined for the time steps associated with the target data point and the previous data point in molecules cm^{-3} s, $[toluene]_t$ and $[toluene]_0$ are the concentrations of toluene at the given point in time and at the beginning of the experiment in molecules cm^{-3}, and $k_{toluene+OH}$ = 5.6×10^{-12} molecules^{-1} cm^3 s^{-1} is the well-characterized second order rate constant of toluene with OH radicals (IUPAC, 2024). Based on the temporally resolved OH exposure (available in minute resolution according to the toluene data set), we used the relationship in Eq. (4b) to calculate OH radical concentrations averaged over the time intervals between t and t-1 according to Eq. (6):

$$[OH] = \Delta OHexp/\Delta t \quad (6)$$

3.3.4 Yield Calculations

The formation yields of the first generation products that we observed, identified, and quantified in the new chamber for T = 298±1 K in the absence of NO_x were calculated from a large data set assembled from six experiments (Table 2). For each compound, we plotted the loss-corrected concentration against the change of toluene for a given point in time, performed a linear regression of the collected data set, and determined the yield as the slope of this regression. This approach helps to minimize the impact of the random error by regressing over a broad range of precursor losses (e.g. Atkinson et al., 1989; Olariu et al., 2002). We included only those data for which the non-corrected value was higher than the LOD, to enhance accuracy and reliability. Since the data acquired at the end of the experiments were affected to a higher extent by secondary chemistry and chamber effects, we considered only the data obtained while the chamber was irradiated as well as the first sample in the dark in case of the SPME-GC-MS.

4 Results and Discussion

An exemplary time series of toluene and its ring-retaining first generation products for one of the experiments at T = 298±1 K under NO_x-free conditions is shown in Fig. 3. While the chamber was irradiated, OH radicals were generated and caused a decrease in toluene and the formation of products. No loss of toluene was observed after the lights were turned off, indicating the termination of the oxidation chemistry in the absence of photolytic OH radical generation.

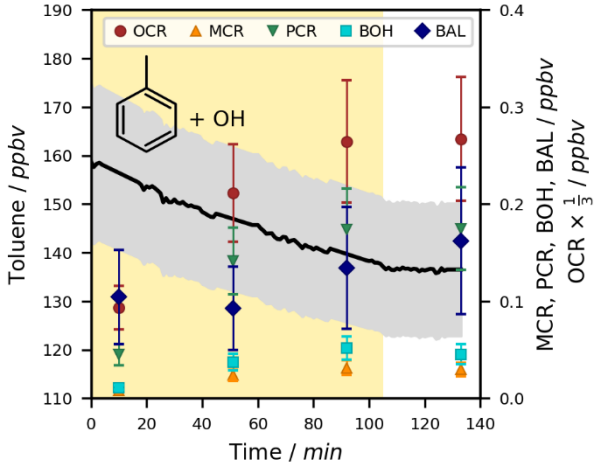

Figure 3: Exemplary time series for the OH radical-induced photooxidation of toluene at T = 298±1 K in the absence of NO_x. The temporal profiles of toluene and its ring-retaining first generation products in experiment Tol-OH-6 are shown. Toluene was determined by PTR-ToF-MS (black line, quantification error shown as grey area), while the products were analysed using the on-line double-derivatization SPME-GC-MS method (quantification error shown as error bars). No loss corrections were applied to the depicted data. The area shaded in yellow represents the period in which the chamber was irradiated. Toluene products in this figure include *o*-cresol (OCR), *m*-cresol (MCR), *p*-cresol (PCR), benzyl alcohol (BOH), and benzaldehyde (BAL).

Under the studied conditions, the OH radical reaction was the only relevant sink of toluene, so that the change in its concentration could be directly used for the calculation of OH radical concentrations and product formation yields. The photolysis rate of toluene in the irradiated chamber was calculated to be as low as $J = 3.78 \pm 1.44 \times 10^{-7}$ s^{-1} (Table S1). Due to the high vapor pressure (21.78 torr at T = 293 K (Munday et al., 1980)) and the low degree of functionalization of toluene, losses to the chamber wall were not substantial. ~~Its rate constants for reactions with O_3 and NO_3 radicals are about $k < 10^{-21}$ molecules^{-1} cm^3 s^{-1} and $k = 7.8 \times 10^{-17}$ molecules^{-1} cm^3 s^{-1} (IUPAC, 2024), so that these loss processes were irrelevant under all experimental conditions.~~

4.1 Chamber Characterization

The new BATCH Teflon chamber was built for the purpose of studying multifunctional gas-phase products. Losses and uncertainties in the quantification of these target species result amongst others from the interaction with the chamber setup. Thus, we first characterized the spectrum of the solar simulator. Secondly, we derived typical wall losses of the photooxidation products and proposed a chamber-specific parameterization. Thirdly, we assessed possible carry-over and artefacts.

4.1.1 Solar Simulator Spectrum and Photolysis Rates

The measured emission spectrum of the solar simulator is shown in Fig. 4a. On average, the emission intensity in our recorded spectrum was about 3 times higher compared to the previous measurement by Bleicher (2012), which was obtained by differential optical absorption spectroscopy (DOAS) and normalized to the empirical Cl_2 photolysis rate. This difference could relate to the specific emission and age of each lamp, or to the vertical distance at which the previous spectrum was recorded. Meanwhile, the same qualitative features are visible in both spectra. Using the newly measured spectrum (λ = 325 – 1000 nm) and the spectrum scaled from the old data set (λ = 262 – 325 nm), the NO_2 photolysis rates calculated theoretically ($2.07 \pm 0.79 \times 10^{-2}$ s^{-1}) and derived experimentally ($2.32 \pm 1.99 \times 10^{-2}$ s^{-1}, Fig. S2) agree within 12 %. For methylglyoxal, the experimental photolysis rate ($3.66 \pm 0.56 \times 10^{-4}$ s^{-1}, Fig. S3) is ~~1.~~21 % ~~fold~~ higher than the calculated value ($3.02 \pm 1.15 \times 10^{-4}$ s^{-1}), yet the uncertainties of these rates overlap. Hence, the updated spectrum with the scaled data in the UV range allows us to reliably derive photolysis rates in the BATCH Teflon chamber.

The calculated photolysis rates of the studied oxidation products (Table S1) were in the range between $1.77 \pm 0.67 \times 10^{-8}$ s^{-1} (*m*-nitrotoluene) and $3.02 \pm 1.15 \times 10^{-4}$ s^{-1} (methylglyoxal). High photolysis rates of $>10^{-4}$ s^{-1} were determined for the carbonyl compounds benzaldehyde, glyoxal, methylglyoxal, and pyruvic acid. Specific quantum yields were mostly available for those compounds which are prone to absorb in the solar actinic spectrum and have therefore been extensively investigated with regard to their photochemistry, such as carbonyls and nitro compounds. For the studied alcohols and carboxylic acids for which no quantum yield was available in the literature, we determined maximum photolysis rates of $<2 \times 10^{-5}$ s^{-1} with assumed

quantum yields of 1. These loss rates do not substantially affect the chemistry and calculated concentrations over the course of the experiment, so that over-corrections of the photolytic losses are negligible.

The emission of the solar simulator directly affected the photolysis of H_2O_2 and thereby the OH radical source. The photolysis of H_2O_2 generates OH radicals with a near-unity quantum yield (Vaghjiani and Ravishankara, 1990) and occurred with a rate of about $J = 1.13 \pm 0.43 \times 10^{-5}$ s^{-1} in the irradiated chamber (Fig. S1, Table S1). For NO_x-free experiments at T = 298±1 K, the resulting mean OH radical concentration was $[OH] = 4.89 \times 10^6$ molecules cm^{-3} while the solar simulator was activated. This is comparable to tropospheric daytime OH radical levels, which typically peak in the range of $2 \times 10^6 - 8 \times 10^6$ molecules cm^{-3} for similar latitudes (Altshuller, 1989). We did not observe any product formation in a test run without H_2O_2 addition, confirming H_2O_2 photolysis as the main source of OH radicals~~, rather than for example the release of HONO from chamber walls which would produce both OH radicals and NO~~.

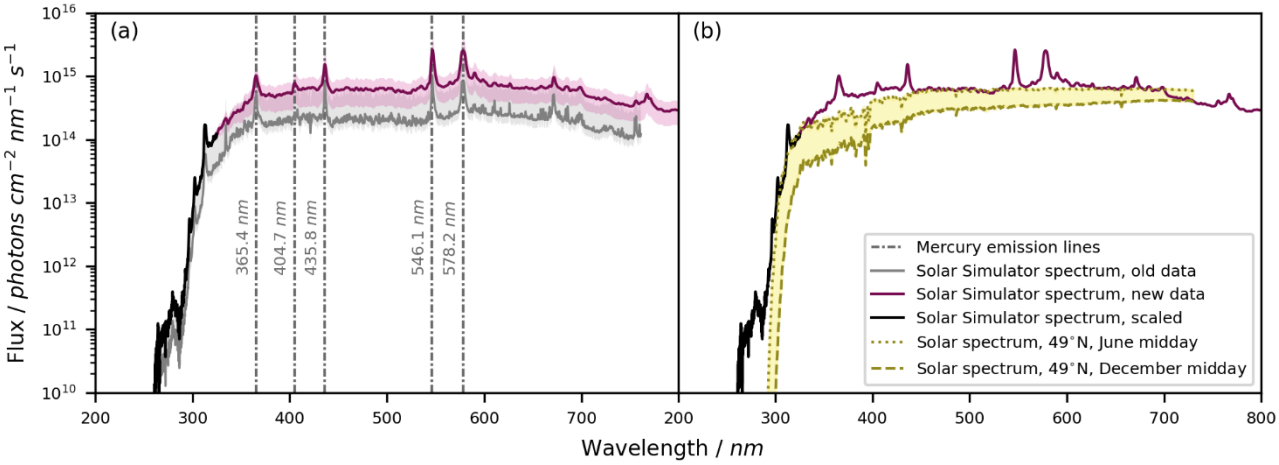

Figure 4: Solar simulator emission spectrum. (a) ~~The left figure shows the~~The emission spectrum of the solar simulator (7 HMI lamps with bandpass filter) available from an old measurement (Bleicher, 2012), the newly recorded spectrum, and the scaled spectrum in the wavelength range between λ = 262 – 325 nm (scaled by comparing the new data and the old data for the wavelength range λ = 350 – 500 nm). The new spectrum is shown as the mean ± standard deviation from 30 measurements at different positions above the solar simulator. The uncertainty in the old data results from the quantification of Cl radicals used to calibrate the actinic flux. The main Hg emission lines are shown. ~~In the right figure,~~(b) ~~t~~The solar simulator spectrum ~~is~~ compared against the natural actinic flux as calculated with the TUV radiation model for 49°N for midday in June and December respectively (NCAR, 2024). Figure concept inspired by Bleicher (2012).

By design, the HMI lamp housings filter radiation λ < 260 nm (Siekmann, 2018) in order to block for instance the 185 nm and 254 nm mercury emission lines. By shifting the UV absorption edge to about λ < 300 nm, the bandpass filter of the solar simulator reproduced a more realistic photon flux in the UV range. For comparison, Fig. 4b shows the resemblance between the solar simulator emission spectrum and the natural solar spectrum, as calculated for a latitude of 49°N with the National Center for Atmospheric Research (NCAR) Tropospheric Ultraviolet and Visible (TUV) radiation model v5.3 (NCAR, 2024) for midday in June and December.

~~The emission of the solar simulator directly affected the photolysis of H_2O_2 and thereby the OH radical source. The photolysis of H_2O_2 generates OH radicals with a near-unity quantum yield (Vaghjiani and Ravishankara, 1990) and occurred with a rate of about $J = 1.13±0.43×10^{-5}$ s^{-1} in the irradiated chamber (Fig. S1, Table S1). For NO_x-free experiments at T = 298±1 K, the resulting mean OH radical concentration was $[OH] = 4.89×10^6$ molecules cm^{-3} while the solar simulator was activated. This is comparable to tropospheric daytime OH radical levels, which typically peak in the range of $2×10^6 – 8×10^6$ molecules cm^{-3} for similar latitudes (Altshuller, 1989). We did not observe any product formation in a test run without H_2O_2 addition, confirming H_2O_2 photolysis as the main source of OH radicals, rather than for example the release of HONO from chamber walls which would produce both OH radicals and NO.~~

~~The calculated photolysis rates of the studied oxidation products (Table S1) were in the range between $1.77±0.67×10^{-8}$ s^{-1} (*m*-nitrotoluene) and $3.02±1.15×10^{-4}$ s^{-1} (methylglyoxal). High photolysis rates of $>10^{-4}$ s^{-1} were determined for the carbonyl compounds benzaldehyde, glyoxal, methylglyoxal, and pyruvic acid. Specific quantum yields were mostly available for those compounds which are prone to absorb in the solar actinic spectrum and have therefore been extensively investigated with regard to their photochemistry, such as carbonyls and nitro compounds. For the studied alcohols and carboxylic acids for which no quantum yield was available in the literature, we determined maximum photolysis rates of $<2×10^{-5}$ s^{-1} with assumed quantum yields of 1. These loss rates do not substantially affect the chemistry and calculated concentrations over the course of the experiment, so that over-corrections of the photolytic losses are negligible.~~

4.1.2 Wall Losses

The wall loss rates which were determined empirically in this work for dry air at T = 298±1 K (Table S8) ranged between $4.54±1.80×10^{-6}$ s^{-1} (benzaldehyde) and $8.53±0.68×10^{-5}$ s^{-1} (*p*-hydroxybenzaldehyde). These orders of magnitude are in line with reported vapor loss rates on Teflon films in the literature (McMurry and Grosjean, 1985; Zhang et al., 2015).

~~The dependence of the measured wall loss rates of the studied oxygenated compounds on their molecular properties is shown in Fig. 5. The most influential parameter was the vapor pressure, which has already been shown previously to be inversely related to wall losses in Teflon chambers (Yeh and Ziemann, 2015; Zhang et al., 2015). In addition, we found a dependency on the molecular weight of the compounds, which is similar to other studies where partitioning to walls increased with the carbon number of the molecule (Matsunaga and Ziemann, 2010; Yeh and Ziemann, 2015). Finally, the wall loss was also influenced by the degree of functionalization and oxygenation (Lumiaro et al., 2021; Matsunaga and Ziemann, 2010; Yeh and Ziemann, 2015), considered in this study in terms of the oxygen-to-carbon ratio (O:C ratio).~~ The dependence of wall losses on molecular properties has been investigated and described for other Teflon chambers by sophisticated gas-wall partitioning models, which are for example based on the ideal gas law or on related parameters such as the saturation concentration (e.g.

Matsunaga and Ziemann, 2010; Ye et al., 2016; Yeh and Ziemann, 2015; Zhang et al., 2015). These models also reveal fundamental relationships, such as an inverse link between wall loss rates and vapor pressure, and an increase in wall losses with increasing carbon number and molecular size as well as with an increasing degree of functionalization. Building onto these findings, we developed a simple parameterization that is based on readily accessible parameters and expresses the wall losses of the toluene photooxidation products as first order processes with a fixed rate constant. We tested several fundamental molecular properties alone and in combination for their ability to describe the empirical loss rates. The most influential parameter was the vapor pressure. We obtained the best fit (R^2 = 0.80) when also including the molecular weight and oxygen-to-carbon ratio (O:C ratio) and reducing the impact of the vapor pressure by taking its square root (Fig. 5). ~~Here, w~~We therefore propose ~~a~~the parameterization for the wall loss rate ~~(R^2 = 0.80) as~~ given in Eq. (~~5~~7):

$$WL = a \times e^{(b \times P)} \quad (7\text{~~5~~a})$$

$$P = \frac{\sqrt{v_p}}{MW \times OC} \quad (7\text{~~5~~b})$$

where WL is the wall loss rate in s^{-1}, a is 6.49×10^{-5} s^{-1}, b is -19.68 $(\sqrt{mmHg})^{-1}$ g mol^{-1}, and P is the parameter in $\sqrt{mmHg}$ g^{-1} mol. The parameter P entails the vapor pressure v_p in mmHg, the molecular weight MW in g mol^{-1}, and the dimensionless O:C ratio OC. We observed a different trend for nitro compounds without further functional groups, and did not include their empirical wall loss rates for fitting the regression. The empirical and parameterized wall loss rates and their relative deviations are summarized for all oxygenated products in Table S8. With the exception of benzaldehyde and methylglyoxal, which both have small empirical loss rates with high uncertainties (<2×10^{-5} s^{-1}, uncertainty of 40 % and 32 % respectively), the empirical and parameterized values agree within 30 %.

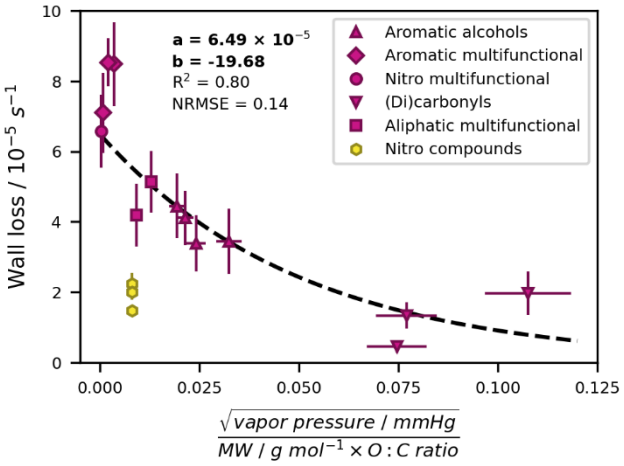

Figure 5: Wall loss parameterization based on empirically determined wall loss rates. Error bars along the y-axis are the normalized root mean squared errors (NRMSEs) of the individual exponential regressions for the empirical wall loss determination. Error bars along the x-axis show a generic 10 % error resulting from uncertainties in available vapor pressure data. Oxidation products with different functional groups are distinguished. Nitro compounds (nitrotoluene isomers and (nitromethyl)benzene) were not included as model input.

In a larger context, the presented parameterization provides the possibility to describe the chamber-specific wall loss of a multitude of oxygenated photooxidation products which cannot be tested empirically. For higher internal consistency, we used the parameterized loss rates for all studied compounds with hydroxy, carboxyl, or carbonyl groups. These values are associated with an uncertainty of 14 % according to the normalized root mean square error (NRMSE) of the parameterization.

The application of the parameterization is limited in that reasonably well-constrained vapor pressure is required to make an explicit prediction. In the absence of such data, the loss rate can be approximated by generic values for clusters of compounds with the same functional group composition. Here, six groups of compounds could be clearly distinguished (see also Table S8). Using the fitted wall loss rate of all associated compounds, we derived generic loss rates (mean ± standard deviation) of $1.23\pm0.32\times10^{-5}$ s^{-1} for carbonyls and dicarbonyls (benzaldehyde, glyoxal, methylglyoxal), $4.04\pm0.38\times10^{-5}$ s^{-1} for monohydric aromatic alcohols (cresols and benzyl alcohol), $5.23\pm0.19\times10^{-5}$ s^{-1} for aliphatic multifunctional compounds (glycolaldehyde, pyruvic acid), $6.23\pm0.14\times10^{-5}$ s^{-1} for aromatic acids and multifunctional compounds (benzoic acid, p-methylcatechol, p-hydroxybenzaldehyde), and 6.44×10^{-5} s^{-1} for nitro compounds with additional hydroxy groups (nitrocresol isomers). The order of the associated wall loss rates (multifunctional compounds and acids > alcohols > carbonyls) agrees well with previous studies which have investigated the effect of the type (Yeh and Ziemann, 2015) and number (Lumiaro et al., 2021) of functional groups on partitioning coefficients of gaseous compounds to walls and particles. Although not included in the parameterization, nitro compounds can be described by their mean empirical wall loss rate of $1.90\pm0.32\times10^{-5}$ s^{-1}.

It should be noted that the presented wall loss rates as well as their parameterization are valid only for dry conditions and a temperature of 298 K, but may differ if experimental conditions change (Grosjean, 1985; Zhang et al., 2015). Furthermore, both the time frame over which we determined the wall losses empirically and the conducted photooxidation experiments were limited to three to four hours. On longer time scales, desorption processes, wall saturation, and equilibrium between the gas phase and the chamber walls need to be taken into account more specifically (Yeh and Ziemann, 2015; Zhang et al., 2015).

4.1.3 Cleanliness and Quality Control

To minimize carry-over effects and quantify chamber contamination, the cleanliness of the chamber was examined carefully prior to each experiment. During these checks from the pre-cleaned chamber, the product concentrations measured in the irradiated chamber and in the dark chamber agreed well within the instrumental error. Hence, there was no substantial desorption of residual compounds from the irradiated walls. In addition, we measured the experimental blank values from the filled chamber to prevent overestimations of product concentrations due to impurities and analytical artefacts related to the added reagents. For most compounds, these blank values were in a similar range as their respective LODs, by several orders of magnitude smaller than their typical concentrations during the photooxidation experiments, and did not differ substantially among the different runs (Fig. 6).

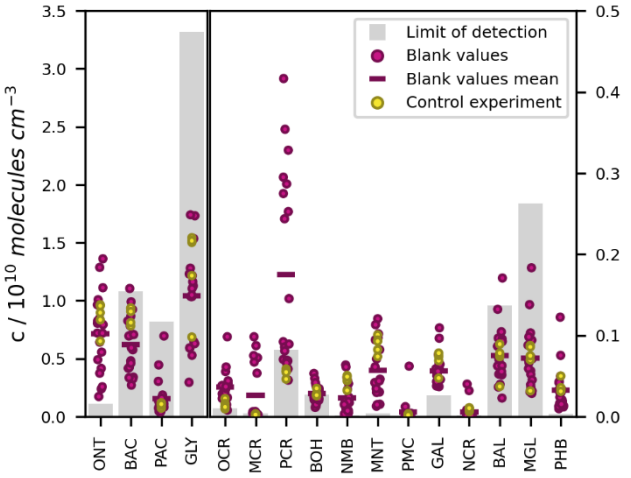

Figure 6: LODs, blank values, and control experiment concentrations of the toluene photooxidation products measured by SPME-GC-MS. The LODs refer to the on-line measurement from the chamber. Blank values are shown for 18 separate experiments. The measured concentrations in the toluene-free control experiment are shown without blank subtraction or further loss corrections. All values are given as concentrations in molecules cm^{-3}, because the LODs for the SPME-GC-MS were derived as fixed concentrations, whereas the corresponding mixing ratios varied between the experiments due to the ambient temperature and pressure.

To confirm that the observed product formation during the photooxidation experiments is solely attributable to the reaction of toluene with OH radicals, we conducted an additional control experiment in the absence of toluene (Table 2). The concentrations obtained in the course of this experiment are comparable to the measured blank values (Fig. 6). Hence, we conclude that the reacted toluene was the unique source of the products in our setup.

4.1.4 Best Practice for Future Work

For future work, we propose a best practice procedure to re-evaluate chamber properties when experimental conditions change and time progresses.

- The qualitative pattern of the solar simulator emission spectrum is stable over time, yet we found a difference in the absolute photon flux by about a factor of 3 over the course of roughly one decade (Fig. 4a). Therefore, the spectrum should be recorded regularly. More frequent checks are needed when there is high experimental throughput or when new HMI lamps are inserted, since each lamp is unique and metal depositions on the glass lead to a relatively quick loss of intensity at the beginning of the lamp lifetime (Bleicher, 2012).
- Wall losses need to be re-assessed (i) for experiments operated at different temperatures, (ii) for experiments performed in humid air, (iii) for new VOC photooxidation systems with different compound structures and properties, (iv) for new chambers when the Teflon body was replaced (see below), and (v) for longer periods of time and more complex wall interactions if the experimental duration is increased.
- Prior to every single experiment, the chamber needs to be carefully cleaned and evaluated for possible artefacts and contamination by recording chamber blank values. For each set of experiments, at least one control experiment without the VOC precursor should be performed. As the chamber is completely evacuated at the end of any experiment, it should still be empty when the next experiment is started. If this is not the case, leaks in the chamber body need to be fixed. A new Teflon body should be constructed after working with high concentrations of sticky compounds and/or NO_x to avoid carry-over or the unintended formation of photochemically relevant species such as HONO (Bell et al., 2023; Rohrer et al., 2005).

4.2 Analytical Performance Evaluation: SPME-GC-MS and PTR-ToF-MS

While it was possible to quantify the isomers of functionally diverse photooxidation products at ppbv and pptv levels with the double derivatization SPME-GC-MS method, its temporal resolution was limited to 41 minutes. In contrast, PTR-ToF-MS averaged scans were monitored every minute with high precision and additional information about potential photooxidation products yet no possibility to distinguish between isomers. Thus, here we combined the two analytical tools to extend and improve the information derived from the conducted photooxidation experiments, merging isomeric information from the SPME-GC-MS and a high time resolution from the PTR-ToF-MS.

4.2.1 SPME-GC-MS Analysis and Calibration of Toluene Products

For the compounds which could be analysed efficiently with the on-line SPME-GC-MS method, the determined calibration factors, associated errors, and LODs are listed in Table 3. The calibration curves are shown exemplary for the ring-retaining first generation products in Fig. 7. No saturation effect is apparent in these curves, indicating that the calibration interval

between c = 0 − 12.3×10^{10} molecules cm^{-3} is still within the linear range of the SPME fibre. As all tested toluene products were injected jointly during the calibration, the total mixing ratio of the products reached about 85 ppbv for the highest calibration level. During the NO_x-free photooxidation experiments, the loss of toluene and hence the maximum production of oxygenated compounds (as C_7 equivalents) was by about a factor of 4 or more lower than that, so that the sampling capacity of the fibre was likely not exceeded. We observed the lowest sensitivity for compounds undergoing both derivatization steps (glycolaldehyde, pyruvic acid, *p*-hydroxybenzaldehyde) and the highest instrumental sensitivity for the non-derivatized nitrotoluene isomers and (nitromethyl)benzene. This is partly due to the selection of ions for the SIM mode and the relatively more complex mass spectrum after derivatization. While non-derivatized compounds were monitored on predominant ions in their mass spectra, the SIM masses of the derivatized compounds were chosen more specifically to represent typical adducts with all involved derivatization reagents.

The instrumental error was highest for the carbonyls benzaldehyde, glyoxal, and methylglyoxal that were derivatized by PFBHA and corrected by acetophenone-d_8. Along with the two carboxylic acids, benzoic acid and pyruvic acid, these compounds furthermore had the highest LODs. This is in contrast to the study by Borrás et al. (2021), where carbonyls could be determined with great precision, and where especially glyoxal performed very well. Probably, this difference results from the distinct experimental setups of the BATCH Teflon chamber and the EUPHORE chamber, respectively. In particular, the transfer line in the present work was longer (~ 6 m), heated to 50°C instead of 80 °C, and made from PTFE instead of sulfinert material. Additionally, the periodic sampling process allowed only 3 minutes of equilibration prior to extraction. We acknowledge that these conditions limit our ability to analyse sticky compounds with regard to sensitivity and sample-to-sample variability (Fig. S9). Furthermore, during preliminary stability and optimization tests, we sometimes observed declining responses of PFBHA and the associated analytes over time, either due to reagent depletion or fibre degradation (Fig. S10). We avoided such effects in the experimental data by checking the fibre condition prior to each experiment and by conducting relatively short experiments with not more than five samples. Still, we note that the derivatization with PFBHA may be less robust than the derivatization with MSTFA/TMCS. Although such effects should be accounted for by the ISTD correction, acetophenone-d_8 as the selected ISTD may be too structurally different from the photooxidation products with regard to aromaticity and the type of carbonyl group to be able to sufficiently correct for pronounced methodological variations.

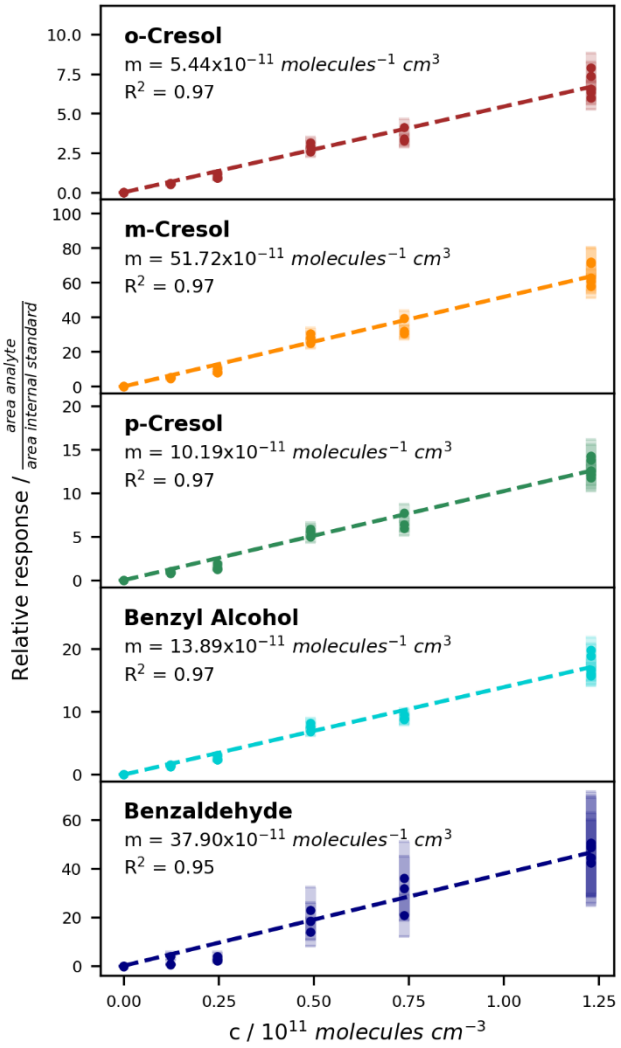

Figure 7: Calibration curves for the ring-retaining first generation products of toluene with the ISTD correction. The relative responses are plotted against the concentration in the chamber. Uncertainty areas represent the instrumental error.

The calibration solutions were prepared in ACN because (i) all compounds were solvable at the target concentrations, and (ii) ACN contains no functional groups that could scavenge the derivatization reagents when present in excess. However, this choice of solvent led to a substantial difference of the chamber matrix between the calibration and the experiments. In the present study, any potential matrix-induced changes in the instrumental sensitivity were compensated for by the on-line ISTD correction. Additionally, matrix-specific blank samples were subtracted both in the calibration (injection of ACN into chamber without dissolved analytes) and the experiments (filled chamber prior to irradiation) to account for possible variations in instrumental offsets. To experimentally confirm the validity of the performed calibration, joint stock solutions of the cresol

isomers, benzyl alcohol, benzaldehyde, glyoxal, and methylglyoxal were prepared in ACN and water respectively (c = 0.5 mM). For each solvent, 125 µL of the stock solution were injected into the chamber and measured by SPME-GC-MS. For all tested compounds, the uncertainty ranges of the mean relative responses of the two solutions overlapped. Hence, any potential solvent effect was within the instrumental error, and artefacts related to the presence of ACN can be excluded.

Table 3: Calibration factors, errors, and LODs for the compounds analysed with the on-line SPME-GC-MS method. The uncertainty of the slope was derived from the standard error of the slope with a 95 % confidence interval. R^2 is the coefficient of determination of the regression performed for the calibration. The instrumental error (Instr. Err.) is the mean RSD of all calibration levels. The quantification error (Quant. Err.) includes the instrumental error, the calibration error, and the experimental error. The LODs for the SPME-GC-MS were derived as fixed concentrations in molecules cm^{-3}, whereas the corresponding mixing ratios varied between the experiments due to the ambient conditions. As information for the reader, the LOD in pptv is shown here for T = 298 K and standard pressure.

	Calibration		Relative Error		Limit of Detection (LOD)	
Compound	Slope / molecules^{-1} cm^3	R^2	Instr. Err. / %	Quant. Err. / %	LOD / molecules cm^{-3}	LOD / pptv
OCR	$5.44\pm0.47\times10^{-11}$	0.97	12	24	1.06×10^{8}	4.3
MCR	$5.17\pm0.43\times10^{-10}$	0.97	12	24	3.49×10^{7}	1.4
PCR	$1.02\pm0.08\times10^{-10}$	0.97	13	24	8.21×10^{8}	33.4
BOH	$1.39\pm0.11\times10^{-10}$	0.97	10	23	2.66×10^{8}	10.8
ONT	$6.94\pm0.53\times10^{-7}$	0.98	7	22	1.11×10^{9}	45.1
NMB	$1.64\pm0.07\times10^{-6}$	0.99	5	21	1.45×10^{7}	0.6
MNT	$9.05\pm0.43\times10^{-7}$	0.99	5	21	4.14×10^{7}	1.7
BAC	$8.66\pm1.22\times10^{-11}$	0.93	31	37	1.08×10^{10}	438.9
PMC	$4.44\pm0.64\times10^{-11}$	0.91	15	25	8.94×10^{6}	0.4
GAL	$6.55\pm0.82\times10^{-11}$	0.94	12	24	2.63×10^{8}	10.7
NCR[(a)]	$3.01\pm0.39\times10^{-10}$	0.94	14	25	1.42×10^{7}	0.6
PAC	$8.81\pm1.38\times10^{-12}$	0.91	16	26	8.20×10^{9}	333.2
BAL	$3.79\pm0.44\times10^{-10}$	0.95	42	47	1.37×10^{9}	55.6
GLY	$2.02\pm1.05\times10^{-11}$	0.34	52	56	3.32×10^{10}	1349.5
MGL	$3.59\pm0.47\times10^{-10}$	0.94	42	47	2.63×10^{9}	106.8
PHB	$4.72\pm0.73\times10^{-12}$	0.92	26	33	3.26×10^{7}	1.3

[(a)] *Evaluated as the average concentration of both 2-nitro-p-cresol and 6-nitro-m-cresol.*

Optimizing and testing the new SPME-GC-MS method, we also evaluated several compounds which we did not include for the characterization of the BATCH Teflon chamber due to insufficient sensitivity or poor transportation from the chamber to the instrument (Table S9). We observed some patterns that can be of general interest for method optimization of these compounds, as described in more detail in the Supplement S6.3.

4.2.2 SPME-GC-MS Fibre Effects and ISTD Addition

In the present setup, the comparability of different samples, of different experiments, and of the experimental period and the on-line calibration was maintained by the added ISTDs. ~~To validate the temporal stability of the permeation source, the enriched outflow was monitored over a period of one week by PTR-ToF-MS. The RSDs of the PI-normalized responses were as low as 5 % for phenol-d_6 and 6 % for acetophenone-d_8, confirming the suitability of the setup for on-line ISTD addition.~~ The PTR-ToF-MS data showed that the ISTDs in the permeation source outflow were stable over the course of one week, with RSDs of 5 % and 6 % for the PI-normalized responses of phenol-d_6 and 6 % for acetophenone-d_8 respectively. Hence, the variability of the ISTD responses measured by SPME-GC-MS (Fig. 8) is indicative for changes in the preparation of the derivatization efficiency, the performance of the GC-MS, and most importantly fibre effects.

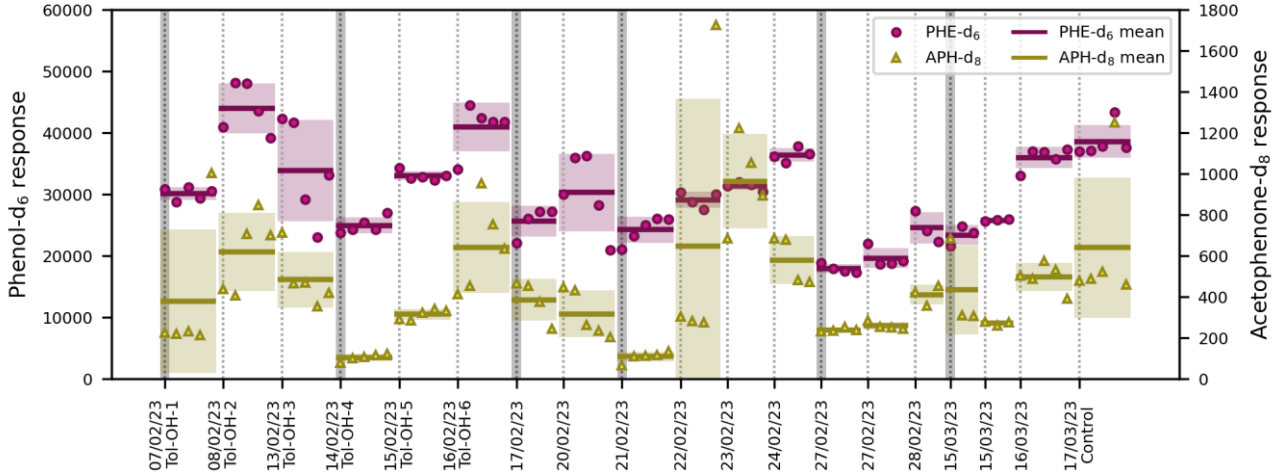

Figure 8: ISTD responses at the SPME-GC-MS over the entire experimental period in chronological order. Each individual marker represents one measurement of phenol-d_6 (PHE-d_6) or acetophenone-d_8 (APH-d_8), respectively. Only the experimental data are included, not the fibre conditioning and chamber cleanliness test measurements prior to each experiment. The ~~grey~~ dotted vertical ~~bars~~lines indicate the start of a new experiment. The insertion of a new SPME fibre is illustrated ~~in~~ with additional dark grey bars. The horizontal lines show the mean value of the entire experiment, with the standard deviations included as uncertainty areas.

For SPME sampling, as much as 200 assays per fibre have been reported in the literature (Martos and Pawliszyn, 1997). Here, the number of sampling cycles (PFBHA + on-line sampling + MSTFA/TMCS) conducted with a single fibre was in the range of about 20 – 30 (Fig. 8) and therefore considerably lower. This high fibre turnover is likely related to (i) the multitude of steps per sampling cycle, (ii) the active analyte extraction where the fibre is located perpendicular to a flow of air with a high velocity of 131 cm s^{-1}, and (iii) additional stress caused by the added derivatization reagents, especially TMCS.

The ISTD response often increased over the lifetime of a single SPME fibre (Fig. 8), suggesting either a carry-over effect or an enhanced performance of the fibres after repeated usage. This development typically reversed after three to four experiments, and fibres were exchanged when this was apparent in the preparatory work of a given experiment. While there

was no general trend over time, the SPME fibres differed in their overall extraction efficiency. The mean values of each fibre across all samples in the associated experiments were compared to indicate inter-fibre reproducibility, resulting in relative standard deviations of 17 % for phenol-d_6 and 25 % for acetophenone-d_8. This is in accordance with the inter-fibre variability of 18 % reported previously by Tumbiolo et al. (2004). It is important to note that with the controlled sequencing of the SPME autosampler system, the conditions and the duration of the extraction process were exactly the same for all samples. Thus, reproducibility could be achieved even for pre-equilibrium conditions when time control is critical.

Functional similarity is important for the ability of ISTDs to correct analytes under various conditions, yet just one ISTD was available for all compounds derivatized by each of the employed derivatization reagents, respectively. Most compounds derivatized by MSTFA/TMCS contained a hydroxy group and were functionally similar to phenol-d_6. The concentrations of the two studied carboxylic acids (pyruvic acid, benzoic acid) throughout the photooxidation experiments rarely exceeded their high LODs (Table 3), so that potential errors associated with insufficient resemblance to the assigned ISTD did not become relevant in the data evaluation. All carbonyls derivatized by PFBHA were corrected with acetophenone-d_8. As aldehydes are generally more reactive towards PFBHA than ketones (Jang and Kamens, 1999), acetophenone-d_8 is likely to be derivatized less effectively if there is a strong competition for the reagent (Fig. S10). In that case, concentrations of the aldehyde products would be overestimated. We therefore recommend a broader range of more functionally diverse ISTDs for future applications. Nevertheless, even with the available ISTDs and regardless of the class of compounds, we achieved improved fit qualities (R^2) of the calibration curves upon normalization of the instrumental response to the assigned ISTD (see calibration curves with ISTD correction in Fig. 7 and without ISTD correction in Fig. S11). This indicates an advanced method precision.

4.2.3 PTR-ToF-MS Calibration and Instrumental Inter-Comparison

The PI-normalized sensitivities, instrumental uncertainties, and LODs of the toluene photooxidation products calibrated for the PTR-ToF-MS are listed in Table S6. Overall, the ring-retaining compounds had the highest instrumental sensitivity. In contrast, the sensitivity of glyoxal on *m/z* 59.0041 was very low and barely quantifiable. Firstly, this is due to its low proton affinity of 161.41 – 165.06 kcal mol^{-1} that barely exceeds the proton affinity of water (Wróblewski et al., 2007). Secondly, we observed fragmentation of glyoxal to formaldehyde on *m/z* 31.0145, described also by Stönner et al. (2017). However, as formaldehyde can occur as a product of toluene photooxidation (Seuwen and Warneck, 1996; Wagner et al., 2003) but could not be determined sufficiently well using the on-line SPME-GC-MS method (Table S9), we had no possibility to differentiate between glyoxal and formaldehyde on that mass, and therefore measured glyoxal on its more specific protonated mass.

By performing separate calibrations for the cresols and benzyl alcohol, we could determine isomer-specific sensitivities (Table S6). We found the highest sensitivities for *o*-cresol and *m*-cresol, while the sensitivity of *p*-cresol was by about a factor of 2.5 lower. Benzyl alcohol did not show any signal on *m/z* 109.0626 and thus did not contribute to the sum signal and was excluded

from the weighted calibration. Instead, it fragmented to *m/z* 91.0522, which is in accordance with the literature (Yeoman et al., 2021) and probably indicates the formation of the benzyl radical after abstraction of water from the protonated molecule. As this fragment is unspecific, we did not evaluate it further. The isomer-specific calibration was performed with relative abundances of 0.741 for *o*-cresol, 0.04 for *m*-cresol, and 0.221 for *p*-cresol~~, and 0.04 for benzyl alcohol~~ (Sect. 4.3.2). As *o*-cresol is by far the most abundant isomer, its contribution to the weighted calibration factor on *m/z* 109.0626 was as high as 87 %. Overall, considering the relative abundances and the specific sensitivities of the individual isomers led to a 1.1547-fold increase of the calibration factor compared to the non-weighted calibration (Table S6).

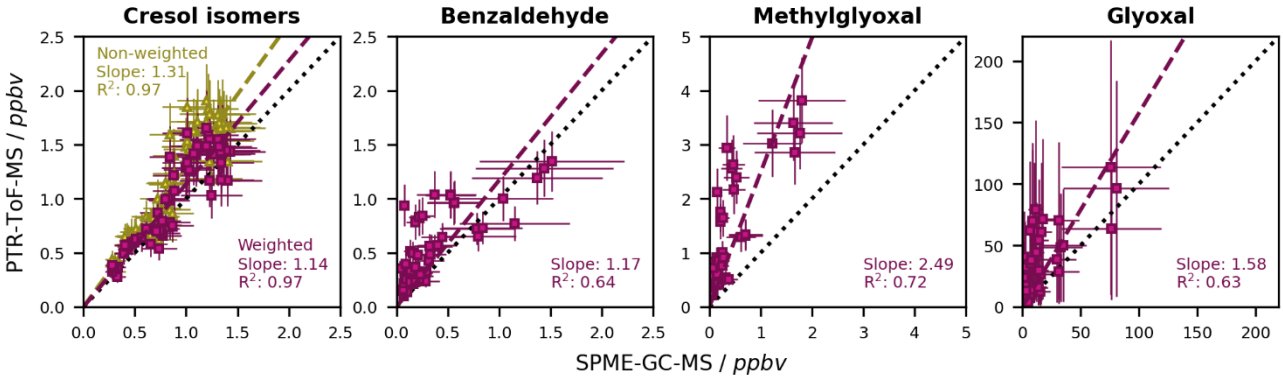

Figure 9: Comparison of the non-corrected mixing ratios of the toluene first generation products that were calibrated for both the SPME-GC-MS and the PTR-ToF-MS. The dashed black line represents a 1:1 fit. For both instruments, the mixing ratios as derived from the chamber calibration are shown. In case of the cresol isomers ~~and benzyl alcohol~~, the non-weighted and weighted calibrations for the sum of the isomers are distinguished. Error bars represent the quantification error of the respective instruments. Error bars of the sum of the ~~C_7H_8O~~ cresol isomers ~~(cresols and benzyl alcohol)~~ at the SPME-GC-MS are the weighted sum of the individual errors. The data are derived from 18 different experiments at different temperatures and both in the absence and presence of NO_x.

The difference between the PTR-ToF-MS data and the SPME-GC-MS data is shown for all calibrated compounds in Fig. 9. For the cresol isomers ~~and benzyl alcohol~~, the weighted calibration improved the coherence between the two instruments from 3125 % to 145 % deviation. Additionally, we determined the best fit quality (R^2) for these compounds, which likely relates to the good detectability and relatively low instrumental error of these compounds at both the SPME-GC-MS and the PTR-ToF-MS. The difference between the two instruments was below 20 % for all ring-retaining first generation products, and therefore within the quantification error of both instruments. For the dicarbonyls, on the other hand, there was a substantial instrumental disagreement. While the analysis of glyoxal at both the SPME-GC-MS and the PTR-ToF-MS was too uncertain to reliably interpret the observed relationship, the concentration of methylglyoxal was clearly higher when derived by PTR-ToF-MS. Possibly, this could be due to the lower selectivity of the PTR-ToF-MS and overestimations due to analytical artefacts. Especially for small molecules, such artefacts can relate to either isobaric interferences, or the actual formation of the target compounds within the instrument upon fragmentation of larger compounds (Michoud et al., 2018; Salazar Gómez et al., 2021). For instance, the C_4 and C_5 γ-dicarbonyl co-products of glyoxal and methylglyoxal photolyze rapidly in natural sunlight (Newland et al., 2019) and therefore are likely to produce substantial amounts of follow-up products in our experiments. The

MCM suggests the formation of photolytic products with a high degree of oxygenation (Bloss et al., 2005), some of which may well produce $C_3H_5O_2^+$ fragments. Oppositely, underestimated concentrations at the SPME-GC-MS could result for instance from insufficient equilibration in the SPME-GC-MS transfer line (Sect. 4.2.1).

As shown in Fig. 10, the combination of SPME-GC-MS data and weighted PTR-ToF-MS data effectively provides isomeric information on a high temporal resolution. This is particularly valuable for modelling and for gaining insights into chemical mechanisms. ~~To the best of our knowledge, this study marks the first demonstration of a correction of the sum signal based on both the abundance and the sensitivity of the individual isomers.~~ Rather than performing a separate weighted calibration for each time segment assigned to a specific SPME-GC-MS sample, we used a fixed relative abundance of the ~~C_7H_8O~~ cresol isomers for both the weighted calibration and the experimental data. This is a reasonable assumption, as their sinks in the BATCH Teflon chamber (wall losses, photolysis, secondary OH radical reactions) agree within 1~~2~~6 % (Tables S1, S7, S8). Accordingly, the isomeric distribution derived from the formation yields (including loss corrections) is equal to the average isomeric distribution calculated from the measured concentrations (excluding loss corrections). The variability of the isomeric distribution in the experimental SPME-GC-MS data ~~confirm that the variability of the isomeric distribution over the course of the conducted experiments~~ is only 1~~7~~3 % and hence within the quantification error. In addition to the simplicity of implementation, the adoption of a fixed relative abundance also makes the PTR-ToF-MS results less susceptible to outliers and the random error of the SPME-GC-MS data.

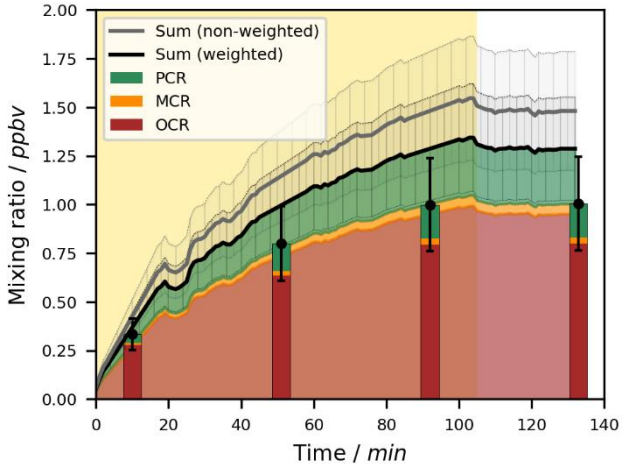

Figure 10: Time series of the cresol isomers ~~and benzyl alcohol~~ by SPME-GC-MS and PTR-ToF-MS. Data are shown for experiment Tol-OH-6 (T = 298±1 K, NO_x-free). No loss corrections were applied to the depicted data. The area shaded in yellow represents the period in which the chamber was irradiated. The sum signal of the PTR-ToF-MS is shown for both the weighted and the non-weighted calibration, with the quantification error shown as shaded area. For the weighted data set, the individual isomers are shown according to their fixed relative abundances. The error of the sum of the isomers in the SPME-GC-MS data is calculated as the weighted sum of the individual quantification errors. ~~In the depicted experiment, the sum of the isomers agrees exceptionally well between the two instruments, while the measured isomeric distribution deviates slightly from the fixed relative abundance.~~ Toluene products in this figure include *o*-cresol (OCR), *m*-cresol (MCR), and *p*-cresol (PCR)~~, and benzyl alcohol (BOH)~~.

4.3 Application: Product Study

The conducted experiments allowed us to validate the developed methods and to gain insight into the OH radical-induced photooxidation of toluene. Since the calculated product formation yields take into account compound- and chamber-specific losses and the ambient oxidation efficiency, they provide a bridge from individual experiments to generalizable mechanistic evaluations. Thus, our results can be placed in the context of previous studies and atmospheric chemistry models.

4.3.1 Loss Corrections and Error

The contribution of the three characterized loss processes (wall losses, photolysis, secondary OH radical reactions) to the ~~final~~ loss-corrected concentration differed over time and according to the experimental conditions. As shown for the NO_x-free experiment Tol-OH-6 in Fig. 11, the different losses gained in importance over the course of the experiment, and the fraction of the measured non-corrected data decreased accordingly. Furthermore, the absolute and relative contributions of the various loss corrections differed for the individual compounds. In the exemplary case of the ring-retaining first generation products, the cresol isomers and benzyl alcohol were affected mainly by wall losses and secondary reactions with OH radicals, whereas photolytic losses were relatively more important for benzaldehyde. An overview of the first order rate constants of all three loss processes for each of the analysed compounds is provided in Fig. S12.

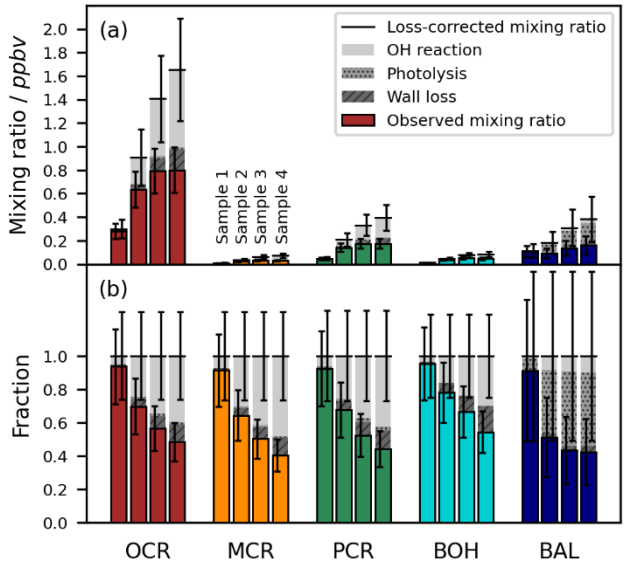

Figure 11: Contributions of the non-corrected data and each of the three included loss corrections (wall losses, photolysis, secondary OH radical reactions) to the ~~final~~ loss-corrected concentration. The displayed data refer to the SPME-GC-MS samples 1 to 4 in experiment Tol-OH-6 (T = 298±1 K, NO_x-free). The shares of the raw data and the losses are shown on **(a)** an absolute scale (mixing ratios~~, upper graph~~) and **(b)** on a relative scale (normalized to the ~~total~~ loss-corrected mixing ratio~~, lower graph~~). The error bars represent the compound-specific quantification errors of the non-corrected data. Toluene products in this figure include o-cresol (OCR), m-cresol (MCR), p-cresol (PCR), benzyl alcohol (BOH), and benzaldehyde (BAL).

The loss corrections introduced additional uncertainty in the final data sets. For the wall loss rates, we adopted the uncertainty of the parameterization (14 %) since we used the modelled values for all compounds. The error of the photolysis rates (38 %) resulted from the recorded spectrum, the uncertainty in the literature values used for the quantum yields and absorption cross sections, and temporal variations in the emission of the solar simulator. The uncertainty associated with secondary reactions of the analytes with OH radicals (19 %) was calculated from the quantification error of toluene, the error of the rate constant of toluene with OH radicals, and the error of the rate constants of OH radicals with the analytes. The total error of the loss-corrected concentrations was weighted and calculated for each data point separately to account for the variable contribution of the different loss processes (for details, see Supplement S7 with Table S10).

As proof-of-concept for the implemented correction scheme, we furthermore compared the measured and the loss-corrected data sets obtained by SPME-GC-MS and PTR-ToF-MS for different compounds and experiments (see Supplement S7 with Fig. S132 and S143). The absolute losses for each of the distinct loss processes as well as the total loss-corrected concentrations are in good agreement between the SPME-GC-MS and the PTR-ToF-MS data, indicating that the correction procedure is valid for both instruments in spite of their different temporal resolutions.

4.3.2 Formation Yields

The linear regressions performed for deriving the formation yields of the ring-retaining first generation products of toluene for T = 298±1 K in the absence of NO_x are shown in Fig. 12. For demonstration, and to be able to resolve the C_7H_8O isomers, we focus here mainly on the SPME-GC-MS data. The results obtained in this study are clustered according to the reaction channel and compared with the MCM predictions and literature values in Table 4.

For the cresol channel, we derived a sum yield of 10.8±2.5 %. This is in the low range of most reported values, but in close agreement with the 10 % yield obtained in another recent study by Zaytsev et al. (2019). The large discrepancy of the available literature values (9 − 52.9 %) can be explained by the high reactivity of the cresols and by their susceptibility to various physical and chemical losses that in turn are specific to the experimental setup and analytical technique (Klotz et al., 1998; Schwantes et al., 2017). Notably, the three highest cresol yields reported in the literature in the last 20 years were obtained theoretically (Wu et al., 2014) or under low-O_2 conditions (Baltaretu et al., 2009; Ji et al., 2017) that may disfavour the competing dicarbonyl channel (Jenkin et al., 2009; Newland et al., 2017). The very high yield of 52.9 % obtained by Seuwen and Warneck (1996) was obtained from experiments with toluene mixing ratios of about 1000 ppmv, limiting the transferability of these data to the real atmosphere. The isomeric distribution was previously reported in the order *o*-cresol > *p*-cresol > *m*-cresol (Klotz et al., 1998; Seuwen and Warneck, 1996; Smith et al., 1998). This pattern is well reproduced in the present work with yields of 8.0±1.8 %, 2.4±0.6 %, and 0.4±0.1 %, respectively. These yields correspond to a ratio of 74:4:22 for *o*-, *m*-, and *p*-cresol. As Seuwen and Warneck (1996) could not quantify the yield of *m*-cresol, and other studies evaluated the sum of *m*-

and *p*-cresol due to insufficient chromatographic separation (e.g. Moschonas et al., 1998), this study reports the first NO_x-free distribution of all the cresol isomers to the best of our knowledge.

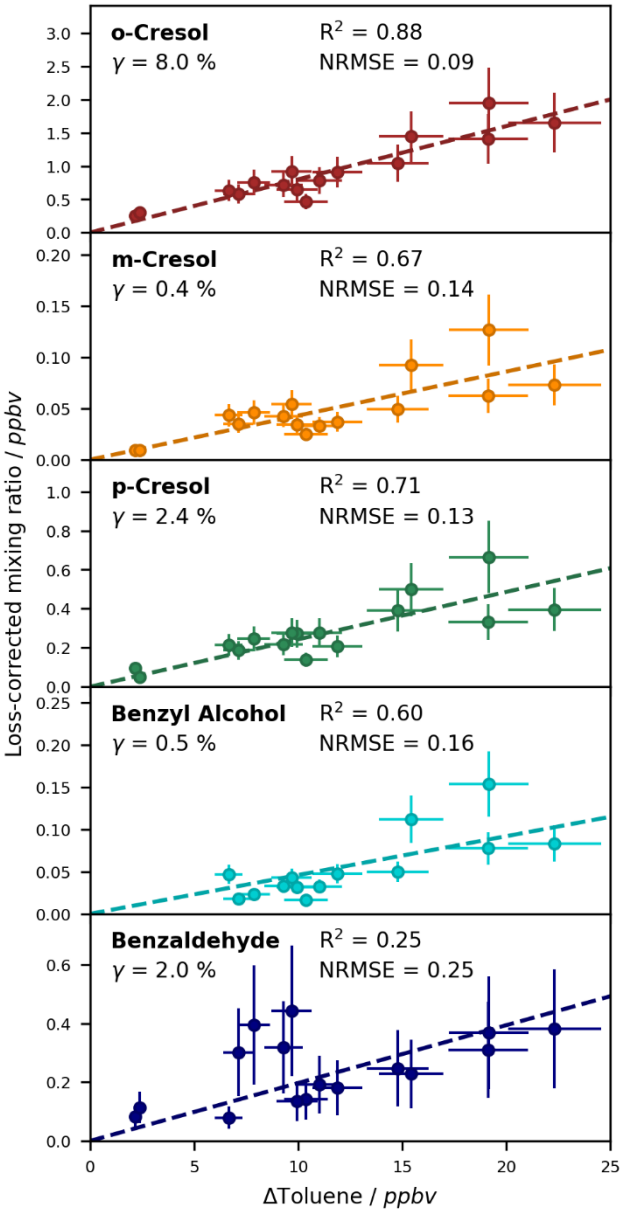

Figure 12: Yields of the ring-retaining first generation products of toluene, derived by linear regressions of the loss-corrected mixing ratio (including loss corrections for wall losses, photolysis, secondary OH radical reactions) against the monitored change in toluene. For each compound, the slope of the regression is equal to the formation yield. To perform the regressions, only experiments conducted at T = 298±1 K and in the absence of NO_x were used. Error bars represent the quantification error.

Table 4: Yields of the ring-retaining first generation products of toluene. The compounds are clustered according to the main channel, which in turn is listed as the sum of the associated products. All yields are given in %. Unless stated otherwise, the yields shown for this work are based on the SPME-GC-MS data. The error of these yields was calculated from the propagation of the NRMSEs of the linear regressions, the calibration error, and the quantification error of toluene. The yields in the MCM refer to the latest representation of the toluene chemistry in MCM v3.1 (Bloss et al., 2005). The MCM does not distinguish between the cresol isomers, while in the abstraction channel, the product yields depend on the chemistry of the preceding peroxy radical. Underlined references refer to NO_x-free studies, while all other cited yields were obtained in the presence of NOx. The asterisk * indicates computational values, as presented by Wu et al. (2014). The instrumental techniques used in the cited literature were chemical ionization mass spectrometry (Baltaretu et al., 2009; Ji et al., 2017; Zaytsev et al., 2019), differential optical absorption spectroscopy (Klotz et al., 1998), gas chromatography with flame ionization detector (Atkinson et al., 1983, 1989; Atkinson and Aschmann, 1994; Moschonas et al., 1998; Seuwen and Warneck, 1996; Smith et al., 1998), offline determination of carbonyls after derivatization (Seuwen and Warneck, 1996; Smith et al., 1998), and tandem mass spectrometry (Dumdei et al., 1988). The literature values presented here provide a comprehensive overview of relevant data; however, we acknowledge that there may be additional relevant studies beyond those included in this table.

Channel, Compound	Formation yields in %			
	This work	MCM	Literature	References
Cresol	10.8±2.5	18	9−52.9	9 (Moschonas et al., 1998), 10 (Zaytsev et al., 2019), 17.9 (Smith et al., 1998), 17.9 (Klotz et al., 1998), 25.2 (Atkinson et al., 1989), 28.1 (Baltaretu et al., 2009), 32.0* (Wu et al., 2014), 39.0 (Ji et al., 2017), 52.9 (Seuwen and Warneck, 1996)
OCR	8.0±1.8	n.a.	6−38.5	6 (Moschonas et al., 1998), 12.0 (Klotz et al., 1998), 12.3 (Smith et al., 1998), 12.3 (Atkinson and Aschmann, 1994), 13.1 (Atkinson et al., 1983), 20.4 (Atkinson et al., 1989), 38.5 (Seuwen and Warneck, 1996)
MCR	0.4±0.1	n.a.	≤0.4 −2.7	≤0.4[(a)] (Seuwen and Warneck, 1996), 2.6 (Smith et al., 1998), 2.7 (Klotz et al., 1998)
PCR	2.4±0.6	n.a.	3.0−14.4	3.0 (Smith et al., 1998), 3.2 (Klotz et al., 1998), 14.4 (Seuwen and Warneck, 1996)
Abstraction[(b)]	≥2.5±0.7 ≥5.1±1.8[(c)]	7	≥6.15−9.4	≥6.15 (Smith et al., 1998), ≥7.7 (Seuwen and Warneck, 1996), ≥9.4 (Moschonas et al., 1998)
BOH	0.5±0.1	n.a.	0.15−2.4	0.15 (Smith et al., 1998), 1 (Moschonas et al., 1998), 2.4 (Seuwen and Warneck, 1996)
BAL	2.0±0.6 4.6±1.7[(c)]	n.a.	4.9−11.3	4.9 (Baltaretu et al., 2009), 5.0 (Dumdei et al., 1988), 5.3 (Seuwen and Warneck, 1996), 5.8 (Klotz et al., 1998), 6.0 (Smith et al., 1998), 6.45 (Atkinson et al., 1989), 7.0* (Wu et al., 2014), 7.3 (Atkinson et al., 1983), 8.4 (Moschonas et al., 1998), 9 (Zaytsev et al., 2019), 11.3 (Ji et al., 2017)

[(a)] Without correction for secondary losses.
[(b)] The MCM v3.1 yield encompasses all possible products of the abstraction channel. For the values obtained in this work as well as for the cited literature values, the sum of only benzyl alcohol and benzaldehyde is compiled.
[(c)] PTR-ToF-MS data set for benzaldehyde.

The yield of benzyl alcohol determined in this work (0.5±0.1 %) is within the range of the few reported values (Moschonas et al., 1998; Seuwen and Warneck, 1996; Smith et al., 1998), confirming it as a relevant first generation product in the abstraction channel. While the yield of benzyl alcohol was always found to be lower than that of benzaldehyde, it is uncertain whether it

is more abundant (Seuwen and Warneck, 1996), less abundant (Smith et al., 1998), or in a similar range (this work) compared to its isomer *m*-cresol. This is important for the interpretation of purely mass-spectrometric approaches that often neglect benzyl alcohol and assign the sum signal exclusively to the *o*-, *m*-, and *p*-isomers of cresol (e.g. Baltaretu et al., 2009; Ji et al., 2017; Zaytsev et al., 2019). While we found that benzyl alcohol does not contribute to the sum signal in H_3O^+ soft ionization, its sensitivity in other ionization techniques should be verified to avoid overestimated cresol yields.

As the dominant product in the H abstraction channel, benzaldehyde has been studied for many decades. The yield obtained in this work using the SPME-GC-MS data (2.0±0.6 %) is smaller than any of the reported values both in the presence and in the absence of NO_x. Notably, the regression performed for benzaldehyde has a relatively high uncertainty (NRMSE = 0.25, Fig. 12), which is in line with the discussed instrumental variability of the aldehydes determined with the on-line SPME-GC-MS method in our setup. As there are no relevant isomers or spectral interferences for benzaldehyde, we could refer to the PTR-ToF-MS measurements as well. These data resulted in a yield of 4.6±1.7 % (Fig. 13). The fact that this value is by more than a factor of 2 higher than the yield obtained using the SPME-GC-MS data relates to the observed difference in the measured concentrations (Fig. 9) that is further amplified by the applied loss corrections. The PTR-ToF-MS yield for benzaldehyde is in better agreement with the literature values, albeit still at the lower end. We conclude that in case of benzaldehyde, the SPME-GC-MS data set is too small to compensate for the instrumental error, and that the more precise PTR-ToF-MS data should therefore be used. Interestingly, the PTR-ToF-MS yield agrees reasonably well with the apparent outliers in the SPME-GC-MS data set in the range of Δtoluene = 7.0 – 9.8 ppbv (Fig. 12). These data correspond to the experiments Tol-OH-4 and Tol-OH-5, which in turn show the best intra-experimental stability of acetophenone-d_8 (Fig. 8). Although we lack definite proof that these effects are causally related, this observation nevertheless reinforces our recommendation to include internal standards for on-line analytical methods used in chamber experiments, and to select compounds with good stability and high resemblance to the analytes for correction.

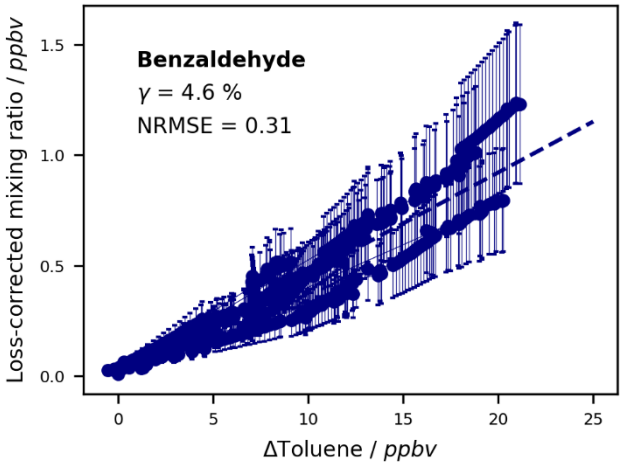

Figure 13: Benzaldehyde formation yield, derived by linear regression of the loss-corrected mixing ratio (including loss corrections for wall loss, photolysis, and reaction with OH radicals) against the monitored change in toluene. The slope of the regression is equal to the formation yield. To perform the regression, only experiments conducted at T = 298±1 K and in the absence of NO_x were used. Error bars represent the uncertainty of the loss-corrected data.

5 Conclusion

In this work, we set up an indoor atmospheric simulation chamber to study multifunctional photooxidation products in the gas phase by on-line SPME-GC-MS and PTR-ToF-MS. Specifically, the products emerging from the reaction of toluene with OH radicals were investigated and used as reference compounds to characterize the chamber properties and the instrumental capabilities. In the new chamber, controlled experiments could be performed with realistic photon fluxes and OH radical concentrations. We characterized the photolysis rates (1.77×10^{-8} – 3.02×10^{-4} s^{-1}), wall losses (4.54×10^{-6} – 8.53×10^{-5} s^{-1}), and secondary OH radical reactions of photooxidation products with diverse functional groups. The wall losses were determined empirically, and found to be dependent on fundamental molecular properties. We parameterized the loss rates accordingly, opening up the possibility of accurately characterising the losses of compounds for which no authentic standards are available. In addition to the wall losses, we calculated photolytic and reactive losses using available literature values of the absorption cross sections and quantum yields, and the rate constants for the reactions with OH radicals, respectively.

The SPME-GC-MS method with on-fibre PFBHA and MSTFA derivatization enabled the on-line analysis of fragile oxygenated compounds with high sensitivity and isomeric resolution. Due to the continuous addition of functionally similar internal standards from a customized permeation source, variations in the SPME fibre extraction efficiency were effectively accounted for. Our method worked particularly well for the studied aromatic alcohols. The carbonyl compounds were associated with a higher instrumental error due to the limitations of the experimental setup regarding the on-line analysis of sticky compounds. For future applications, we recommend a wider range of internal standards to facilitate a higher structural resemblance to the analytes. Combining the SPME-GC-MS data with the PTR-ToF-MS data, we could gain additional insight into temporal trends and cross-compare the absolute concentrations. We calibrated the main first generation products of toluene for both instruments, and found good agreement for ~~the ring retaining products (~~the cresol isomers~~, benzyl alcohol,~~ and benzaldehyde~~)~~. We further demonstrated that the sensitivity of the PTR-ToF-MS for different structural isomers can vary substantially. For the cresols~~ and benzyl alcohol~~, we therefore applied a weighted calibration factor based on the determined isomer-specific sensitivities and the distribution of the isomers as obtained by the SPME-GC-MS data. This led to an improved instrumental agreement, and allowed us to derive continuous time series of the individual isomers. For a wide range of applications based on mass-spectrometric techniques, it may be worth examining and potentially incorporating isomer-specific sensitivities if the relative distribution is known and calibration standards are available.

For method validation purposes, we focused on the initial photooxidation period to evaluate the primary chemistry and the dominant first generation products of toluene. Taking into account compound-specific physical and chemical losses, we

obtained product formation yields under NO_x-free conditions at T = 298±1 K for *o*-cresol (8.0±1.8 %), *m*-cresol (0.4±0.1 %), *p*-cresol (2.4±0.6 %), benzyl alcohol (0.5±0.1 %), and benzaldehyde (4.6±1.7 %). These results are comparable to previous studies. Jointly, the experimental design, instrumental analysis, and data processing approaches that we have tested and optimized in this work provide a means of determining the formation yields of the individual isomers of photooxidation products with different functional groups with good accuracy.

Code and data availability

The code and data used in this study are available by request to the corresponding authors.

Author contributions

AN acquired funding, conceptualised the project, and provided supervision. EB and AM provided methodological training at the EUPHORE chamber. With support from AN, FL set up the methodology in Bayreuth, performed the experiments, validated the results, and was in charge of the curation, formal analysis, and visualisation of the data. FL and AN prepared the manuscript with contributions from all co-authors.

Competing interests

The authors declare that they have no conflict of interest.

Acknowledgements

We thank the workshop of the University of Bayreuth for manufacturing the SPME-GC-MS sampling cell. Also, we thank Andrej Einhorn and Agnes Bednorz for their support regarding the technical setup and the experimental work. We thank Sergej Bleicher for helpful discussions about the solar simulator emission spectrum, and Cornelius Zetzsch for advice regarding hydroxyl radical generation. We are grateful for the financial support of the German Research Foundation (Deutsche Forschungsgemeinschaft, DFG) for the PTR-ToF-MS (Großgeräteantrag, project number: 495692966) and the ACTRIS TNA for practical training at the EUPHORE chambers (supported by the European Commission under the Horizon 2020 – Research and Innovation Framework Programme, H2020-INFRADEV-2019-2, Grant Agreement number: 871115). This open access publication was funded by the Open Access Publishing Fund of the University of Bayreuth.

References

Alfarra, R., Camredon, M., Cazaunau, M., Doussin, J.-F., Fuchs, H., Jorga, S., McFiggans, G., Newland, M. J., Pandis, S., Rickard, A. R., and Saathoff, H.: Physical and Chemical Characterization of the Chamber, in: A Practical Guide to Atmospheric Simulation Chambers, edited by: Doussin, J.-F., Fuchs, H., Kiendler-Scharr, A., Seakins, P., and Wenger, J., Springer International Publishing, Cham, 73–111, https://doi.org/10.1007/978-3-031-22277-1_2, 2023.

Altshuller, A. P.: Ambient Air Hydroxyl Radical Concentrations: Measurements and Model Predictions, JAPCA, 39, 704–708, https://doi.org/10.1080/08940630.1989.10466556, 1989.

Arthur, C. L. and Pawliszyn, Janusz.: Solid phase microextraction with thermal desorption using fused silica optical fibers, Anal. Chem., 62, 2145–2148, https://doi.org/10.1021/ac00218a019, 1990.

Atkinson, R. and Aschmann, S. M.: Products of the gas-phase reactions of aromatic hydrocarbons: Effect of NO_2 concentration, Int. J. Chem. Kinet., 26, 929–944, https://doi.org/10.1002/kin.550260907, 1994.

Atkinson, R., Carter, W. P. L., Darnall, K. R., Winer, A. M., and Pitts Jr., J. N.: A smog chamber and modeling study of the gas phase NO_x–air photooxidation of toluene and the cresols, Int. J. Chem. Kinet., 12, 779–836, https://doi.org/10.1002/kin.550121102, 1980.

Atkinson, R., Carter, W. P. L., and Winer, A. M.: Effects of pressure on product yields in the nitrogen oxide (NO_x) photooxidations of selected aromatic hydrocarbons, J. Phys. Chem., 87, 1605–1610, https://doi.org/10.1021/j100232a029, 1983.

Atkinson, R., Aschmann, S. M., Arey, J., and Carter, W. P. L.: Formation of ring-retaining products from the OH radical-initiated reactions of benzene and toluene, Int. J. Chem. Kinet., 21, 801–827, https://doi.org/10.1002/kin.550210907, 1989.

Baltaretu, C. O., Lichtman, E. I., Hadler, A. B., and Elrod, M. J.: Primary Atmospheric Oxidation Mechanism for Toluene, J. Phys. Chem. A, 113, 221–230, https://doi.org/10.1021/jp806841t, 2009.

Bartelt, R. J.: Calibration of a Commercial Solid-Phase Microextraction Device for Measuring Headspace Concentrations of Organic Volatiles, Anal. Chem., 69, 364–372, https://doi.org/10.1021/ac960820n, 1997.

Behnke, W., Holländer, W., Koch, W., Nolting, F., and Zetzsch, C.: A smog chamber for studies of the photochemical degradation of chemicals in the presence of aerosols, Atmospheric Environ. 1967, 22, 1113–1120, https://doi.org/10.1016/0004-6981(88)90341-1, 1988.

Bell, D., Doussin, J.-F., and Hohaus, T.: Preparation of Simulation Chambers for Experiments, in: A Practical Guide to Atmospheric Simulation Chambers, edited by: Doussin, J.-F., Fuchs, H., Kiendler-Scharr, A., Seakins, P., and Wenger, J., Springer International Publishing, Cham, 113–127, https://doi.org/10.1007/978-3-031-22277-1_3, 2023.

Berndt, T., Scholz, W., Mentler, B., Fischer, L., Herrmann, H., Kulmala, M., and Hansel, A.: Accretion Product Formation from Self- and Cross-Reactions of RO_2 Radicals in the Atmosphere, Angew. Chem. Int. Ed., 57, 3820–3824, https://doi.org/10.1002/anie.201710989, 2018.

Bleicher, S.: Zur Halogenaktivierung im Aerosol und in Salzpfannen, Doctoral thesis, University of Bayreuth, Bayreuth, 181 pp., 2012.

Bloss, C., Wagner, V., Jenkin, M. E., Volkamer, R., Bloss, W. J., Lee, J. D., Heard, D. E., Wirtz, K., Martin-Reviejo, M., Rea, G., Wenger, J. C., and Pilling, M. J.: Development of a detailed chemical mechanism (MCMv3.1) for the atmospheric oxidation of aromatic hydrocarbons, Atmospheric Chem. Phys., 5, 641–664, https://doi.org/10.5194/acp-5-641-2005, 2005.

Bohn, B., Rohrer, F., Brauers, T., and Wahner, A.: Actinometric measurements of NO_2 photolysis frequencies in the atmosphere simulation chamber SAPHIR, Atmospheric Chem. Phys., 5, 493–503, https://doi.org/10.5194/acp-5-493-2005, 2005.

Borrás, E., Tortajada-Genaro, L. A., Ródenas, M., Vera, T., Speak, T., Seakins, P., Shaw, M. D., Lewis, A. C., and Muñoz, A.: On-line solid phase microextraction derivatization for the sensitive determination of multi-oxygenated volatile compounds in air, Atmospheric Meas. Tech., 14, 4989–4999, https://doi.org/10.5194/amt-14-4989-2021, 2021.

Buxmann, J., Balzer, N., Bleicher, S., Platt, U., and Zetzsch, C.: Observations of bromine explosions in smog chamber experiments above a model salt pan, Int. J. Chem. Kinet., 44, 312–326, https://doi.org/10.1002/kin.20714, 2012.

Cabrera-Perez, D., Taraborrelli, D., Sander, R., and Pozzer, A.: Global atmospheric budget of simple monocyclic aromatic compounds, Atmospheric Chem. Phys., 16, 6931–6947, https://doi.org/10.5194/acp-16-6931-2016, 2016.

Carter, W. P. L., Winer, A. M., Darnall, K. R., and Pitts, J. N. Jr.: Smog chamber studies of temperature effects in photochemical smog, Environ. Sci. Technol., 13, 1094–1100, https://doi.org/10.1021/es60157a006, 1979.

Carter, W. P. L., Cocker, D. R., Fitz, D. R., Malkina, I. L., Bumiller, K., Sauer, C. G., Pisano, J. T., Bufalino, C., and Song, C.: A new environmental chamber for evaluation of gas-phase chemical mechanisms and secondary aerosol formation, Atmos. Environ., 39, 7768–7788, https://doi.org/10.1016/j.atmosenv.2005.08.040, 2005.

Charan, S. M., Buenconsejo, R. S., and Seinfeld, J. H.: Secondary organic aerosol yields from the oxidation of benzyl alcohol, Atmospheric Chem. Phys., 20, 13167–13190, https://doi.org/10.5194/acp-20-13167-2020, 2020.

Chu, B., Chen, T., Liu, Y., Ma, Q., Mu, Y., Wang, Y., Ma, J., Zhang, P., Liu, J., Liu, C., Gui, H., Hu, R., Hu, B., Wang, X., Wang, Y., Liu, J., Xie, P., Chen, J., Liu, Q., Jiang, J., Li, J., He, K., Liu, W., Jiang, G., Hao, J., and He, H.: Application of smog chambers in atmospheric process studies, Natl. Sci. Rev., 9, nwab103, https://doi.org/10.1093/nsr/nwab103, 2022.

Dumdei, B. E., Kenny, D. V., Shepson, P. B., Kleindienst, T. E., Nero, C. M., Cupitt, L. T., and Claxton, L. D.: MS/MS analysis of the products of toluene photooxidation and measurement of their mutagenic activity, Environ. Sci. Technol., 22, 1493–1498, https://doi.org/10.1021/es00177a017, 1988.

Finlayson-Pitts, B. J. and Jr, J. N. P.: Chemistry of the Upper and Lower Atmosphere: Theory, Experiments, and Applications, Elsevier, 993 pp., 1999.

Galloway, M. M., Huisman, A. J., Yee, L. D., Chan, A. W. H., Loza, C. L., Seinfeld, J. H., and Keutsch, F. N.: Yields of oxidized volatile organic compounds during the OH radical initiated oxidation of isoprene, methyl vinyl ketone, and methacrolein under high-NO_x conditions, Atmospheric Chem. Phys., 11, 10779–10790, https://doi.org/10.5194/acp-11-10779-2011, 2011.

Gkatzelis, G. I., Hohaus, T., Tillmann, R., Gensch, I., Müller, M., Eichler, P., Xu, K.-M., Schlag, P., Schmitt, S. H., Yu, Z., Wegener, R., Kaminski, M., Holzinger, R., Wisthaler, A., and Kiendler-Scharr, A.: Gas-to-particle partitioning of major biogenic oxidation products: a study on freshly formed and aged biogenic SOA, Atmospheric Chem. Phys., 18, 12969–12989, https://doi.org/10.5194/acp-18-12969-2018, 2018.

Gómez Alvarez, E., Viidanoja, J., Muñoz, A., Wirtz, K., and Hjorth, J.: Experimental Confirmation of the Dicarbonyl Route in the Photo-oxidation of Toluene and Benzene, Environ. Sci. Technol., 41, 8362–8369, https://doi.org/10.1021/es0713274, 2007.

Gómez Alvarez, E., Moreno, M. V., Gligorovski, S., Wortham, H., and Cases, M. V.: Characterisation and calibration of active sampling Solid Phase Microextraction applied to sensitive determination of gaseous carbonyls, Talanta, 88, 252–258, https://doi.org/10.1016/j.talanta.2011.10.039, 2012.

Grosjean, Daniel.: Wall loss of gaseous pollutants in outdoor Teflon chambers, Environ. Sci. Technol., 19, 1059–1065, https://doi.org/10.1021/es00141a006, 1985.

Henze, D. K., Seinfeld, J. H., Ng, N. L., Kroll, J. H., Fu, T.-M., Jacob, D. J., and Heald, C. L.: Global modeling of secondary organic aerosol formation from aromatic hydrocarbons: high- vs. low-yield pathways, Atmospheric Chem. Phys., 8, 2405–2420, https://doi.org/10.5194/acp-8-2405-2008, 2008.

Hu, D., Tolocka, M., Li, Q., and Kamens, R. M.: A kinetic mechanism for predicting secondary organic aerosol formation from toluene oxidation in the presence of NO_x and natural sunlight, Atmos. Environ., 41, 6478–6496, https://doi.org/10.1016/j.atmosenv.2007.04.025, 2007.

Huang, Y., Coggon, M. M., Zhao, R., Lignell, H., Bauer, M. U., Flagan, R. C., and Seinfeld, J. H.: The Caltech Photooxidation Flow Tube reactor: design, fluid dynamics and characterization, Atmospheric Meas. Tech., 10, 839–867, https://doi.org/10.5194/amt-10-839-2017, 2017.

IUPAC: Evaluated Kinetic Data, International Union of Pure and Applied Chemistry (IUPAC) Task Group on Atmospheric Chemical Kinetic Data Evaluation, https://iupac.aeris-data.fr/ (last access 05 February 2024), 2024.

Jang, M. and Kamens, R. M.: Newly characterized products and composition of secondary aerosols from the reaction of α-pinene with ozone, Atmos. Environ., 33, 459–474, https://doi.org/10.1016/S1352-2310(98)00222-2, 1999.

Jenkin, M. E., Saunders, S. M., Wagner, V., and Pilling, M. J.: Protocol for the development of the Master Chemical Mechanism, MCM v3 (Part B): tropospheric degradation of aromatic volatile organic compounds, Atmospheric Chem. Phys., 3, 181–193, https://doi.org/10.5194/acp-3-181-2003, 2003.

Jenkin, M. E., Glowacki, D. R., Rickard, A. R., and Pilling, M. J.: Comment on "Primary Atmospheric Oxidation Mechanism for Toluene," J. Phys. Chem. A, 113, 8136–8138, https://doi.org/10.1021/jp903119k, 2009.

Ji, Y., Zhao, J., Terazono, H., Misawa, K., Levitt, N. P., Li, Y., Lin, Y., Peng, J., Wang, Y., Duan, L., Pan, B., Zhang, F., Feng, X., An, T., Marrero-Ortiz, W., Secrest, J., Zhang, A. L., Shibuya, K., Molina, M. J., and Zhang, R.: Reassessing the atmospheric oxidation mechanism of toluene, Proc. Natl. Acad. Sci., 114, 8169–8174, https://doi.org/10.1073/pnas.1705463114, 2017.

Kanakidou, M., Seinfeld, J. H., Pandis, S. N., Barnes, I., Dentener, F. J., Facchini, M. C., Van Dingenen, R., Ervens, B., Nenes, A., Nielsen, C. J., Swietlicki, E., Putaud, J. P., Balkanski, Y., Fuzzi, S., Horth, J., Moortgat, G. K., Winterhalter, R., Myhre, C. E. L., Tsigaridis, K., Vignati, E., Stephanou, E. G., and Wilson, J.: Organic aerosol and global climate modelling: a review, Atmospheric Chem. Phys., 5, 1053–1123, https://doi.org/10.5194/acp-5-1053-2005, 2005.

Kiendler-Scharr, A., Becker, K.-H., Doussin, J.-F., Fuchs, H., Seakins, P., Wenger, J., and Wiesen, P.: Introduction to Atmospheric Simulation Chambers and Their Applications, in: A Practical Guide to Atmospheric Simulation Chambers, edited by: Doussin, J.-F., Fuchs, H., Kiendler-Scharr, A., Seakins, P., and Wenger, J., Springer International Publishing, Cham, 1–72, https://doi.org/10.1007/978-3-031-22277-1_1, 2023.

Klotz, B., Sørensen, S., Barnes, I., Becker, K. H., Etzkorn, T., Volkamer, R., Platt, U., Wirtz, K., and Martín-Reviejo, M.: Atmospheric Oxidation of Toluene in a Large-Volume Outdoor Photoreactor: In Situ Determination of Ring-Retaining Product Yields, J. Phys. Chem. A, 102, 10289–10299, https://doi.org/10.1021/jp982719n, 1998.

Koss, A. R., Sekimoto, K., Gilman, J. B., Selimovic, V., Coggon, M. M., Zarzana, K. J., Yuan, B., Lerner, B. M., Brown, S. S., Jimenez, J. L., Krechmer, J., Roberts, J. M., Warneke, C., Yokelson, R. J., and de Gouw, J.: Non-methane organic gas emissions from biomass burning: identification, quantification, and emission factors from PTR-ToF during the FIREX 2016 laboratory experiment, Atmospheric Chem. Phys., 18, 3299–3319, https://doi.org/10.5194/acp-18-3299-2018, 2018.

Koziel, J. A. and Pawliszyn, J.: Air sampling and analysis of volatile organic compounds with solid phase microextraction, J. Air Waste Manag. Assoc. 1995, 51, 173–184, https://doi.org/10.1080/10473289.2001.10464263, 2001.

Krechmer, J. E., Day, D. A., and Jimenez, J. L.: Always Lost but Never Forgotten: Gas-Phase Wall Losses Are Important in All Teflon Environmental Chambers, Environ. Sci. Technol., 54, 12890–12897, https://doi.org/10.1021/acs.est.0c03381, 2020.

Lelieveld, J., Butler, T. M., Crowley, J. N., Dillon, T. J., Fischer, H., Ganzeveld, L., Harder, H., Lawrence, M. G., Martinez, M., Taraborrelli, D., and Williams, J.: Atmospheric oxidation capacity sustained by a tropical forest, Nature, 452, 737–740, https://doi.org/10.1038/nature06870, 2008.

Leskinen, A., Yli-Pirilä, P., Kuuspalo, K., Sippula, O., Jalava, P., Hirvonen, M.-R., Jokiniemi, J., Virtanen, A., Komppula, M., and Lehtinen, K. E. J.: Characterization and testing of a new environmental chamber, Atmospheric Meas. Tech., 8, 2267–2278, https://doi.org/10.5194/amt-8-2267-2015, 2015.

Lindinger, W., Hansel, A., and Jordan, A.: On-line monitoring of volatile organic compounds at pptv levels by means of proton-transfer-reaction mass spectrometry (PTR-MS) medical applications, food control and environmental research, Int. J. Mass Spectrom. Ion Process., 173, 191–241, https://doi.org/10.1016/S0168-1176(97)00281-4, 1998.

Liu, X., Jeffries, H. E., and Sexton, K. G.: Atmospheric Photochemical Degradation of 1,4-Unsaturated Dicarbonyls, Environ. Sci. Technol., 33, 4212–4220, https://doi.org/10.1021/es990469y, 1999.

Lumiaro, E., Todorović, M., Kurten, T., Vehkamäki, H., and Rinke, P.: Predicting gas–particle partitioning coefficients of atmospheric molecules with machine learning, Atmospheric Chem. Phys., 21, 13227–13246, https://doi.org/10.5194/acp-21-13227-2021, 2021.

Ma, W., Liu, Y., Zhang, Y., Feng, Z., Zhan, J., Hua, C., Ma, L., Guo, Y., Zhang, Y., Zhou, W., Yan, C., Chu, B., Chen, T., Ma, Q., Liu, C., Kulmala, M., Mu, Y., and He, H.: A New Type of Quartz Smog Chamber: Design and Characterization, Environ. Sci. Technol., 56, 2181–2190, https://doi.org/10.1021/acs.est.1c06341, 2022.

Majer, J. R., Naman, S.-A. M. A., and Robb, J. C.: Photolysis of aromatic aldehydes, Trans. Faraday Soc., 65, 1846–1853, https://doi.org/10.1039/TF9696501846, 1969.

Martos, P. A. and Pawliszyn, J.: Calibration of Solid Phase Microextraction for Air Analyses Based on Physical Chemical Properties of the Coating, Anal. Chem., 69, 206–215, https://doi.org/10.1021/ac960415w, 1997.

Martos, P. A. and Pawliszyn, J.: Sampling and Determination of Formaldehyde Using Solid-Phase Microextraction with On-Fiber Derivatization, Anal. Chem., 70, 2311–2320, https://doi.org/10.1021/ac9711394, 1998.

Matsunaga, A. and Ziemann, P. J.: Gas-Wall Partitioning of Organic Compounds in a Teflon Film Chamber and Potential Effects on Reaction Product and Aerosol Yield Measurements, Aerosol Sci. Technol., 44, 881–892, https://doi.org/10.1080/02786826.2010.501044, 2010.

McMurry, P. H. and Grosjean, Daniel.: Gas and aerosol wall losses in Teflon film smog chambers, Environ. Sci. Technol., 19, 1176–1182, https://doi.org/10.1021/es00142a006, 1985.

Michoud, V., Sauvage, S., Léonardis, T., Fronval, I., Kukui, A., Locoge, N., and Dusanter, S.: Field measurements of methylglyoxal using proton transfer reaction time-of-flight mass spectrometry and comparison to the DNPH–HPLC–UV method, Atmospheric Meas. Tech., 11, 5729–5740, https://doi.org/10.5194/amt-11-5729-2018, 2018.

Moschonas, N., Danalatos, D., and Glavas, S.: The effect of O_2 and NO_2 on the ring retaining products of the reaction of toluene with hydroxyl radicals, Atmos. Environ., 33, 111–116, https://doi.org/10.1016/S1352-2310(98)00134-4, 1998.

Müller, M., Graus, M., Wisthaler, A., Hansel, A., Metzger, A., Dommen, J., and Baltensperger, U.: Analysis of high mass resolution PTR-TOF mass spectra from 1,3,5-trimethylbenzene (TMB) environmental chamber experiments, Atmospheric Chem. Phys., 12, 829–843, https://doi.org/10.5194/acpd-11-25871-2011, 2012.

Munday, E. B., Mullins, J. C., and Edie, D. D.: Vapor pressure data for toluene, 1-pentanol, 1-butanol, water, and 1-propanol and for the water and 1-propanol system from 273.15 to 323.15 K, J. Chem. Eng. Data, 25, 191–194, https://doi.org/10.1021/je60086a006, 1980.

Muñoz, A., Borrás, E., Ródenas, M., Vera, T., and Pedersen, H. A.: Atmospheric Oxidation of a Thiocarbamate Herbicide Used in Winter Cereals, Environ. Sci. Technol., 52, 9136–9144, https://doi.org/10.1021/acs.est.8b02157, 2018.

NCAR: Tropospheric Ultraviolet and Visible (TUV) Radiation Model, v5.3, National Center for Atmospheric Research (NCAR), web version of model, https://www.acom.ucar.edu/Models/TUV/Interactive_TUV/ (last access 05 February 2024), 2024.

Newland, M. J., Jenkin, M. E., and Rickard, A. R.: Elucidating the fate of the OH-adduct in toluene oxidation under tropospheric boundary layer conditions, Proc. Natl. Acad. Sci., 114, E7856–E7857, https://doi.org/10.1073/pnas.1713678114, 2017.

Newland, M. J., Rea, G. J., Thüner, L. P., Henderson, A. P., Golding, B. T., Rickard, A. R., Barnes, I., and Wenger, J.: Photochemistry of 2-butenedial and 4-oxo-2-pentenal under atmospheric boundary layer conditions, Phys. Chem. Chem. Phys., 21, 1160–1171, https://doi.org/10.1039/C8CP06437G, 2019.

Olariu, R. I., Klotz, B., Barnes, I., Becker, K. H., and Mocanu, R.: FT–IR study of the ring-retaining products from the reaction of OH radicals with phenol, o-, m-, and p-cresol, Atmos. Environ., 36, 3685–3697, https://doi.org/10.1016/S1352-2310(02)00202-9, 2002.

Pindado Jiménez, O., Pérez Pastor, R. M., Vivanco, M. G., and Santiago Aladro, M.: A chromatographic method to analyze products from photo-oxidation of anthropogenic and biogenic mixtures of volatile organic compounds in smog chambers, Talanta, 106, 20–28, https://doi.org/10.1016/j.talanta.2012.11.081, 2013.

Rissanen, M.: Anthropogenic Volatile Organic Compound (AVOC) Autoxidation as a Source of Highly Oxygenated Organic Molecules (HOM), J. Phys. Chem. A, 125, 9027–9039, https://doi.org/10.1021/acs.jpca.1c06465, 2021.

Rivera-Rios, J. C., Nguyen, T. B., Crounse, J. D., Jud, W., St. Clair, J. M., Mikoviny, T., Gilman, J. B., Lerner, B. M., Kaiser, J. B., de Gouw, J., Wisthaler, A., Hansel, A., Wennberg, P. O., Seinfeld, J. H., and Keutsch, F. N.: Conversion of hydroperoxides to carbonyls in field and laboratory instrumentation: Observational bias in diagnosing pristine versus anthropogenically controlled atmospheric chemistry, Geophys. Res. Lett., 41, 8645–8651, https://doi.org/10.1002/2014GL061919, 2014.

Rohrer, F., Bohn, B., Brauers, T., Brüning, D., Johnen, F.-J., Wahner, A., and Kleffmann, J.: Characterisation of the photolytic HONO-source in the atmosphere simulation chamber SAPHIR, Atmospheric Chem. Phys., 5, 2189–2201, https://doi.org/10.5194/acp-5-2189-2005, 2005.

Romano, A. and Hanna, G. B.: Identification and quantification of VOCs by proton transfer reaction time of flight mass spectrometry: An experimental workflow for the optimization of specificity, sensitivity, and accuracy, J. Mass Spectrom., 53, 287–295, https://doi.org/10.1002/jms.4063, 2018.

Salazar Gómez, J. I., Sojka, M., Klucken, C., Schlögl, R., and Ruland, H.: Determination of trace compounds and artifacts in nitrogen background measurements by proton transfer reaction time-of-flight mass spectrometry under dry and humid conditions, J. Mass Spectrom., 56, e4777, https://doi.org/10.1002/jms.4777, 2021.

Saunders, S. M., Jenkin, M. E., Derwent, R. G., and Pilling, M. J.: Protocol for the development of the Master Chemical Mechanism, MCM v3 (Part A): tropospheric degradation of non-aromatic volatile organic compounds, Atmospheric Chem. Phys., 3, 161–180, https://doi.org/10.5194/acp-3-161-2003, 2003.

Schmarr, H.-G., Sang, W., Ganss, S., Fischer, U., Köpp, B., Schulz, C., and Potouridis, T.: Analysis of aldehydes via headspace SPME with on-fiber derivatization to their O-(2,3,4,5,6-pentafluorobenzyl)oxime derivatives and comprehensive 2D-GC-MS, J. Sep. Sci., 31, 3458–3465, https://doi.org/10.1002/jssc.200800294, 2008.

von Schneidemesser, E., Monks, P. S., Allan, J. D., Bruhwiler, L., Forster, P., Fowler, D., Lauer, A., Morgan, W. T., Paasonen, P., Righi, M., Sindelarova, K., and Sutton, M. A.: Chemistry and the Linkages between Air Quality and Climate Change, Chem. Rev., 115, 3856–3897, https://doi.org/10.1021/acs.chemrev.5b00089, 2015.

Schwantes, R. H., Schilling, K. A., McVay, R. C., Lignell, H., Coggon, M. M., Zhang, X., Wennberg, P. O., and Seinfeld, J. H.: Formation of highly oxygenated low-volatility products from cresol oxidation, Atmospheric Chem. Phys., 17, 3453–3474, https://doi.org/10.5194/acp-17-3453-2017, 2017.

Seuwen, R. and Warneck, P.: Oxidation of toluene in NO_x free air: Product distribution and mechanism, Int. J. Chem. Kinet., 28, 315–332, https://doi.org/10.1002/(SICI)1097-4601(1996)28:5<315::AID-KIN1>3.0.CO;2-Y, 1996.

Shaw, J. T., Lidster, R. T., Cryer, D. R., Ramirez, N., Whiting, F. C., Boustead, G. A., Whalley, L. K., Ingham, T., Rickard, A. R., Dunmore, R. E., Heard, D. E., Lewis, A. C., Carpenter, L. J., Hamilton, J. F., and Dillon, T. J.: A self-consistent, multivariate method for the determination of gas-phase rate coefficients, applied to reactions of atmospheric VOCs and the hydroxyl radical, Atmospheric Chem. Phys., 18, 4039–4054, https://doi.org/10.5194/acp-18-4039-2018, 2018.

Siekmann, F.: Freisetzung von photolabilen und reaktiven Halogenverbindungen aus salzhaltigen Aerosolen unter simulierten troposphärischen Reinluftbedingungen in einer Aerosol-Smogkammer, Doctoral thesis, University of Bayreuth, Bayreuth, 139 pp., 2018.

Smith, D. F., McIver, C. D., and Kleindienst, T. E.: Primary Product Distribution from the Reaction of Hydroxyl Radicals with Toluene at ppb NO_x Mixing Ratios, J. Atmospheric Chem., 30, 209–228, https://doi.org/10.1023/A:1005980301720, 1998.

Stönner, C., Derstroff, B., Klüpfel, T., Crowley, J. N., and Williams, J.: Glyoxal measurement with a proton transfer reaction time of flight mass spectrometer (PTR-TOF-MS): characterization and calibration, J. Mass Spectrom., 52, 30–35, https://doi.org/10.1002/jms.3893, 2017.

Tumbiolo, S., Gal, J.-F., Maria, P.-C., and Zerbinati, O.: Determination of benzene, toluene, ethylbenzene and xylenes in air by solid phase micro-extraction/gas chromatography/mass spectrometry, Anal. Bioanal. Chem., 380, 824–830, https://doi.org/10.1007/s00216-004-2837-1, 2004.

Vaghjiani, G. L. and Ravishankara, A. R.: Photodissociation of H_2O_2 and CH_3OOH at 248 nm and 298 K: Quantum yields for OH, $O(^3P)$ and $H(^2S)$, J. Chem. Phys., 92, 996–1003, https://doi.org/10.1063/1.458081, 1990.

Vasquez, K. T., Allen, H. M., Crounse, J. D., Praske, E., Xu, L., Noelscher, A. C., and Wennberg, P. O.: Low-pressure gas chromatography with chemical ionization mass spectrometry for quantification of multifunctional organic compounds in the atmosphere, Atmospheric Meas. Tech., 11, 6815–6832, https://doi.org/10.5194/amt-11-6815-2018, 2018.

Volkamer, R., Platt, U., and Wirtz, K.: Primary and Secondary Glyoxal Formation from Aromatics: Experimental Evidence for the Bicycloalkyl−Radical Pathway from Benzene, Toluene, and p-Xylene, J. Phys. Chem. A, 105, 7865–7874, https://doi.org/10.1021/jp010152w, 2001.

Wagner, V., Jenkin, M. E., Saunders, S. M., Stanton, J., Wirtz, K., and Pilling, M. J.: Modelling of the photooxidation of toluene: conceptual ideas for validating detailed mechanisms, Atmospheric Chem. Phys., 3, 89–106, https://doi.org/10.5194/acp-3-89-2003, 2003.

White, S. J., Jamie, I. M., and Angove, D. E.: Chemical characterisation of semi-volatile and aerosol compounds from the photooxidation of toluene and NO_x, Atmos. Environ., 83, 237–244, https://doi.org/10.1016/j.atmosenv.2013.11.023, 2014.

Williams, J., Keßel, S. U., Nölscher, A. C., Yang, Y., Lee, Y., Yáñez-Serrano, A. M., Wolff, S., Kesselmeier, J., Klüpfel, T., Lelieveld, J., and Shao, M.: Opposite OH reactivity and ozone cycles in the Amazon rainforest and megacity Beijing: Subversion of biospheric oxidant control by anthropogenic emissions, Atmos. Environ., 125, 112–118, https://doi.org/10.1016/j.atmosenv.2015.11.007, 2016.

Wittmer, J., Bleicher, S., and Zetzsch, C.: Iron(III)-Induced Activation of Chloride and Bromide from Modeled Salt Pans, J. Phys. Chem. A, 119, 4373–4385, https://doi.org/10.1021/jp508006s, 2015.

Wróblewski, T., Ziemczonek, L., Alhasan, A. M., and Karwasz, G. P.: Ab initio and density functional theory calculations of proton affinities for volatile organic compounds, Eur. Phys. J. Spec. Top., 144, 191–195, https://doi.org/10.1140/epjst/e2007-00126-7, 2007.

Wu, R., Pan, S., Li, Y., and Wang, L.: Atmospheric Oxidation Mechanism of Toluene, J. Phys. Chem. A, 118, 4533–4547, https://doi.org/10.1021/jp500077f, 2014.

Ye, P., Ding, X., Hakala, J., Hofbauer, V., Robinson, E. S., and Donahue, N. M.: Vapor wall loss of semi-volatile organic compounds in a Teflon chamber, Aerosol Sci. Technol., 50, 822–834, https://doi.org/10.1080/02786826.2016.1195905, 2016.

Yeh, G. K. and Ziemann, P. J.: Gas-Wall Partitioning of Oxygenated Organic Compounds: Measurements, Structure–Activity Relationships, and Correlation with Gas Chromatographic Retention Factor, Aerosol Sci. Technol., 49, 727–738, https://doi.org/10.1080/02786826.2015.1068427, 2015.

Yeoman, A. M., Shaw, M., and Lewis, A. C.: Estimating person-to-person variability in VOC emissions from personal care products used during showering, Indoor Air, 31, 1281–1291, https://doi.org/10.1111/ina.12811, 2021.

Yu, J., Flagan, R. C., and Seinfeld, J. H.: Identification of Products Containing −COOH, −OH, and −CO in Atmospheric Oxidation of Hydrocarbons, Environ. Sci. Technol., 32, 2357–2370, https://doi.org/10.1021/es980129x, 1998.

Zádor, J., Turányi, T., Wirtz, K., and Pilling, M. J.: Measurement and investigation of chamber radical sources in the European Photoreactor (EUPHORE), J. Atmospheric Chem., 55, 147–166, https://doi.org/10.1007/s10874-006-9033-y, 2006.

Zaytsev, A., Koss, A. R., Breitenlechner, M., Krechmer, J. E., Nihill, K. J., Lim, C. Y., Rowe, J. C., Cox, J. L., Moss, J., Roscioli, J. R., Canagaratna, M. R., Worsnop, D. R., Kroll, J. H., and Keutsch, F. N.: Mechanistic study of the formation of ring-retaining and ring-opening products from the oxidation of aromatic compounds under urban atmospheric conditions, Atmospheric Chem. Phys., 19, 15117–15129, https://doi.org/10.5194/acp-19-15117-2019, 2019.

Zhang, R. M., Truhlar, D. G., and Xu, X.: Kinetics of the Toluene Reaction with OH Radical, Research, 2019, https://doi.org/10.34133/2019/5373785, 2019.

Zhang, X., Schwantes, R. H., McVay, R. C., Lignell, H., Coggon, M. M., Flagan, R. C., and Seinfeld, J. H.: Vapor wall deposition in Teflon chambers, Atmospheric Chem. Phys., 15, 4197–4214, https://doi.org/10.5194/acp-15-4197-2015, 2015.

Zhao, Y., Li, Y., Kumar, A., Ying, Q., Vandenberghe, F., and Kleeman, M. J.: Separately resolving NO_x and VOC contributions to ozone formation, Atmos. Environ., 285, 119224, https://doi.org/10.1016/j.atmosenv.2022.119224, 2022.

Supplementary Information.

Characterization of the new BATCH Teflon chamber and on-line analysis of isomeric multifunctional photooxidation products

Finja Löher[1,2], Esther Borrás[3], Amalia Muñoz[3], Anke Christine Nölscher[1,2]

[1]Department of Atmospheric Chemistry, University of Bayreuth, 95447 Bayreuth, Germany
[2]Bayreuth Center of Ecology and Environmental Research (BayCEER), University of Bayreuth, 95447 Bayreuth, Germany
[3]Fundación Centro de Estudios Ambientales del Mediterráneo (CEAM), 46980 Paterna, Valencia, Spain

Correspondence to: Finja Löher (finja.loeher@uni-bayreuth.de) and Anke C. Nölscher (anke.noelscher@uni-bayreuth.de)

Hereinafter, the following abbreviations are used for toluene photooxidation products and their internal standards (here sorted according to their retention time, as in Table 1 in the main text): phenol-d_6 (PHE-d_6), *o*-cresol (OCR), *m*-cresol (MCR), *p*-cresol (PCR), benzyl alcohol (BOH), *o*-nitrotoluene (ONT), (nitromethyl)benzene (NMB), *m*-nitrotoluene (MNT), benzoic acid (BAC), *p*-methylcatechol (PMC), glycolaldehyde (GAL), nitrocresols (NCR), pyruvic acid (PAC), acetophenone-d_8 (APH-d_8), benzaldehyde (BAL), glyoxal (GLY), methylglyoxal (MGL), *p*-hydroxybenzaldehyde (PHB).

S1 Emission Spectrum of Solar Simulator

S1.1 Photolysis Rates

We calculated the compound-specific photolysis rates theoretically in order to overcome the restriction to compounds with available authentic standards, and to exclude mutual formation and solvent effects associated with the empirical evaluation of a large range of in parts solid photooxidation products. The compound-specific absorption cross sections and quantum yields and the resulting photolysis rates are listed in Table S1. The calculation of the photolysis rate from the emission spectrum and the absorption cross section is illustrated exemplary for H_2O_2 in Fig. S1 (quantum yield = 1).

Table S1: Calculated photolysis rates of the measured photooxidation products and other relevant compounds in the BATCH Teflon chamber. Unless stated otherwise, values apply to T = 298 K. The wavelength ranges for which the photolysis rates were calculated were restricted by the available absorption cross section data, and the recorded emission spectrum of the solar simulator ($\lambda > 262$ nm). If no absorption cross section was available, the photolysis rate was set to zero. If no quantum yield was available, it was set to 1. Whenever available, IUPAC-recommended values were selected. The uncertainty of the photolysis rates is 38 %.

Compound	Absorption cross section / nm range	Quantum yield / molecules photons^{-1}	Photolysis rate / s^{-1}	Note
OCR	250 – 291 (Etzkorn et al., 1999)	1	$7.42\pm2.82\times10^{-6}$	
MCR	250 – 291 (Etzkorn et al., 1999)	1	$7.40\pm2.81\times10^{-6}$	
PCR	250 – 291 (Etzkorn et al., 1999)	1	$1.17\pm0.44\times10^{-5}$	
BOH	220 – 280 (El Dib et al., 2006)	1	$4.60\pm1.75\times10^{-8}$	
ONT	171 – 300 (Shama, 1991)	0.004 (Sandus and Slagg, 1972)	$3.01\pm1.14\times10^{-7}$	
NMB	n.a.	n.a.	n.a.	set to zero
MNT	171 – 301 (Shama, 1991)	0.0008 (Sandus and Slagg, 1972)	$1.77\pm0.67\times10^{-8}$	
BAC	220 – 280 (Roth et al., 2010)	1	$1.33\pm0.51\times10^{-6}$	T = 293 − 357 K
PMC	n.a.	n.a.	n.a.	set to zero
GAL	205 – 335 (Bacher et al., 2001)[(a)]	0.75 (Bacher et al., 2001)[(a)]	$1.01\pm0.38\times10^{-5}$	
NCR	320 – 450 (Chen et al., 2011)[(a)]	0.0001 (Bejan et al., 2006)	$1.93\pm0.73\times10^{-5}$	2-nitro-*p*-cresol, T = 293 K
PAC	251 – 407 (Horowitz et al., 2001)[(a)]	0.24 (Reed Harris et al., 2016)	$1.49\pm0.57\times10^{-4}$	
BAL	220 – 395 (IUPAC, 2024)[(a)]	0.29 (Zhu and Cronin, 2000)[(a)]	$2.52\pm0.96\times10^{-4}$	
GLY	250 – 473 (Volkamer et al., 2005)[(a)]	$\phi(\lambda)$ (IUPAC, 2024)[(a)]	$2.57\pm0.98\times10^{-4}$	T = 296 K
MGL	219 – 493 (Meller et al., 1991)[(a)]	$\phi(\lambda)$ (IUPAC, 2024)[(a)]	$3.02\pm1.15\times10^{-4}$	T = 296 K
PHB	n.a.	n.a.	n.a.	set to zero
H_2O_2	190 – 350 (IUPAC, 2024)[(a)] 353 – 410 (Kahan et al., 2012)	1 (IUPAC, 2024)[(a)]	$1.13\pm0.43\times10^{-5}$	T = 296.0 − 297.4 K
Toluene	115 – 315 (Serralheiro et al., 2015)	1	$3.78\pm1.44\times10^{-7}$	
NO_2	205 – 495 (IUPAC, 2024)[(a)]	$\phi(\lambda)$ (Troe, 2000)[(a)]	$2.07\pm0.79\times10^{-2}$	
NO_3	400 – 690 (IUPAC, 2024)[(a)]	$\phi(\lambda)$ (Johnston et al., 1996)[(a)]	$3.07\pm1.17\times10^{-1}$	

[(a)] *IUPAC recommendation.*

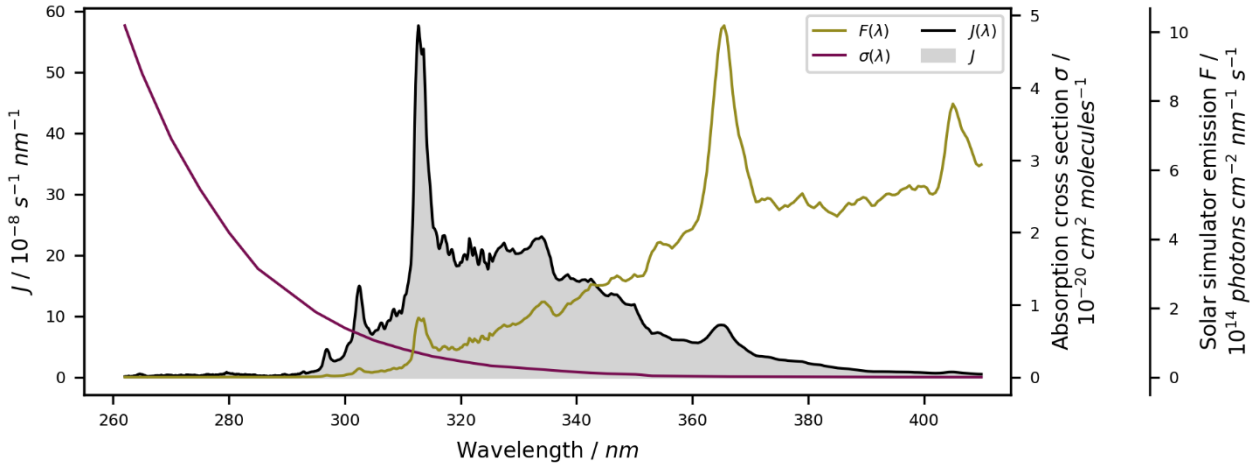

Figure S1: Photolysis of H_2O_2 as a source of OH radicals in the BATCH Teflon chamber. The emission F of the solar simulator, absorption cross section σ of H_2O_2, and resulting photolysis rate J as functions of wavelength are shown. The overall photolysis rate is derived from the integration of the wavelength-specific photolysis rate. The quantum yield of the H_2O_2 photolysis equals unity over the entire wavelength range and is therefore not illustrated specifically.

S1.2 Actinometry

We performed actinometric experiments with NO_2 and methylglyoxal to confirm the emission spectrum that we recorded for the solar simulator.

For the NO_2 chemistry, reactions (R1), (R2), and (R3) need to be considered:

$$NO_2 \xrightarrow{h\nu} NO + O(^3P) \quad \text{(R1)}$$

$$O(^3P) + O_2 \xrightarrow{M} O_3 \quad \text{(R2)}$$

$$NO + O_3 \rightarrow NO_2 + O_2 \quad \text{(R3)}$$

We worked in hydrocarbon-free air to avoid the competitive oxidation of NO by peroxy radicals. During photochemical equilibrium of NO_2, NO, and O_3, the photolysis rate of NO_2 ($J(NO_2)$, s^{-1}) can then be calculated using Eq. (S1):

$$J(NO_2) = \frac{k_{NO+O_3}[NO][O_3]}{[NO_2]} \quad \text{(S1)}$$

where k_{NO+O_3} = 1.90±0.31×10^{-14} molecules^{-1} cm^3 s^{-1} is the rate constant of the reaction of NO and O_3 at T = 298 K (IUPAC, 2024), and $[NO]$, $[O_3]$, and $[NO_2]$ are the concentrations of NO, O_3, and NO_2 in photostationary state in molecules cm^{-3}. Temporal profiles of NO, NO_2, and O_3 in photochemical equilibrium are provided in Fig. S2. The mean values within this time frame were [NO] = 9.38±1.31×10^{11} molecules cm^{-3}, [NO_2] = 1.70±1.41×10^{11} molecules cm^{-3}, and [O_3] = 2.20±0.04×10^{11} molecules cm^{-3}. The error in the resulting NO_2 photolysis rate was calculated from the propagation of the relative errors of the rate constant k, and the concentrations [NO], [NO_2], and [O_3]. It was affected mainly by the high uncertainty in the NO_2 quantification. We derived a value of J = 2.32±1.99×10^{-2} s^{-1} for the NO_2 photolysis rate.

For methylglyoxal, we fitted the wall-loss-corrected decay in the irradiated chamber (Fig. S3). The error in the resulting photolysis rate was calculated from the propagation of the NRMSE of the exponential regression (0.06) and the uncertainty of the assumed wall loss rate (0.14). We derived a value of J = 3.66±0.56×10^{-4} s^{-1} for the methylglyoxal photolysis rate.

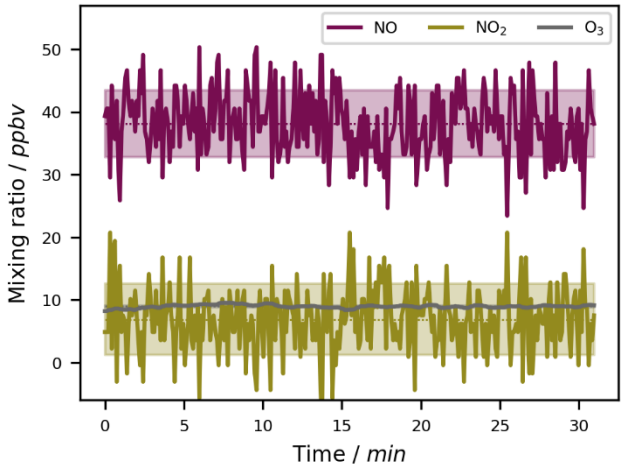

Figure S2: Temporal profiles of NO, NO_2, and O_3 in photostationary state in the BATCH Teflon chamber. The mean values within this time frame were used for the calculation of the NO_2 photolysis rate.

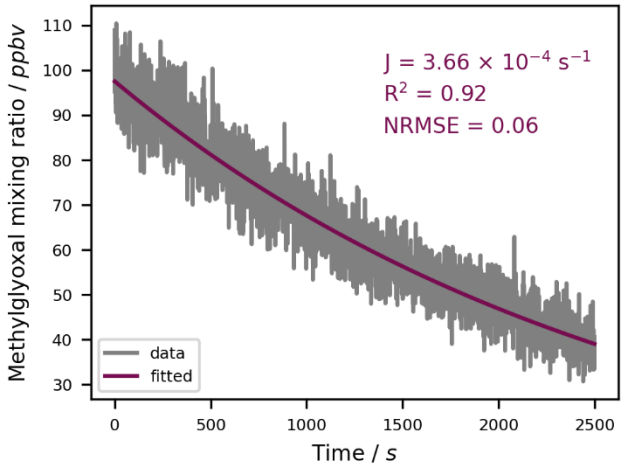

Figure S3: Empirical determination of the methylglyoxal photolysis rate in the BATCH Teflon chamber. The data were obtained on a second resolution over a time frame of roughly 40 minutes. Prior to fitting, the data were corrected for the determined wall loss rate.

S2 Materials

S2.1 Chemicals

The derivatization reagents PFBHA and MSTFA and the catalyst TMCS, as well as the internal standards phenol-d_6 and acetophenone-d_8 were supplied by Sigma Aldrich / Merck (Darmstadt, Germany). Acetonitrile (Roth, Karlsruhe, Germany) and ultrapure water (0.055 µS cm^{-1}) were used as solvents.

The following oxidation products were purchased as authentic standards: *o*-cresol, *m*-cresol, *p*-cresol, benzyl alcohol, *o*-nitrotoluene, *m*-nitrotoluene, *p*-nitrotoluene, (nitromethyl)benzene, benzoic acid, *p*-methylcatechol, glycolaldehyde, 6-nitro-*m*-cresol, benzaldehyde, 40% glyoxal (aq), 40% methylglyoxal (aq), *p*-hydroxybenzaldehyde, acetaldehyde, acetic acid, acetone, formaldehyde, glyoxylic acid, oxalic acid, succinic acid, *p*-toluquinone (Sigma Aldrich / Merck, Darmstadt, Germany), 2-nitro-*p*-cresol, 4-nitro-*m*-cresol, dimethylglyoxal (Thermo Fisher Scientific, Schwerte, Germany), glutaric acid, pyruvic acid (Alfa Aesar, Karlsruhe, Germany), formic acid (Honeywell Fluka, Offenbach, Germany), and methanol (Roth, Karlsruhe, Germany).

S2.2 NO_x and O_3 Analysers

A NO_x analyser based on chemiluminescence detection (Teledyne, T200P) was used to monitor NO and NO_2. The T200P model is equipped with a high efficiency photolytic converter for NO_2 detection. For the NO_2 actinometric experiments, we used a CLD 700 AL (ECO PHYSICS). To observe the formation of O_3, a UV photometric O_3 analyser (Thermo Scientific, 49i) was available. All instruments were calibrated using a dilution calibrator and gas-phase titration (Teledyne, T750U). From the performed calibrations, we derived average noises in the signals of 5.34 ppbv (CLD measurement) and 0.16 ppbv (Blue Light Converter measurement) for NO, 5.73 ppbv (CLD measurement) and 0.12 ppbv (Blue Light Converter measurement) for NO_2, and 0.18 ppbv for O_3.

S3 SPME-GC-MS Analysis

S3.1 Instrumental Settings

Table S2: GC and MS parameters. Used in this configuration for all tests and experiments conducted in this study.

Step	Parameter
GC inlet	Temperature: 250 °C
	Liner: RESTEK, Topaz, single taper with wool, 23303
	Injection: splitless
GC column	Type: Agilent, HP-5MS, 30 m×0.25 mm×0.25 µm, 19091S-433
	Carrier gas: Helium
	Constant flow: 1.5 sccm
GC oven	Initial temperature: 45 °C, hold 0.1 min
	Ramp 1: 20 °C min^{-1} to 80 °C, hold 2 min
	Ramp 2: 12 °C min^{-1} to 240 °C
	Ramp 3: 100 °C min^{-1} to 280 °C, hold 3 min
MS settings	Transfer line temperature: 280 °C
	Source temperature: 230 °C
	Quadrupole temperature: 150 °C
	Ionization: EI, 70 eV
	Scan mode: m/z 40 – m/z 550, threshold 10, 1562 u s^{-1}
	SIM mode[(a)]: 3 time segments, dwell times 800 – 900 ms

[(a)] See Table 1 in main text.

Table S3: List of steps in each SPME-GC-MS sampling cycle in chronological order. The double derivatization scheme with the optimized reagent preparation and extraction parameters was adapted from Borrás et al. (2021).

SPME fibre	Instrument
	PFBHA headspace generation (Agitator: 50 °C, 500 rpm, 3 min)
PFBHA extraction (4 min)	
Sample extraction (5 min, 5 SLPM)	MSTFA/TMCS headspace generation (Agitator: 50 °C, 500 rpm, 3 min)
MSTFA/TMCS extraction (3 min)	
Desorption into GC inlet (250 °C, 40 mm depth, 10 min)	GC-MS run (20.5 min)
Fibre conditioning in N_2 (240 °C, 10 min)	

S3.2 Sampling Cell

The sampling cell consisted of a 126×28×25 mm PTFE block which was held in place by a polyvinylchloride (PVC) body that fitted tightly in the SPME-GC-MS sample tray. A circular hole (9 mm diameter) was drilled through the entire length of the PTFE block to guide the flow of air. The material and the enforced flow profile were designed to reduce species conversions and wall losses. Another hole was drilled from the top so that it connected with the main tunnel. It was sealed with a septum (Supelco, PTFE/silicone, 1.5 mm thickness, 27511) and used as needle guide for the SPME system. During on-line analysis, the fibre coating was placed directly in the sample flow path (penetration depth of 47.5 mm) for maximum extraction efficiency. A technical drawing of the sampling cell is shown in Fig. S4.

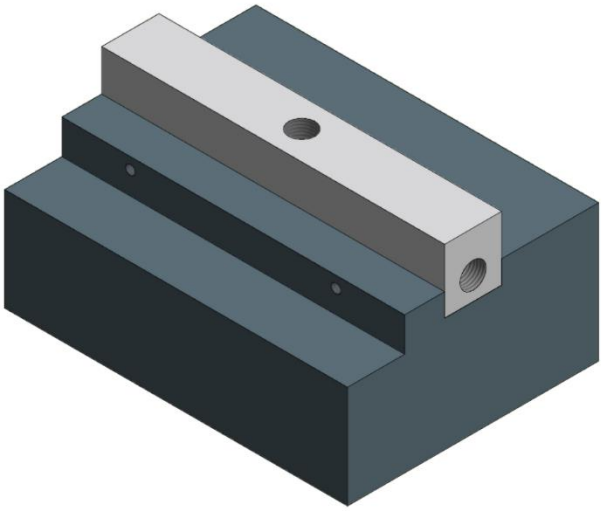

Figure S4: Technical drawing of the sampling cell as illustrated and used for construction by the workshop of the University of Bayreuth. The dark grey area is the PVC body, while the light grey area is the PTFE flow guide. The PTFE part has ¼'' NPT fittings on each side as well as on the top, the latter of which is used to guide the SPME needle into the flow of sample air.

S3.3 Internal Standards

The addition of the ISTDs into the transfer line flow towards the SPME-GC-MS sampling cell was facilitated by means of a customized permeation source (Fig. S5). Permeation sources, in which the pure analyte is slowly released through a permeable layer, are known to supply low concentrations of gases in a constant manner over time if the temperature and flows are carefully controlled (Mitchell, 2000; Namies´nik, 1984; Thorenz et al., 2012). Here, a separate permeation tube was constructed for each ISTD by placing the pure substance in a 2 mL glass vial with open screw cap. For the more volatile acetophenone-d_8, a virginal PTFE septum (thickness: 0.5 mm) was inserted directly in the screw cap (opening 6 mm in diameter). For phenol-d_6, a much larger permeable area was created by placing a 6.5 cm long PTFE tube (outer diameter = 6 mm, inner diameter: 4 mm) tightly through the screw cap and sealing the upper end with a solid PTFE stopper. Both permeation tubes were placed in a 250 mL glass impinger which was continuously flushed with 200 sccm N_2. The outflow was directed either into the main transfer line (for analysis) or into the fume hood (inactive periods). For controlling the temperature, the impinger was wrapped with electric heating wire, insulated rigorously, and placed in a dewar. The voltage of the heating wire was adjusted to achieve a response of the ISTDs similar to the response of the analytes, resulting in about 40 °C in the impinger.

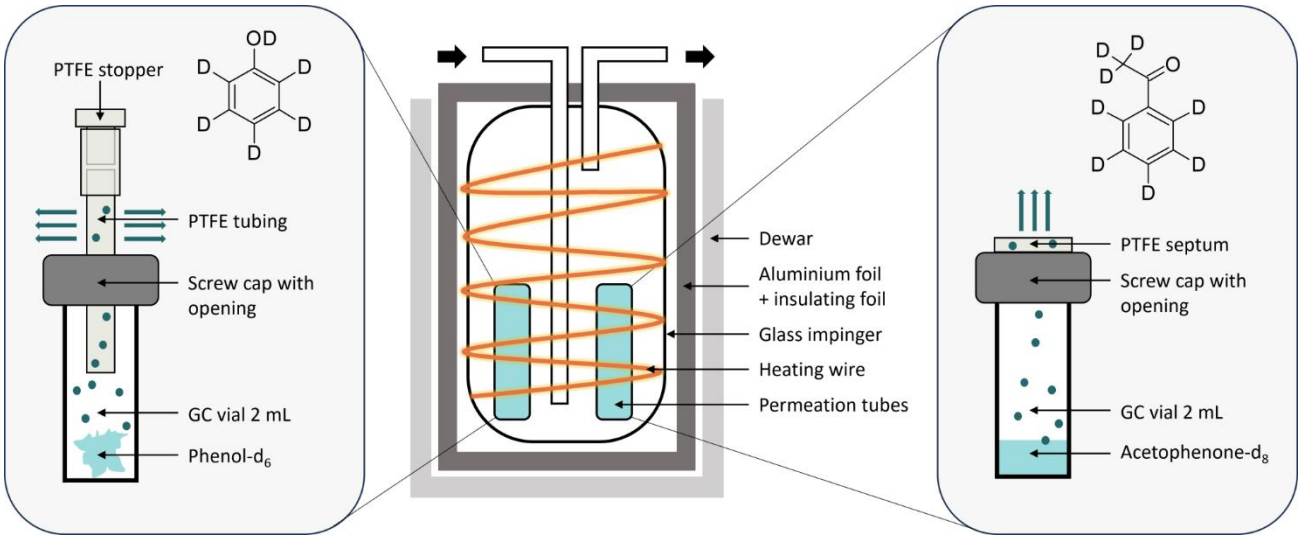

Figure S5: Permeation system for on-line internal standard addition. Customized permeation tubes were designed for phenol-d_6 and acetophenone-d_8. Phenol-d_6 permeated through a PTFE tube (wall thickness 1 mm, 6.5 cm long), while acetophenone-d_8 permeated through a PTFE septum in the open screw cap (thickness 0.5 mm, 6 mm diameter). Both permeation tubes were kept at a constant temperature in an insulated impinger (T = 40 °C) and added with a constant flow of N_2 (200 sccm). Dimensions are not to scale.

S3.4 Derivatization

The silylation of alcohols and carboxylic acids with MSTFA and the typical fragments in the EI spectrum are shown in Fig. S6. Derivatization with MSTFA causes a mass-shift of the analyte to *m/z* = M+72, due to the addition of the trimethylsilyl (TMS) group with mass 73, and the abstraction of one H atom. Typical losses of TMS adducts upon EI fragmentation include the TMS group $Si(CH_3)_3$ (*m/z* = 73), CH_3 (*m/z* = 15), and $Si(CH_3)_3O$ (TMS-O, *m/z* = 89). The remaining molecular ions have masses of *m/z* = M-1, *m/z* = M+57, and *m/z* = M-17, respectively (Borrás et al., 2021; Jaoui et al., 2004; Lai and Fiehn, 2018; Šepič and Leskovšek, 1999). The TMS ion is often the base ion with the strongest response.

The formation of oximes from ketones and aldehydes with PFBHA and the typical fragments in the EI spectrum are shown in Fig. S7. An intact mono-derivative after reaction with PFBHA will shift to *m/z* = M+195 (addition of PFBHA with mass 213, and loss of H_2O with mass 18). EI fragmentation produces a range of PFBHA-specific ions. Typically, a strong signal is observed for *m/z* = 181, resulting from cleavage of the C-O bond. The counterpart of this fragment has a mass of *m/z* = M+14 compared to the original compound. Other fragmentation mechanisms include O-N cleavage, N-C cleavage, and loss of NO, resulting in fragment ions of *m/z* = 197 and *m/z* = M-2, *m/z* = 211 and *m/z* = M -16, as well as *m/z* = 30 and *m/z* = M+165 respectively (Borrás et al., 2021; Šepič and Leskovšek, 1999). Compounds with multiple carbonyl functional groups can be derivatized multiple times. Given that the side chains of the central carbon atom differ from each other, PFBOs typically exist as geometric cis and trans isomers due to the C=N double bond of the oxime (Borrás et al., 2021; Jang and Kamens, 1999). The chromatogram therefore contains 2^x peaks, where x is the number of stereocentres as induced either by the derivatization process or the molecular structure itself.

Table S4: Number and selection of chromatographic peaks, and mass shifts of the compounds monitored by SPME-GC-MS. The mass shift was calculated as the difference of the evaluated SIM ions compared to the molecular weight. If no further explanation is given, the mass shift represents a typical fragment of the derivatization procedure (see Fig. S6 and S7).

Compound	Peaks (selected)	MW / g mol^{-1}	SIM / m/z	Mass shift	Note
PHE-d_6	1	100.15	156.1	M+56	As the TMS replaces a D atom and not a H atom, the mass shift after derivatization is only +71
OCR	1	108.14	165.1	M+57	
MCR	1	108.14	165.1	M+57	
PCR	1	108.14	165.1	M+57	
BOH	1	108.14	135.1	M+27	Loss of all three methyl groups from the TMS group
ONT	1	137.14	91.1	[no derivatization]	C_7H_7 fragment from loss of NO_2
NMB	1	137.14	91.1	[no derivatization]	C_7H_7 fragment from loss of NO_2
MNT	1	137.14	137.1	[no derivatization]	
BAC	1	122.12	179.1	M+57	
PMC	1	124.13	268.1	M+72+72	
GAL	2 (1+2)	60.05	312.1	M+195+57	Both derivatization steps; Peaks overlap, hence evaluated as sum
NCR	1	153.14	210.1	M+57	
PAC	1	88.06	340.1	M+195+57	Both derivatization steps
APH-d_8	2 (1)	128.20	323.1	M+195	
BAL	2 (1)	106.12	301.1	M+195	
GLY	2 (1)	58.04	448.1	M+195+195	
MGL	4 (3)	72.06	265.1	M+193	Both carbonyl groups derivatized, one undergoes O-N scission (-2)
PHB	2 (2)	122.12	389.1	M+195+72	Both derivatization steps

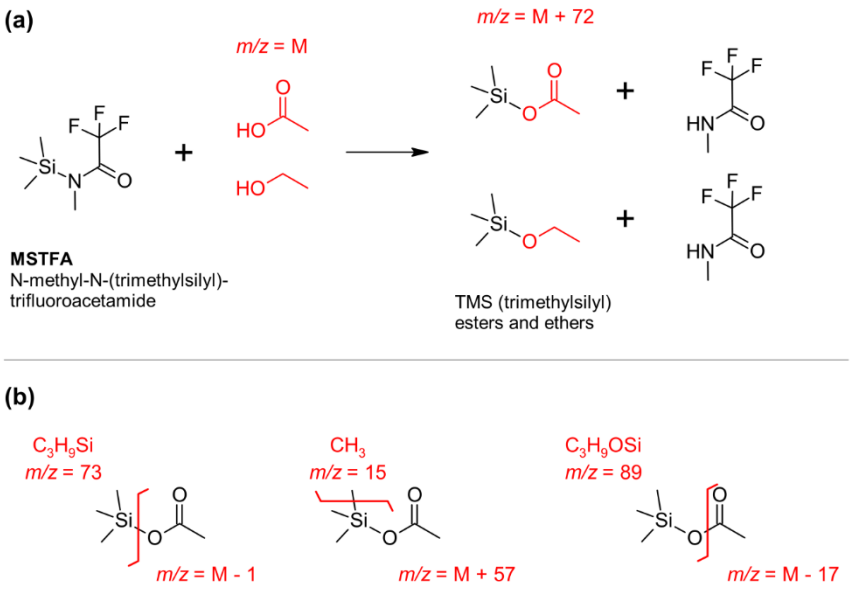

Figure S6: Derivatization mechanism of hydroxy and carboxylic groups and subsequent fragmentation patterns. ~~Upper graph:~~ **(a)** ~~d~~Derivatization of carboxylic acids (top) and alcohols (bottom) by reaction with MSTFA. ~~Lower graph:~~ **(b)** ~~t~~Typical fragments of TMS adducts after electron ionization.

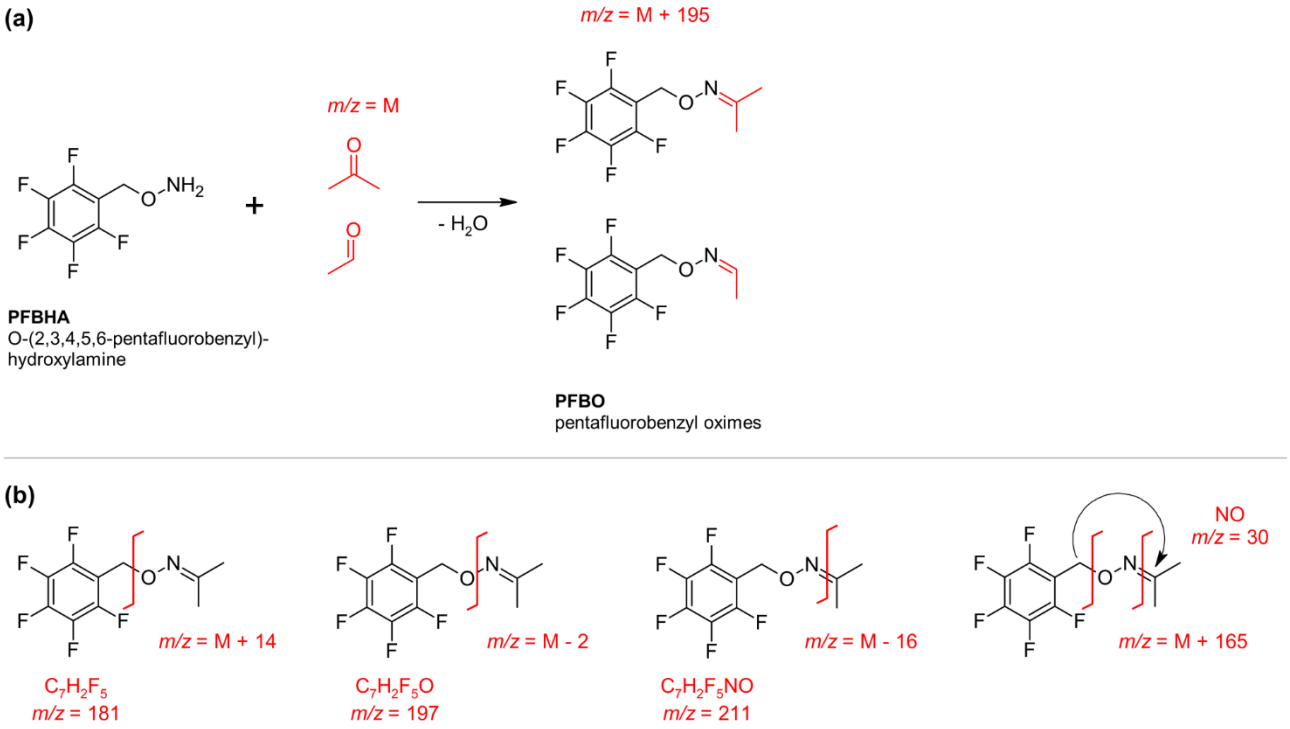

Figure S7: Derivatization mechanism of carbonyls and subsequent fragmentation patterns. ~~Upper graph:~~ **(a)** ~~d~~Derivatization of ketones (top) and aldehydes (bottom) by reaction with PFBHA. ~~Lower graph:~~ **(b)** ~~t~~Typical PFBO fragments after electron ionization.

S4 PTR-ToF-MS Analysis

Table S5: Measurement of toluene, its calibrated photooxidation products, and the internal standards with the PTR-ToF-MS. The primary ion was H_3O^+ in all cases. For all compounds, the sum formula, non-ionized mass, mass after proton transfer, and selected peak are listed. The internal standards were only monitored in a separate measurement to evaluate the stability of the permeation source.

Compound(s)	Sum formula	MW / g mol^{-1}	Protonated mass / m/z	Selected peak / m/z
Glyoxal	$C_2H_2O_2$	58.04	59.01	59.0041
Methylglyoxal	$C_3H_4O_2$	72.06	73.03	73.0243
Toluene, ^{13}C isotope	$^{13}CC_6H_8$	93.13	94.07	94.0716
Benzaldehyde	C_7H_6O	106.12	107.05	107.0470
Cresol isomers + Benzyl alcohol	C_7H_8O	108.14	109.06	109.0626
Phenol-d_6[(a)]	C_6D_6O	100.15	101.09	100.0795[(b)]
Acetophenone-d_8[(a)]	C_8D_8O	128.20	129.12	129.1172

[(a)] Internal standard: not monitored during experiments, not calibrated.
[(b)] The mass m/z -1 had a higher sensitivity than the protonated mass because of hydrogen-deuterium-exchange.

Table S6: Calibration factors, errors, and LODs for the compounds calibrated for the PTR-ToF-MS. The uncertainty of the slope is derived from the standard error of the slope with a 95% confidence interval. The instrumental error (Instr. Err.) is the mean RSD of all calibration levels. The quantification error (Quant. Err.) includes the instrumental error, the calibration error, and the experimental error. All errors are relative. For the ~~C_7H_8O~~ cresol isomers, we derived a weighted sensitivity by multiplying the recorded sensitivity with the relative abundance as determined by SPME-GC-MS (0.74 for *o*-cresol, 0.04 for *m*-cresol, and 0.22 for *p*-cresol). The weighted calibration factor for the sum signal was obtained from the sum of these weighted isomer-specific sensitivities. When evaluating individual ~~C_7H_8O~~ cresol isomers, we adopted the error and LOD of the weighted sum of the isomers.

Compound(s)	Slope / ncps ppbv^{-1}	Instr. Err. / %	Quant. Err. / %	LOD / pptv
Glyoxal	0.04±0.22	89	91	1827.8
Methylglyoxal	14.42±2.07	2	21	4.8
Benzaldehyde	30.82±2.01	1	21	0.5
Cresol isomers ~~+ Benzyl alcohol~~ (averaged)	27.61±1.57	1	21	1.1
Cresol isomers ~~+ Benzyl alcohol~~ (weighted)	31.78±1.27	1	21	0.9~~7~~
o-Cresol (~~raw~~ single / weighted)	37.37±1.29 / 27.65±0.95			
m-Cresol (~~raw~~single / weighted)	32.64±1.26 / 1.31±0.05			
p-Cresol (~~raw~~single / weighted)	12.82±1.23 / 2.82±0.27			
Benzyl alcohol ~~(raw / weighted)~~	0.00~~ / 0.00~~[(a)]			
Glyoxal fragment, *m/z* 31.0145[(b)]	2.45±1.44			
Benzyl alcohol fragment, *m/z* 91.0522[(b)]	29.24±2.20			

[(a)] No signal on m/z 109.0626 – regression resulted in slightly negative slope, therefore set to zero.
[(b)] Listed here only as information for the reader.

S5 Loss Corrections

S5.1 Correction Principle

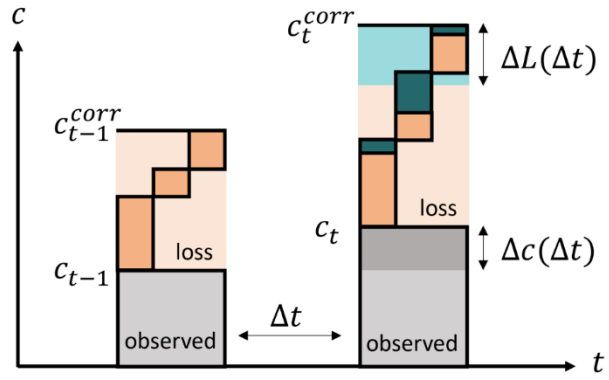

Figure S8: Implementation of the loss corrections. For a given data point, the loss-corrected concentration is calculated as the sum of the loss-corrected concentration of the previous data point, the measured change in concentration, and the absolute loss over that time period. This is equivalent to the measured concentration at that point in time plus the cumulative loss since the beginning of the experiment.

S5.2 Rate Constants for Reactions with OH Radicals

Table S7: Second order rate constants of the reactions of the measured photooxidation products with OH radicals at T = 298 K. Whenever available, IUPAC-recommended values were selected. Here, approximate pseudo first order rate constants (k′) are given as information for the reader to compare the order of magnitude against wall losses and photolysis rates. These rates were calculated with [OH] = 4.89×10^{6} molecules cm^{-3} (mean value in experiments at T = 298±1 K in absence of NO_x). For the actual implementation of the loss corrections, experiment- and time-specific OH radical concentrations were considered. OH radical concentrations were obtained by evaluating the loss of toluene. The uncertainty of the pseudo first order rate constants is 19 %.

Compound	k(OH) / molecules^{-1} cm^3 s^{-1}	Note	k' / s^{-1}
OCR	4.1×10^{-11} (IUPAC, 2024)[(a)]		$2.01\pm0.38\times10^{-4}$
MCR	5.9×10^{-11} (IUPAC, 2024)[(a)]		$2.89\pm0.55\times10^{-4}$
PCR	4.9×10^{-11} (IUPAC, 2024)[(a)]		$2.40\pm0.46\times10^{-4}$
BOH	2.7×10^{-11} (Harrison and Wells, 2009)[(a)]		$1.32\pm0.25\times10^{-4}$
ONT	1.22×10^{-12}	MNT value	$5.97\pm1.13\times10^{-6}$
NMB	1.22×10^{-12}	MNT value	$5.97\pm1.13\times10^{-6}$
MNT	1.22×10^{-12} (Atkinson et al., 1989)[(a)]		$5.97\pm1.13\times10^{-6}$
BAC	1.28×10^{-10} (Wu et al., 2017)		$6.27\pm1.19\times10^{-4}$
PMC	1.5×10^{-10} (Olariu et al., 2000)[(a)]		$7.34\pm1.39\times10^{-4}$
GAL	8×10^{-12} (IUPAC, 2024)[(a)]		$3.92\pm0.74\times10^{-5}$
NCR	5.15×10^{-12}	Mean of 2-nitro-*p*-cresol and 6-nitro-*m*-cresol, both (Bejan et al., 2007)[(a)]	$2.52\pm0.48\times10^{-5}$
PAC	1.2×10^{-13} (Mellouki and Mu, 2003)		$5.87\pm1.12\times10^{-7}$
BAL	1.26×10^{-11} (IUPAC, 2024)[(a)]		$6.17\pm1.17\times10^{-5}$
GLY	9.7×10^{-12} (IUPAC, 2024)[(a)]		$4.75\pm0.90\times10^{-5}$
MGL	1.3×10^{-11} (IUPAC, 2024)[(a)]		$6.36\pm1.21\times10^{-5}$
PHB	1.13×10^{-10} (US EPA, 2024)	Estimated using EPISUITE AopWinv1.92	$5.53\pm1.05\times10^{-4}$

[(a)] IUPAC recommendation.

S5.3 Wall Losses

Table S8: Empirical and fitted wall loss rates of the measured photooxidation products in the BATCH Teflon chamber. The uncertainty of the empirical wall loss rates was derived from the NRMSEs of the individual exponential regressions. The uncertainty of the fitted wall loss rates was calculated according to the 14 % error of the parameterization. The relative change (RC) from the empirical (EMP) to the fitted (FIT) rate was calculated as RC = (FIT − EMP)/EMP. The values for the compound groups are given as mean ± standard deviation of all compounds belonging to this group.

Compound	Group	Wall loss empirical			Wall loss fitted	
		Loss rate / s^{-1}	R^2	Uncertainty / %	Loss rate / s^{-1}	RC / %
OCR	(a)	$3.44\pm0.93\times10^{-5}$	0.57	27	$3.43\pm0.48\times10^{-5}$	±0
MCR	(a)	$3.39\pm0.81\times10^{-5}$	0.65	24	$4.03\pm0.56\times10^{-5}$	+19
PCR	(a)	$4.11\pm0.77\times10^{-5}$	0.76	19	$4.26\pm0.60\times10^{-5}$	+4
BOH	(a)	$4.45\pm0.92\times10^{-5}$	0.73	21	$4.43\pm0.62\times10^{-5}$	±0
ONT	(b)	$1.47\pm0.11\times10^{-5}$	0.96	8	-	-
NMB	(b)	$2.01\pm0.23\times10^{-5}$	0.91	11	-	-
MNT	(b)	$2.24\pm0.31\times10^{-5}$	0.88	14	-	-
BAC	(c)	$7.10\pm1.14\times10^{-5}$	0.82	16	$6.40\pm0.90\times10^{-5}$	-10
PMC	(c)	$8.49\pm1.20\times10^{-5}$	0.86	14	$6.05\pm0.85\times10^{-5}$	-29
GAL	(d)	$4.20\pm0.90\times10^{-5}$	0.70	21	$5.43\pm0.76\times10^{-5}$	+29
NCR	(e)	$6.58\pm1.04\times10^{-5}$	0.83	16	$6.44\pm0.90\times10^{-5}$	-2
PAC	(d)	$5.14\pm0.87\times10^{-5}$	0.78	17	$5.04\pm0.71\times10^{-5}$	-2
BAL	(f)	$4.54\pm1.80\times10^{-6}$	0.07	40	$1.49\pm0.21\times10^{-5}$	+229
GLY	(f)	$1.33\pm0.38\times10^{-5}$	0.45	28	$1.43\pm0.20\times10^{-5}$	+7
MGL	(f)	$1.96\pm0.63\times10^{-5}$	0.35	32	$7.82\pm1.09\times10^{-6}$	-60
PHB	(c)	$8.53\pm0.68\times10^{-5}$	0.95	8	$6.24\pm0.87\times10^{-5}$	-27
(a) Monohydric aromatic alcohols					$4.04\pm0.38\times10^{-5}$	
(b) Nitro compounds		$1.90\pm0.32\times10^{-5}$				
(c) Aromatic acids and multifunctional					$6.23\pm0.14\times10^{-5}$	
(d) Aliphatic multifunctional					$5.23\pm0.19\times10^{-5}$	
(e) Nitro compounds with OH group					6.44×10^{-5}	
(f) Carbonyls and dicarbonyls					$1.23\pm0.32\times10^{-5}$	

S6 SPME-GC-MS Method Evaluation

S6.1 Inter-Sample Variability

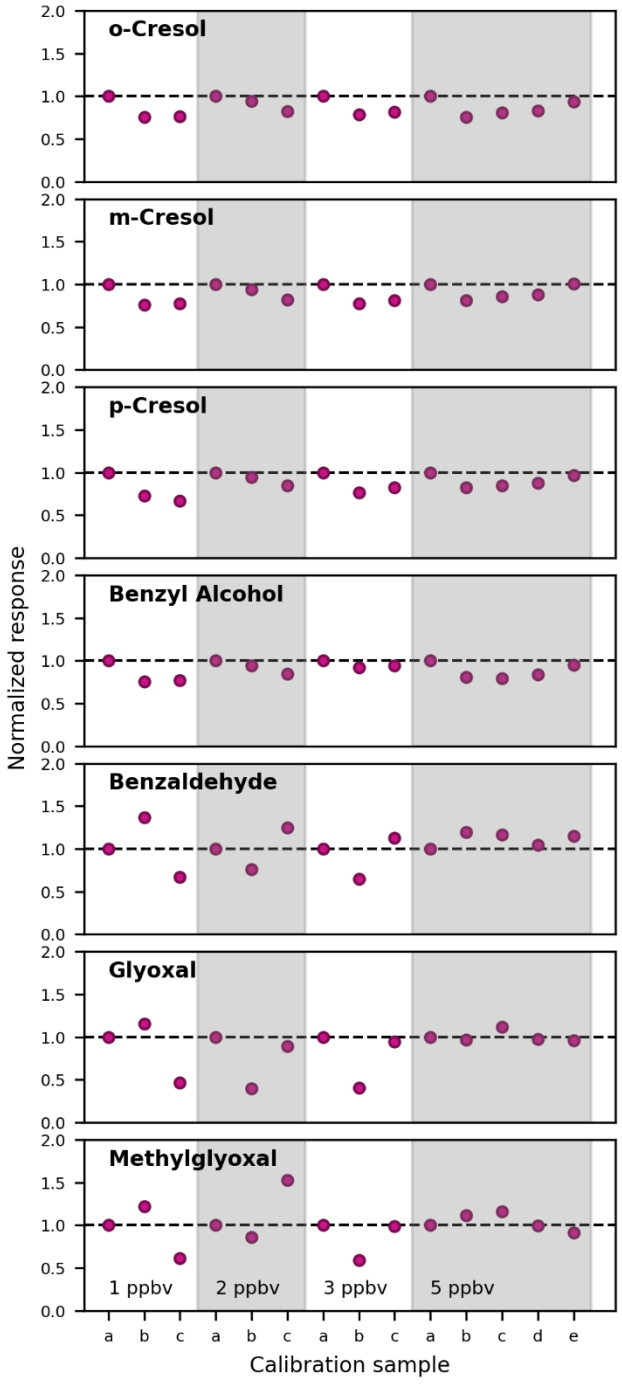

Figure S9: Inter-sample variability of the cresols, benzyl alcohol, benzaldehyde, glyoxal, and methylglyoxal at the SPME-GC-MS. The data are shown for the on-line calibration samples, and normalized within each calibration level. The calibration levels were calculated as concentrations, but are shown here as mixing ratios for simplicity. The depicted data include corrections for internal standard responses, blanks, and wall losses. Note that before each calibration level, the chamber was cleaned, and blanks were recorded (not shown here). The calibration levels at 0 ppbv and 0.5 ppbv are not shown here because of the substantial variability at low concentrations.

S6.2 Derivatization Reagents and Internal Standards

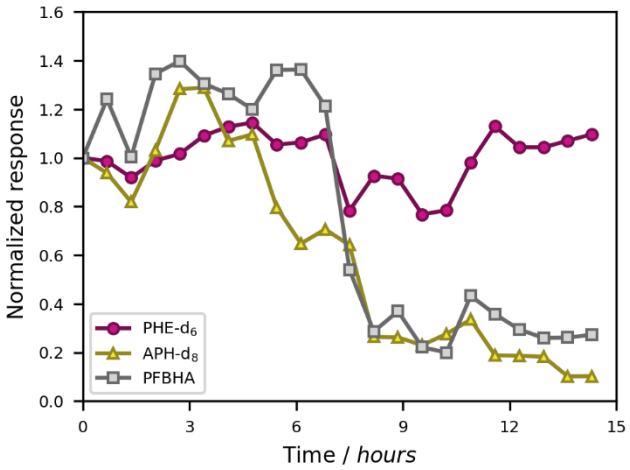

Figure S10: SPME-GC-MS data of the ISTD permeation source outflow mixed with zero air over a time frame of 15 hours. Time series of the two ISTDs (phenol-d_6 = PHE-d_6, and acetophenone-d_8 = APH-d_8) and PFBHA as the carbonyl reagent are shown. Responses were normalized to the respective start value for scalability. The silylants MSTFA and TMCS were not monitored to avoid stress on the MS detector.

S6.3 Method Limitations

For the purpose of characterizing the BATCH Teflon chamber, we focused on the compounds with the best sensitivity and suitability for the on-line analysis with our setup. The compounds which we excluded after initial testing are listed in Table S9. We observed the following limitations:

Firstly, we excluded small compounds with MW < 50 g mol^{-1} (acetaldehyde, formaldehyde, formic acid, and methanol) from our method due to low sensitivity. This is in agreement with the study by Gómez Alvarez and Valcárcel (2009), where the response of formaldehyde and acetaldehyde was lower than that of benzaldehyde. Generally, PDMS/DVB fibres are designed for molecular weights in the range of MW = 50 − 300 g mol^{-1} (manufacturer specification), explaining this observation.

Secondly, most tested carboxylic acids (acetic acid, formic acid, glutaric acid, glyoxylic acid, oxalic acid, succinic acid) could only be detected at elevated sampling temperature of 85 °C due to their low volatility. This was shown by offline measurements of heated vials containing a calibration standard. Meanwhile, benzoic acid and pyruvic acid could be calibrated for on-line analysis reasonably well, possibly due to their aromaticity and additional keto group, respectively. Similar to sticky compounds such as glyoxal (see main text), we acknowledge that the on-line analysis of low-volatility compounds in the chamber could be enhanced by a different material, length, and temperature of the transfer line, and a non-interrupted flow.

Thirdly, we observed low sensitivities and poor transportation from the chamber to the instrument for ketones. This is in line with the lower affinity of ketones to PFBHA compared to aldehydes (Jang and Kamens, 1999), and additionally suggests a substantial stickiness of these compounds. We excluded non-aromatic compounds with only keto functional groups (acetone, dimethylglyoxal). For the aromatic ketones, we could use acetophenone-d_8 as an internal standard but excluded *p*-toluquinone. The analysis of acetophenone-d_8 profited from the fact that it was added constantly and could therefore equilibrate well, and that we specifically designed the permeation source to release enough mass for a good instrumental response (nevertheless, the variability of acetophenone-d_8 was higher than for phenol-d_6, see main text). Furthermore, the direct addition of keto groups to the aromatic ring may induce steric hindrance and thereby inhibit an effective PFBHA derivatization. All tested aromatic compounds with carbonyl groups detached from the ring or with hydroxy/carboxylic groups were successfully optimized for on-line analysis.

Table S9: List of all tested compounds which were not included in the final SPME-GC-MS method due to methodological limitations. The retention time (RT), number of peaks and selected peak, and molecular weight (MW) are given for each compound. The functional groups amenable to oxime formation (PFBHA derivatization) or silylation (MSTFA/TMCS derivatization) are denoted as aldehydes (CHO), ketones (C=O), alcohols (OH), and carboxylic acids (COOH). The selected ion monitoring (SIM) masses were selected to represent abundant masses resulting from mass shifts and fragmentations which are typical for the respective derivatization process (see Sect. S3.4). For 4-nitro-*m*-cresol and *p*-nitrotoluene, the on-line calibration could be performed successfully, however the noise exceeded the signal during the photooxidation experiments, so that these compounds were not evaluated.

Compound	RT / min	Peaks (selected)	MW / g mol^{-1}	Oxime formation	Silylation	SIM / m/z	Mass shift	Methodological difficulty
Acetaldehyde	6.57	2 (1)	44.10	1 × CHO	-	209.1	M+165	Low sensitivity
Acetic acid	-	-	60.06	-	1 × COOH	-	-	No response
Acetone	6.77	1	58.08	1 × C=O	-	223.1	M+165	Low sensitivity
Dimethylglyoxal	9.76	1	86.09	2 × C=O	-	281.1	M+195	Not detected in on-line calibration
Formaldehyde	5.09	1	30.03	1 × CHO	-	195.0	M+165	Low sensitivity
Formic acid	-	-	46.03	-	1 × COOH	-	-	No response
Glutaric acid	10.60	1	132.12	-	2 × COOH	261.1	M+72+57	Requires high temperature
Glyoxylic acid	11.4	1	74.04	1 × CHO	1 × COOH	326.1	M+195+57	Requires high temperature
Methanol	-	-	32.04	-	1 × OH	-	-	No response
Oxalic acid	7.112	1	90.04	-	2 × COOH	147.1	[fragment][(a)]	Requires high temperature
Succinic acid	9.50	1	118.09	-	2 × COOH	147.1	[fragment][(a)]	Requires high temperature
p-Toluquinone	14.46	2 (1)	122.12	2 × C=O	-	317.1	M+195	Not detected in on-line calibration
4-Nitro-*m*-cresol	12.22	1	153.14	-	1 × OH	210.1	M+57	Noise higher than signal
p-Nitrotoluene	8.20	1	137.14	-	-	137.1	[no derivatization]	Noise higher than signal

[(a)] The ion m/z 147 is a typical fragment of silylated dicarboxylic acids (Pindado Jiménez et al., 2013).

S6.4 Calibration Curves without ISTD Correction

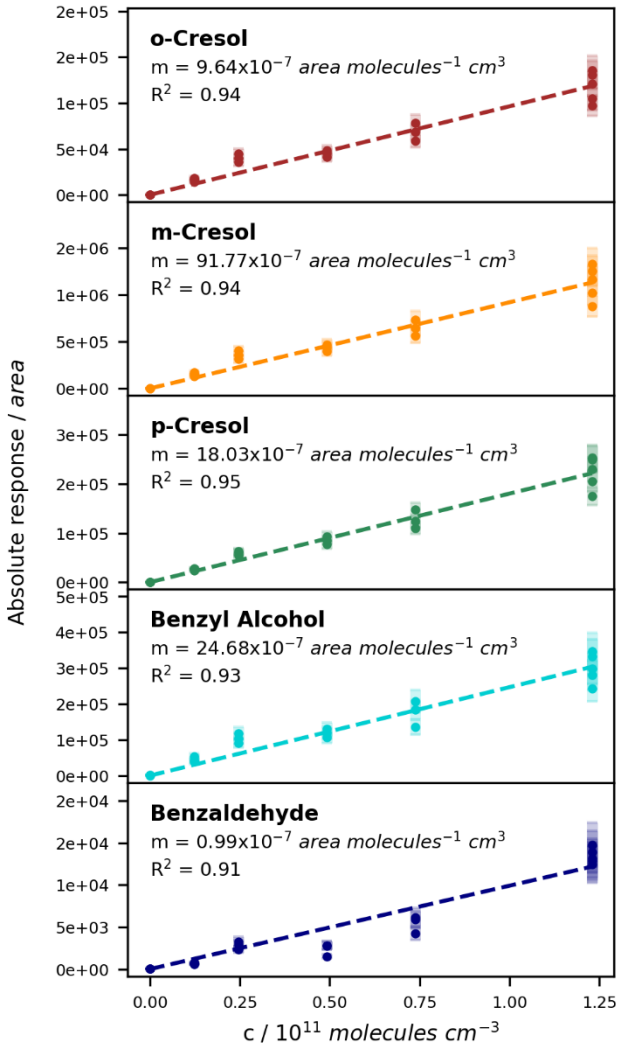

Figure S11: Calibration curves for the ring-retaining first generation products of toluene without the ISTD correction. The absolute responses are plotted against the concentration in the chamber. Uncertainty areas represent the instrumental error.

S7 Error and Validity of Loss Corrections

In order to obtain a weighted error for the loss-corrected data, we first calculated the absolute error of each loss process for each data point and compound. To do so, we considered the absolute loss, the error of the loss process, and the quantification error of the measured concentration. We then added the absolute errors of the non-corrected concentrations and the three losses to get a sum absolute error. This error was divided by the loss-corrected concentration to get a relative value.

The variability, minima and maxima, and mean values of these relative errors of the loss-corrected concentrations are listed for all compounds measured by SPME-GC-MS in Table S10. The data were collected from all 18 experiments, including temperature and NO_x variations. The mean relative errors of the loss-corrected concentrations were between 1 % (*o*-nitrotoluene) and 20 % (*p*-methylcatechol) higher than the errors of their non-corrected concentrations. Due to the added sources of uncertainty, we observed an increase of the relative error of the loss-corrected concentrations over the course of the experiment. Still, the variability of the relative error both across all the data and between the experimental means remained below 10 % for all compounds except *p*-methylcatechol which reacts fastest with OH radicals (Table S7). Benzoic acid has a similar rate constant for reaction with OH radicals but has a higher instrumental error that dominates the overall quantification error.

Table S10: Relative errors of the loss-corrected concentrations of the SPME-GC-MS data. The mean relative error and its increase compared to the quantification error of the non-corrected concentrations are given. The range of all individual relative errors across all 18 experiments as well as their variability are listed, along with the range and variability of the experimental mean values.

Compound	Loss-corrected error		All values		Experimental means	
	Mean value / %	Increase / %	Range / %	Variability / %	Range / %	Variability / %
OCR	26	10	24 – 29	4	25 – 28	4
MCR	27	12	24 – 29	4	25 – 29	4
PCR	27	11	25 – 29	4	26 – 29	3
BOH	25	8	23 – 27	3	24 – 27	3
ONT	22	1	21 – 23	1	22 – 23	1
NMB	22	3	18 – 34	8	20 – 26	6
MNT	22	2	14 – 23	5	20 – 22	3
BAC	40	7	38 – 47	3	38 – 41	2
PMC	30	20	26 – 103	32	27 – 46	14
GAL	25	5	24 – 29	3	25 – 26	2
NCR	26	5	23 – 30	4	24 – 28	3
PAC	30	18	27 – 40	9	28 – 35	6
BAL	51	9	48 – 56	3	50 – 52	1
GLY	60	6	57 – 64	2	58 – 61	1
MGL	52	10	48 – 58	3	49 – 53	2
PHB	35	8	32 – 38	4	34 – 37	3

The absolute and relative importance of wall losses, photolysis, and OH radical reactions is shown for each of the analysed compounds in Fig. S12.

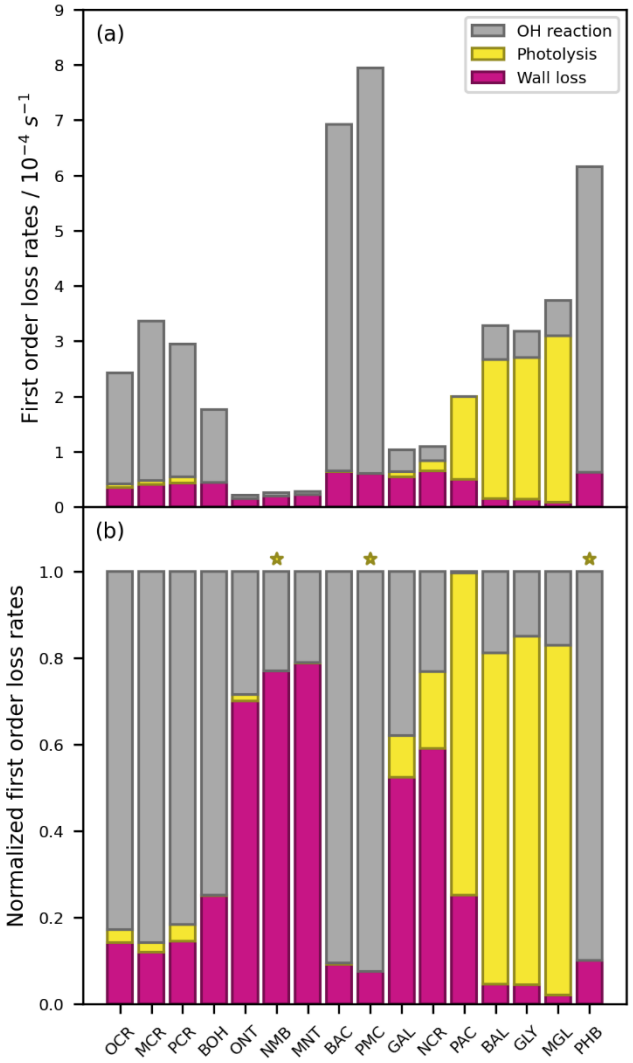

Figure S12: Loss processes for each of the analysed toluene photooxidation products. (a) First order loss rates. For the OH radical reactions, we used the mean OH radical concentration of [OH] = 4.89×10^6 molecules cm^{-3} for obtaining pseudo first order rates. **(b)** Normalization of the first order loss rates for each individual compound. Note that we could not compile any photolysis rates for (nitromethyl)benzene (NMB), *p*-methylcatechol (PMC), and *p*-hydroxybenzaldehyde (PHB), and assumed zero photolytic loss in these cases (marked with stars). Photolysis is only relevant during chamber irradiation, and the assumed OH radical concentration likewise only applies to the irradiated time period.

In order to evaluate and validate the loss correction procedure at the two instruments, we compared the measured and the loss-corrected data sets obtained by SPME-GC-MS and PTR-ToF-MS. ~~Since the extent of the loss corrections depends on the non-corrected concentrations, we selected experiments in which the measured data of the two instruments agreed particularly well.~~ We show this comparison for benzaldehyde as a compound with no known spectral interference and high photolytic losses (Fig. S132), and for *o*-cresol as one of the ~~C_7H_8O~~ cresol isomers and a compound with a high reactivity towards OH radicals and a relatively high wall loss rate (Fig. S143). ~~The loss-corrected data are in good agreement.~~ Figures S13 and S14 include not only the time series of the measured data and the individual losses for both instruments (Fig. S13b and S14b), but also the direct comparison of the relative change associated with the loss corrections (Fig. S13a and S14a). This relative change was calculated as the difference between the loss-corrected data and the measured data divided by the measured data, and makes it possible to

compare the extent of the loss corrections even in view of slightly different measured initial mixing ratios. The relative changes obtained by the two instruments are in good agreement for both compounds.

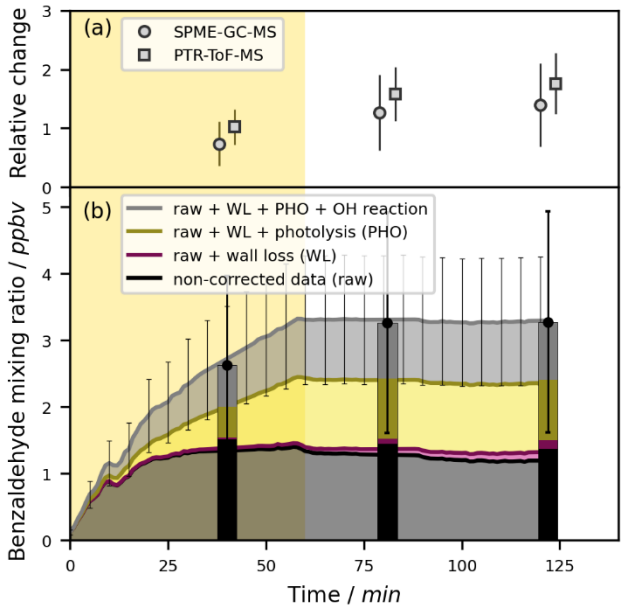

Figure S132: Measured and loss-corrected mixing ratio of benzaldehyde as obtained by the SPME-GC-MS and the PTR-ToF-MS. The data are shown for an experiment with 25 ppbv initial NO at T = 298±1 K. (a) The relative change between the measured and fully loss-corrected mixing ratio for each sample. (b) Absolute raw and corrected mixing ratios. Error bars in both panels are the instrumental quantification error.

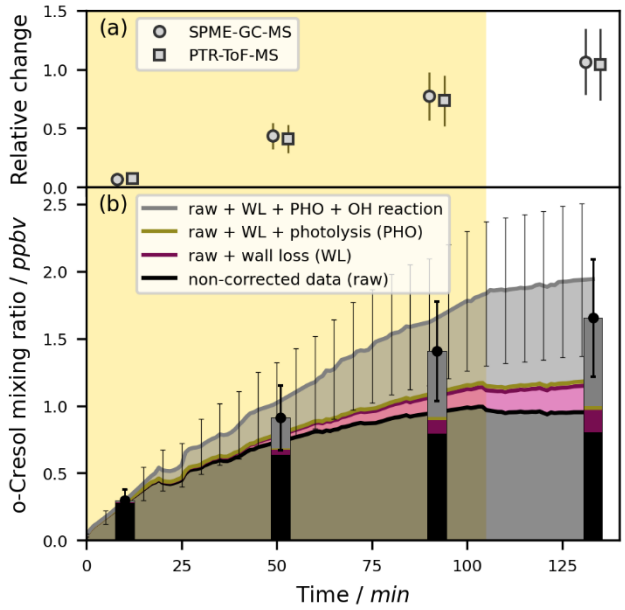

Figure S143: Measured and loss-corrected mixing ratio of *o*-cresol as obtained by the SPME-GC-MS and the PTR-ToF-MS. The data are shown for experiment Tol-OH-6. The mixing ratio of *o*-cresol at the PTR-ToF-MS was calculated from the weighted calibration and the fixed relative abundance of ~~the C_7H_8O isomers (~~0.741~~)~~ for *o*-cresol. (a) The relative change between the measured and fully loss-corrected mixing ratio for each sample. (b) Absolute raw and corrected mixing ratios. Error bars in both panels are the instrumental quantification error.

References

Atkinson, R., Aschmann, S. M., Arey, J., and Carter, W. P. L.: Formation of ring-retaining products from the OH radical-initiated reactions of benzene and toluene, Int. J. Chem. Kinet., 21, 801–827, https://doi.org/10.1002/kin.550210907, 1989.

Bacher, C., Tyndall, G. S., and Orlando, J. J.: The Atmospheric Chemistry of Glycolaldehyde, J. Atmospheric Chem., 39, 171–189, https://doi.org/10.1023/A:1010689706869, 2001.

Bejan, I., Aal, Y. A. E., Barnes, I., Benter, T., Bohn, B., Wiesen, P., and Kleffmann, J.: The photolysis of ortho-nitrophenols: a new gas phase source of HONO, Phys. Chem. Chem. Phys., 8, 2028–2035, https://doi.org/10.1039/B516590C, 2006.

Bejan, I., Barnes, I., Olariu, R., Zhou, S., Wiesen, P., and Benter, T.: Investigations on the gas-phase photolysis and OH radical kinetics of methyl-2-nitrophenols, Phys. Chem. Chem. Phys., 9, 5686–5692, https://doi.org/10.1039/B709464G, 2007.

Borrás, E., Tortajada-Genaro, L. A., Ródenas, M., Vera, T., Speak, T., Seakins, P., Shaw, M. D., Lewis, A. C., and Muñoz, A.: On-line solid phase microextraction derivatization for the sensitive determination of multi-oxygenated volatile compounds in air, Atmospheric Meas. Tech., 14, 4989–4999, https://doi.org/10.5194/amt-14-4989-2021, 2021.

Chen, J., Wenger, J. C., and Venables, D. S.: Near-Ultraviolet Absorption Cross Sections of Nitrophenols and Their Potential Influence on Tropospheric Oxidation Capacity, J. Phys. Chem. A, 115, 12235–12242, https://doi.org/10.1021/jp206929r, 2011.

El Dib, G., Chakir, A., Roth, E., Brion, J., and Daumont, D.: Study of Benzylperoxy Radical Using Laser Photolysis: Ultraviolet Spectrum, Self-Reaction, and Reaction with HO_2 Kinetics, J. Phys. Chem. A, 110, 7848–7857, https://doi.org/10.1021/jp056860p, 2006.

Etzkorn, T., Klotz, B., Sørensen, S., Patroescu, I. V., Barnes, I., Becker, K. H., and Platt, U.: Gas-phase absorption cross sections of 24 monocyclic aromatic hydrocarbons in the UV and IR spectral ranges, Atmos. Environ., 33, 525–540, https://doi.org/10.1016/S1352-2310(98)00289-1, 1999.

Gómez Alvarez, E. and Valcárcel, M.: Research into conditions of quantitivity in the determination of carboniles in complex air matrices by adsorptive solid phase microextraction, Talanta, 77, 1444–1453, https://doi.org/10.1016/j.talanta.2008.09.044, 2009.

Harrison, J. C. and Wells, J. R.: Gas-phase chemistry of benzyl alcohol: Reaction rate constants and products with OH radical and ozone, Atmos. Environ., 43, 798–804, https://doi.org/10.1016/j.atmosenv.2008.11.001, 2009.

Horowitz, A., Meller, R., and Moortgat, G. K.: The UV–VIS absorption cross sections of the α-dicarbonyl compounds: pyruvic acid, biacetyl and glyoxal, J. Photochem. Photobiol. Chem., 146, 19–27, https://doi.org/10.1016/S1010-6030(01)00601-3, 2001.

IUPAC: Evaluated Kinetic Data, International Union of Pure and Applied Chemistry (IUPAC) Task Group on Atmospheric Chemical Kinetic Data Evaluation, https://iupac.aeris-data.fr/ (last access 05 February 2024), 2024.

Jang, M. and Kamens, R. M.: Newly characterized products and composition of secondary aerosols from the reaction of α-pinene with ozone, Atmos. Environ., 33, 459–474, https://doi.org/10.1016/S1352-2310(98)00222-2, 1999.

Jaoui, M., Kleindienst, T. E., Lewandowski, M., and Edney, E. O.: Identification and Quantification of Aerosol Polar Oxygenated Compounds Bearing Carboxylic or Hydroxyl Groups. 1. Method Development, Anal. Chem., 76, 4765–4778, https://doi.org/10.1021/ac049919h, 2004.

Johnston, H. S., Davis, H. F., and Lee, Y. T.: NO_3 Photolysis Product Channels: Quantum Yields from Observed Energy Thresholds, J. Phys. Chem., 100, 4713–4723, https://doi.org/10.1021/jp952692x, 1996.

Kahan, T. F., Washenfelder, R. A., Vaida, V., and Brown, S. S.: Cavity-Enhanced Measurements of Hydrogen Peroxide Absorption Cross Sections from 353 to 410 nm, J. Phys. Chem. A, 116, 5941–5947, https://doi.org/10.1021/jp2104616, 2012.

Lai, Z. and Fiehn, O.: Mass spectral fragmentation of trimethylsilylated small molecules, Mass Spectrom. Rev., 37, 245–257, https://doi.org/10.1002/mas.21518, 2018.

Meller, R., Raber, W., Crowley, J. N., Jenkin, M. E., and Moortgat, G. K.: The UV-visible absorption spectrum of methylglyoxal, J. Photochem. Photobiol. Chem., 62, 163–171, https://doi.org/10.1016/1010-6030(91)87017-P, 1991.

Mellouki, A. and Mu, Y.: On the atmospheric degradation of pyruvic acid in the gas phase, J. Photochem. Photobiol. Chem., 157, 295–300, https://doi.org/10.1016/S1010-6030(03)00070-4, 2003.

Mitchell, G. D.: A Review of Permeation Tubes and Permeators, Sep. Purif. Methods, 29, 119–128, https://doi.org/10.1081/SPM-100100005, 2000.

Namies´nik, J.: Generation of standard gaseous mixtures, J. Chromatogr. A, 300, 79–108, https://doi.org/10.1016/S0021-9673(01)87581-6, 1984.

Olariu, R. I., Barnes, I., Becker, K. H., and Klotz, B.: Rate coefficients for the gas-phase reaction of OH radicals with selected dihydroxybenzenes and benzoquinones, Int. J. Chem. Kinet., 32, 696–702, https://doi.org/10.1002/1097-4601(2000)32:11<696::AID-KIN5>3.0.CO;2-N, 2000.

Pindado Jiménez, O., Pérez Pastor, R. M., Vivanco, M. G., and Santiago Aladro, M.: A chromatographic method to analyze products from photo-oxidation of anthropogenic and biogenic mixtures of volatile organic compounds in smog chambers, Talanta, 106, 20–28, https://doi.org/10.1016/j.talanta.2012.11.081, 2013.

Reed Harris, A. E., Doussin, J.-F., Carpenter, B. K., and Vaida, V.: Gas-Phase Photolysis of Pyruvic Acid: The Effect of Pressure on Reaction Rates and Products, J. Phys. Chem. A, 120, 10123–10133, https://doi.org/10.1021/acs.jpca.6b09058, 2016.

Roth, E., Chakir, A., and Ferhati, A.: Study of a Benzoylperoxy Radical in the Gas Phase: Ultraviolet Spectrum and $C_6H_5C(O)O_2$ + HO_2 Reaction between 295 and 357 K, J. Phys. Chem. A, 114, 10367–10379, https://doi.org/10.1021/jp1021467, 2010.

Sandus, O. and Slagg, N.: Reactions of Aromatic Nitrocompounds. 1. Photochemistry, Feltman Research Laboratory, Picatinny Arsenal, Dover, NJ, 1972.

Šepič, E. and Leskovšek, H.: Isolation and identification of fluoranthene biodegradation products, Analyst, 124, 1765–1769, https://doi.org/10.1039/A904990H, 1999.

Serralheiro, C., Duflot, D., da Silva, F., Hoffmann, S., Jones, N., Nj, M., B, M., and P, L.-V.: Toluene Valence and Rydberg Excitations as Studied by ab initio Calculations and Vacuum Ultraviolet (VUV) Synchrotron Radiation, J. Phys. Chem. A, 119, https://doi.org/10.1021/acs.jpca.5b05080, 2015.

Shama, S. A. A. E.-A.: Vacuum ultraviolet absorption spectra of organic compounds in gaseous and liquid state, Doctoral thesis, University of Zagazig, Zagazig, 1991.

Thorenz, U. R., Kundel, M., Müller, L., and Hoffmann, T.: Generation of standard gas mixtures of halogenated, aliphatic, and aromatic compounds and prediction of the individual output rates based on molecular formula and boiling point, Anal. Bioanal. Chem., 404, 2177–2183, https://doi.org/10.1007/s00216-012-6202-5, 2012.

Troe, J.: Are Primary Quantum Yields of NO_2 Photolysis at $\lambda \leq 398$ nm Smaller than Unity?, Z. Für Phys. Chem., 214, 573, https://doi.org/10.1524/zpch.2000.214.5.573, 2000.

US EPA: Estimation Programs Interface Suite (EPI Suite), model AopWin v1.92, United States Environmental Protection Agency, 2024.

Volkamer, R., Spietz, P., Burrows, J., and Platt, U.: High-resolution absorption cross-section of glyoxal in the UV–vis and IR spectral ranges, J. Photochem. Photobiol. Chem., 172, 35–46, https://doi.org/10.1016/j.jphotochem.2004.11.011, 2005.

Wu, C., De Visscher, A., and Gates, I. D.: Reactions of hydroxyl radicals with benzoic acid and benzoate, RSC Adv., 7, 35776–35785, https://doi.org/10.1039/C7RA05488B, 2017.

Zhu, L. and Cronin, T. J.: Photodissociation of benzaldehyde in the 280–308 nm region, Chem. Phys. Lett., 317, 227–231, https://doi.org/10.1016/S0009-2614(99)01375-5, 2000.